E.A.M. Klein Holkenborg

Towards Water Availability Predictions with Earth-Observed Open Data in Man-Made Reservoirs Worldwide

TUDelft   **Deltares**   510

Towards Water Availability Predictions with Earth-Observed Open Data in Man-Made Reservoirs Worldwide

By

E.A.M. Klein Holkenborg

in partial fulfilment of the requirements for the degree of

Master of Science
in Civil Engineering

at the Delft University of Technology,
to be defended publicly on Monday May 15, 2023 at 15:45.

Thesis committee:	Dr. ir. H.C. Winsemius	Deltares
	Prof. dr. ir. R. Uijlenhoet	TU Delft
	Prof. dr. ir. T.C. Comes	TU Delft
	Dr. M.J.C. van den Homberg	510

An electronic version of this thesis is available at http://repository.tudelft.nl/.

Preface

It is with great pleasure that I present this master's thesis, the culmination of months of dedicated and rigorous work. The objective of this study was to investigate the role of volume time series, generated from a novel method of reservoir bathymetry reconstruction using open earth observation data, in predicting water availability in man-made reservoirs worldwide. By establishing volume estimations in these reservoirs and exploring the first steps into predictive tools that could assist decision-makers in mitigating drought-induced hazards, I am proud to contribute to Global Water Watch's vision of democratizing earth's data on water resources.

The modelling work, which was conducted using Python, involved construction of a bathymetry model, validation of the results with extensive datasets, and evaluation of the predictive skill of each model in case studies in Eswatini and Lesotho. Finally, I enjoyed the work and I look forward to seeing the method integrated into Global Water Watch and continuing to evolve.

Acknowledgements

This thesis is established with the support and guidance of many, whom I would like to express my gratitude to:

First and foremost, I would like to express my sincere appreciation to my first supervisor, Hessel Winsemius, for his insightful ideas and guidance throughout the thesis process. His weekly meetings were helping me to gain a deeper understanding of the subject matter and encouraging me to think critically and creatively.

I would also like to thank everyone at Deltares, especially the team members of Global Water Watch, with whom I had the privilege of working. Starting as an intern and completing my master's studies within the team was a remarkable experience, and I learned a great deal from the colleagues, fellow interns, and the HYD department.

My special thanks go to Marc van den Homberg, who provided guidance within 510 and had been involved since my internship. He was a fount of excellent ideas, connected me to new persons, and helped to contextualise my thesis.

I am also grateful to Remko Uijlenhoet and Tina Comes for being part of the thesis committee and offering unique perspectives and insights.

Furthermore, I would like to thank my parents, Martin and Moniek, and brothers, Bern and Marn, for their unwavering support throughout my studies, including reviewing my work and assisting me with moving into a new home during the busiest period of my Master's and staying up late to discuss even the smallest details. Last but not least, I am grateful to Mark for always being a source of support and for always seeing the bright side!

I would also like to extend my thanks to everyone who provided guidance, organised lectures, and supported meetings throughout my Master's program in Water Management, of which this thesis is the final component. I would like to specifically acknowledge the Dispuut Water and Environment, where I made valuable friendships who enriched my experience of being a Masters' student.

In conclusion, I would like to express my sincere appreciation to all the individuals who have supported me during this journey. It is my hope that this thesis will contribute to the scientific community and provide insights into the value of volume time series in water availability predictions in man-made reservoirs worldwide.

E.A.M. Klein Holkenborg
Delft, May 2023

Abstract

Small to medium-sized man-made freshwater reservoir are a reliable source for drinking water supply, hydropower generation and irrigation purposes worldwide. However, water volumes in these reservoirs can be significantly affected by prolonged droughts, resulting in severe impacts on society (Kozacek, 2014; Mahr, 2018). To mitigate the impact of such events it is crucial for decision makers to know when the available water resources are lacking. Although many reservoirs are closely monitored, this data is not always readily available. Inadequate information sharing, inaccessibility, and a lack of tools to predict future reservoir storages contribute to this problem.

Remote sensing has the potential to address this problem. The Global Water Watch is a platform that and provides earth-observed surface area dynamics that can be used to monitor small to medium-sized reservoirs worldwide and detect trends in water availability. While this method serves as a valuable indicator of water availability, it falls short in providing decision-makers with the necessary absolute volume time series and volume predictions. Currently, no platform exists beyond in-situ measurements to meet this essential need.

This thesis presents a novel method for retrieving near real-time volume time series in small to medium-sized man-made reservoirs worldwide using remotely sensed open data. The method utilises the MERIT-Hydro digital elevation model, HydroMT and stream flow methods by Eilander et al. (2023), and literature by Messager et al. (2016) to reconstruct reservoir bathymetry. This novel approach in reconstructing reservoir bathymetry enables the conversion of available reservoir area time series into volume time series. These were employed in autoregressive and multi-linear regression models to predict water availability up to six months in advance. The models incorporate ERA5 precipitation data by Hersbach's (2020) and the Standardised Precipitation and Evaporation Index (SPEI) by Beguería et al. (2021) to improve the accuracy of the volume predictions.

When comparing the novel method to the method proposed by Messager et al. (2016), the novel method yielded more accurate reservoir volume estimations. The method successfully obtained bathymetries and accurate volume estimations when validating using 2 reservoirs in Zambia and 48 in India, demonstrating the potential of this novel approach. However, some reservoirs with complex shapes faced initial delineation challenges, resulting in inaccurate volume predictions. These issues could be resolved by manually delineating the area for bathymetry reconstruction. Moreover, regression models were applied to case study reservoirs in Eswatini and Lesotho, demonstrating reasonable predictive capabilities with the Heidke Skill Scores ranging from 0.77 to 1 for up to 2 months ahead. However, precise prediction of extreme decreases in reservoir levels requires a physically based approach that incorporates the volumetric time series provided by this novel method. The study emphasises the necessity of considering the volume time series' memory to predict water availability and provides a valuable foundation for volume time series analysis using remotely sensed data.

Contents

List of Figures and Tables

Nomenclature

List of Symbols

A	Surface area of the reservoir (m^2)
k	Flattening Parameter
β	Weights associated with volume
C	Datum (reference water level) (m)
D_t	Topographic depth (m)
ε_m	White noise in the respectable month (m^3)
$d_x d_y$	Pixel surface area (m^2)
d	Distance from nearest cell upstream of the reservoir (m)
h	Water level (m)
h_0	Water level at bottom of reservoir (m)
m	Month
N	Number of pixels (-)
P	Precipitation (mm)
P_{MLR}	Multi-linear regression model based on precipitation inputs
∂	Weights associated with SPEI
s	Slope (rad) sampled in the nearest onshore upstream cell
$SPEI$	Standardised Precipitation and Evapotranspiration Index (-)
$SPEI_{MLR}$	Multi-linear regression model based on SPEI inputs
V	Reservoir volume (m^3)
V_{auto}	Autoregressive model
$V - P_{MLR}$	Multi-linear regression model based on volume and precipitation inputs
$V - SPEI_{MLR}$	Multi-linear regression model based on volume and SPEI inputs
ω	Weights associated with precipitation

List of Abbreviations

ATLAS	Advanced Topographic Laser Altimeter System
DEM	Digital Elevation Maps
GLAS	Geoscience Laser Altimeter System
GOODD	GlObal geOreferenced Database of Dams
GRanD	Global Reservoir and Dam database
HSS	Heidke Skill Score
ICESAT-2	Ice, Cloud and land Elevation Satellite
InSAR	Interferometric Synthetic Aperture Radar
LiDAR	Light Detection and Ranging
MERIT-Hydro	Multi-Error-Removed Improved-Terrain Hydro
SAR	Synthetic Aperture Radar
SRTM	Shuttle Radar Topography Mission

1
Introduction

Roughly four billion people worldwide, of which 75% lives in agricultural areas, suffer from limited to no access to clean water for drinking and hygiene for at least one month per year (UNICEF, 2023; UNESCO, 2019). Worldwide this results in 55 million people that require immediate assistance, need displacement or evacuation. Moreover, at least 1100 deaths annually can be directly related to severe dehydration. These impacts are often driven by the occurrence of water scarcity, which is the long-term unsustainable use of water resources (Van Loon & Van Lanen, 2013).

Water scarcity is highly influenced by water management practices and affects the water availability (Van Loon & Van Lanen, 2013). Examples are seen where humanitarian impacts are mitigated due to effective management of available water resources during meteorological or agricultural droughts (Murray-Darling Basin Authority, 2022; Hallema, 2022; Mahr, 2018). On the other hand, the neglecting of water resource management can put society at even higher risks (Kozacek C., 2014). Also, the lack of water availability can be driven by mismanagement alone, independent of occurrence of drought (Greenwood, 2018).

Effective management of water resources is essential to build resilience against natural disasters (UNDRR, 2015). To achieve this, there is a need for understanding disaster risk in all its dimensions, as expressed in the United Nations Sendai Framework for Disaster Risk Reduction. For lacking water availability, this includes the monitoring of our available clean water resources and predicting when water will be scarce. This information enhances risk governance in water management, opens opportunities for effective investment of capacities and allows for effective response, or actions in anticipation of events.

These anticipatory actions are preferred over responsive action, as anticipatory actions mitigate the impact before it materialises (FAO, 2022). Anticipatory actions are implemented after predictions of hazards. The implementation time of the action could require the prediction to be further into the future, introducing significant uncertainties (FAO, 2022). Therefore, the risk of acting in-vain increases, which ultimately means risking the loss of allocated resources or the unnecessary installation of measures. This is a problem especially when measures, like curtailments, have negative impact on livelihoods (Mahr, 2018).

The monitoring of reservoirs could contribute to the understanding of water availability dynamics and risks, and thereby helps to reduce the risk of in-vain actions. Generally monitoring is done in-situ or with satellite applications. In-situ measurements often provide more accurate data; however, it is highly labour intensive, could entail high costs, and acquires access to the reservoir of interest. The latter could be difficult due to logistic or safety reasons, or in transboundary conflicts, due to political reasons. Satellite applications mitigate these issues. They can provide relatively low-cost analysis (when open-source data is used, and the amount of computational time is taken care of) and they allow for analysis on global scale.

Recent efforts dealt with the known difficulties that come with using satellite imagery for reservoir analysis, and enabled monitoring of global reservoirs (Donchyts et al., 2022). Time series analysis of surface water area in lakes and man-made reservoirs could provide indication of water availability in the region (Donchyts et al., 2022). For the sake of understanding water availability dynamics, there is an interest to obtain volumes out of the provided surface areas for any specific reservoir. The insight in reservoir volumes, and their predictions, is expected to benefit decisions about the implementation of anticipatory actions, and thereby benefit societies' resilience to lacking water availability.

1.1 Research questions

This MSc thesis establishes an approach, referred to as the 'novel method', for estimating near real-time volumes in man-made reservoirs, without the need for in-situ access. This method involves reconstructing the reservoir bathymetry and the associated hypsometric curve, which characterises the relationships between the reservoir's volume, surface area, and water level height. The results for 2 reservoirs in Zambia and 48 reservoirs in India will be compared to in-situ measurements of water level and storage data and to a more generic method proposed in literature by Messager et al. (2016). Moreover, an assessment of the forecasting skill of regression models will be made by predicting volume dynamics in the Hawane reservoir in Eswatini during a severe drought in 2016, and the Katse Dam reservoir in Lesotho in 2015. The set of regression models will be employed to generate the forecasts of future volumes for lead times of up to six months. In conclusion, the research outcomes will showcase the potential of the novel method in remotely estimating near real-time volume time series in reservoirs by utilising Global Water Watch (Donchyts, et al., 2022). Additionally, the study will evaluate whether the data generated by this approach can be employed to develop predictions that facilitate decision-making aimed at mitigating the impacts of reduced water availability.

This objective will be reached by answering the following main question:

What is the performance and usability of a novel method for reservoir bathymetry reconstruction utilised for water availability predictions with earth-observed open data in man-made reservoirs worldwide?

To answer the main question, three sub questions are defined:

1. **What is the accuracy of the hypsometric curve established with the novel method?**

2. **How does the accuracy of the hypsometric curve proposed in this study compare with the benchmark method developed by Messager et al. (2016)?**

3. **What is the skill of regression models utilising volume time series generated by the novel method combined with SPEI or precipitation time series in predicting water availability in the Hawane reservoir located in Eswatini?**

1.2 Hypothesis

It is hypothesised that the novel method has the capability to extract the volume time series of any small to medium man-made reservoirs in the Global Water Watch dataset, provided that a dam wall is identifiable in the digital elevation model (DEM) chosen for the method. The hypothesis postulates that the DEM can also facilitate the extraction of other physical parameters such as the dam wall height, elevation of dam outlet, flow direction, dimensions of the reservoir surface area, and the surrounding terrain slope. Consequently, a more sophisticated bathymetry reconstruction can be carried out on man-made reservoirs using this method, benefitting its accuracy over conventional approaches reported in the literature that are applicable to both man-made reservoirs and natural lakes (Hollister & Milstead, 2010; Sobek, Nisell, & Fölster, 2011; Heathcote, Giorgio, & Prairie, 2015; Messager, Lehner, Grill, Nedeva, & Schmitt, 2016).

Given that the novel method utilises surface area measurements from the Global Water Watch dataset to estimate volumes, and surface area time series have been available since 1984, there exists a sufficiently long time series to construct data-driven models that can predict future volumes. Regarding the volume predictions, it is hypothesised that it is crucial to incorporate the memory of the volume time series itself, as the current volume state of the reservoir, due to the residence time of water, influences the future water volume in the reservoir. Moreover, the model's forecasting skill is expected to improve with the inclusion of precipitation time series, which via runoff is the reservoir's primary inflow, and the standardised precipitation and evapotranspiration index (SPEI) time series, a regional drought index that provides an indication of the level of evapotranspiration in the region and indirectly provides insight into water demand.

1.3   Thesis structure

The thesis structure began with an introduction in Chapter 1, which outlined the research objectives and hypothesis. In the remaining of this thesis, Chapter 2 provides background information on the subject and discusses related works. The methods applied in this study are presented in detail in Chapter 3. The results and findings of the study are presented in Chapter 4, followed by a discussion of the results in Chapter 5, where the usability of the novel method will be discussed. Finally, the conclusions drawn from the study are presented in Chapter 6, where also recommendations for future research is presented. This structured approach ensures a cohesive argument and a thorough analysis of the performance and usability of the novel method for reservoir bathymetry reconstruction utilised for water availability predictions.

2

Background & Related Work

The background and related work section of this thesis provides a comprehensive review of the key concepts around water availability estimations and predictions in man-made reservoirs. Section 2.1 differentiates man-made reservoirs from natural lakes, the two groups that constitute Earth's freshwater bodies. Section 2.2 focuses specifically on these man-made reservoirs and explains how their storage is established. Section 2.3 introduces how the storage in man-made reservoirs can be described and introduces the hypsometric curve, a metric that relates volume, area, and water level. Furthermore, it is explained how the curve can be derived with the use of digital elevation models (DEMs). Section 2.4 provides background information on the creation of DEMs, which were created by spaceborne technologies. In Section 2.5, the analysis of surface water dynamics is discussed, with a focus on the Global Water Watch database, which provides essential information for the method in this thesis. Section 2.6 explores literature that estimates reservoir storage using the previously discussed remotely sensed data and highlights the method by Messenger et al. (2016), which is considered the benchmark method in this thesis. In addition, Section 2.7 touches upon the impact of sedimentation on volume estimations. Section 2.8 provides an overview of model approaches for modelling volume dynamics in reservoirs. Section 2.9 delves into data-driven approaches, specifically autoregression and multi-linear regression. Finally, Section 2.10 explains how the predictive skill of a model is assessed with the Heidke Skill Score.

2.1 The Distinction Between Natural Lakes and Man-Made Reservoirs

According to Downing (2016) over 3% of Earth's continental terrain (~4.6 million km^2) is covered by water. This water coverage includes over 500.000 water bodies that have surface areas exceeding 1 hectare (~2.59 million km^2), with the smaller subset of 70.000 water bodies larger than 10 hectares covering the majority of the surface area (~2.47 million km^2). While some bodies of water are primarily a part of natural systems, others play critical roles in various societal structures, such as providing water and electricity. These water bodies can be categorised into two major groups: natural lakes, which form due to geological processes and act as a sinkhole of the surrounding landscape, and man-made reservoirs, which are formed by building a dam across a river to impound water.

Morris and Fan (1998) reported that while natural lakes and man-made reservoirs may share some similar characteristics, they also have fundamental differences. In terms of similarities, they can have comparable depths, nutrient concentrations, temperatures, and sediment loads, particularly if they are situated in the same climatic zone and have similar hydraulic residence times or nutrient and sediment loading. However, natural lakes tend to have a larger hydrologic size, higher age, and greater transparencies, while man-made reservoirs exhibit higher water level variations and a higher shoreline to area ratio. Figure 2.1 represents distinct geometries of a natural lake and a man-made reservoir. Moreover, the shape of a man-made reservoir is often more linear and dendritic, whereas natural lakes tend to have a more oval shape, as illustrated in Figure 2.1. Furthermore, the depth of man-made reservoirs tends to increase towards the dam, while the maximum depth of natural lakes is usually found in the central region. These differences are crucial for accurately reconstructing the bathymetry of water bodies and estimating its contained volume.

In addition, it is worth noting that a third, much smaller, group of water bodies exists. These are lakes that have been expanded by constructing a dam wall across their natural outflow, thereby increasing their storage capacity. These extended natural lakes can exhibit characteristics of both natural lakes and reservoirs, which were described by Morris and Fan (1998).
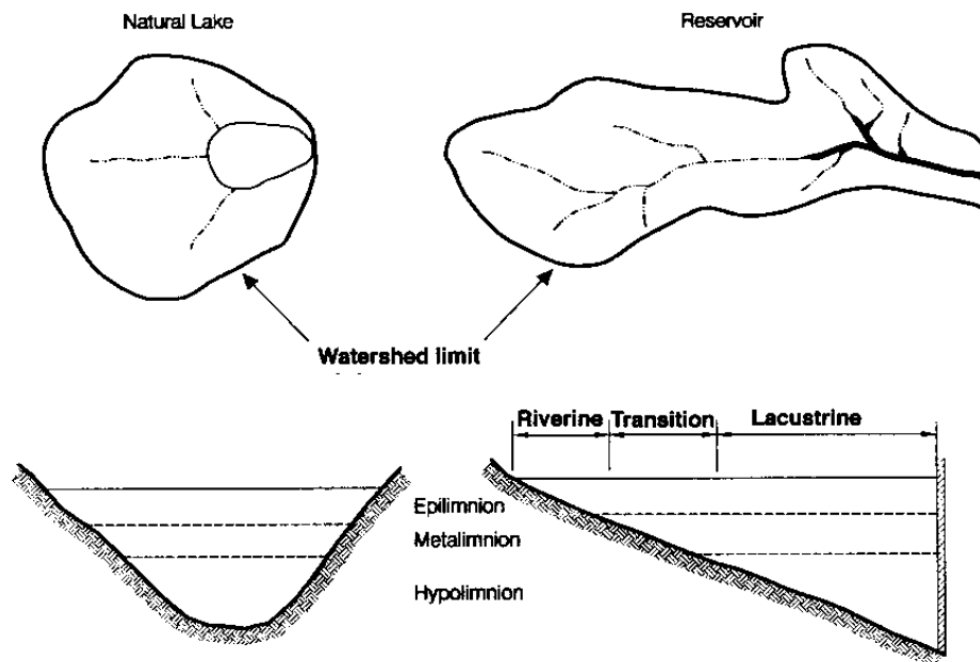
Figure 2.1: The distinct geometries of a natural lake and a man-made reservoir. The oval-shaped natural lake (left) is formed by geological factors, while the linear and dendritic shape of the man-made reservoir (right) is a result of dam construction. The reservoir's depth gradually increases towards the dam, resulting in a shallow upstream end and deeper downstream sections. Figure adapted from Morris & Fan (1998).

2.2 Water Balance in Man-Made Reservoirs

This thesis focuses on man-made reservoirs, a group of water bodies described in the previous Section 2.1, because they are crucial to societal systems, and water availability in these reservoirs is often of great importance. This section examines how the volume in the reservoir is established, specifically by discussing its water balance and elaborating on its main in- and outflows. Figure 2.1 represents the fluxes influencing the total volume contained in man-made reservoirs. The total volume present in man-made reservoirs is determined by various factors, which are presented by the dark blue arrows in Figure 2.1. These factors include the stream inflow into the reservoir, which is influenced by a variety of sources, such as river flow, upstream surface runoff caused by upstream precipitation, near-shore surface runoff, and direct precipitation. The outflow of the reservoir, on the other hand, is determined by direct evaporation, the abstraction rate, which is dependent on the water demand and operating schedule of the reservoir, as well as the discharge rate, which is again based on the reservoir's operating strategy. This strategy may involve maintaining an environmental base flow, for example. Last, although none was reported in the literature, groundwater inflows and seepage, which are affected by the groundwater piezometric head, can also influence the water balance by adding or removing water from the reservoir (Habets, 2018). The water balance is also expressed in Formula 2.1:

$$\frac{dV}{dt} = Q_{in} + P + G_{in} - Q_{out} - E - S - Q_{abs} \qquad (2.1)$$

where dV is the water volume variation (m^3) over period dt (s), Q_{in} is the stream inflow into the reservoir (m^3/s), Q_{out} is the outflow from the reservoir (m^3/s), E is the evaporation rate (m^3/s), P is the precipitation rate (m^3/s), S is the seepage rate (m^3/s), G_{in} is the groundwater inflow (m^3/s) and Q_{abs} is the water abstraction (m^3/s).
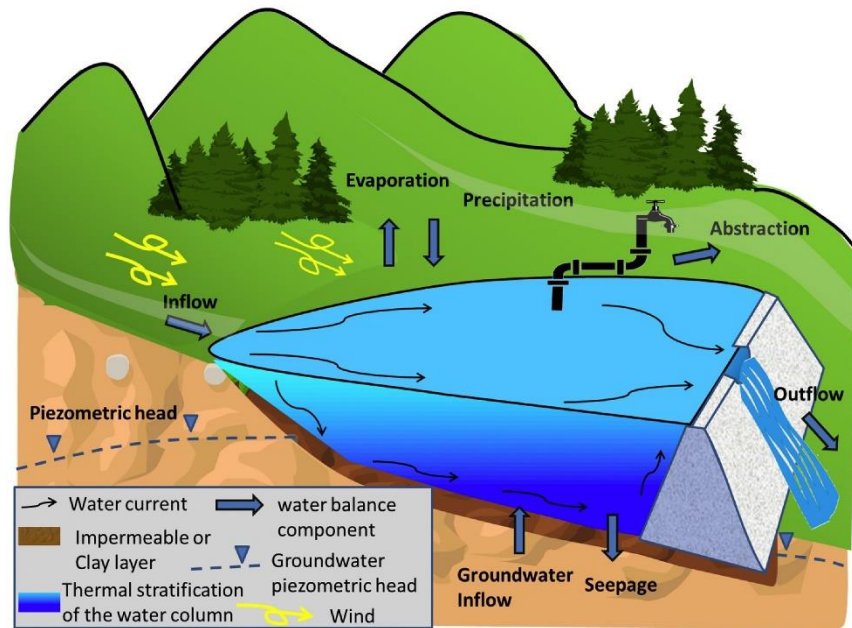
Figure 2.2: Factors influencing the total volume contained in man-made reservoirs, including incoming streamflow, upstream and direct runoff and direct precipitation. The outflow is determined by discharge, water abstraction and evaporation, water abstraction, as well as potential groundwater inflows and seepage. Figure adapted from Habets et al. (2018).

2.3   Methods to Construct a Hypsometric Curve

To determine the filling rate of a reservoir, various types of measurements can be conducted. For instance, the surface water level can be measured relative to a known datum, or the surface water area can be determined to estimate the filling rate. However, if the goal is to ascertain the available water reserves accurately, measuring or calculating the volume is likely the most useful method. The relation between these three volume indicators, water level height, surface area, and volume, can be represented in a hypsometric curve.

Creating the hypsometric curve of a reservoir traditionally involves combining in-situ water level, area and volume measurements over multiple time periods. This is typically achieved through specialised equipment such as boats or sonar echo probes during bathymetric surveys, which enable the determination of terrain elevations beneath the water surface (Becker et al., 2009; Studio Pietrangeli, 2012a; 2012b). The resulting maps from these surveys are essential in establishing the hypsometric curve including volumes. However, even though they provide the essential information, bathymetric surveys can be costly, time-consuming, and challenging due to financial reasons, safety, or political concerns as discussed in Section 1.

Reservoir hypsometric curves can be established without the need of in-situ measurements, using remotely sensed global datasets that provide surface area measurements over time, constructed by Donchyts et al. (2022), which is further elaborated on in Section 2.5. These datasets can be linked to digital elevation models (DEMs) that offer elevation measurements. Two types of DEMs are available: dynamic and static. Dynamic DEMs are long-duration missions and based on Light Detection and Ranging (LiDAR) technologies, such as the Ice, Cloud and land Elevation Satellite 2 (ICESAT-2) mission, which provides point cloud elevation measurements over time (Markus et al., 2017). Static DEMs, on the other hand, are short-term missions and offer a 3D spatial elevation map of the Earth at a single moment in time and are based on Synthetic Aperture Radar (SAR) technologies, such as the MERIT-Hydro DEM, constructed by Yamazaki et al. (2017), or the Shuttle Radar Topography Mission (SRTM) (Farr & Kobrick, 2000; Yamaguchi, et al., 1998). Section 2.4 will explore these spaceborne technologies used to construct DEMs, which are essential in the remote construction of hypsometric curves.

A type of DEM is a, so-called, 'dynamic' DEM, which offers multiple point cloud elevation measurements over time. This can be used to establish the hypsometric curve for area and elevation in a reservoir (Annor et al., 2009; Gao, et al., 2012). However, a complete hypsometric curve requires establishing such relationships throughout the entire filling rate of the reservoir, which is often limited by the insufficient number of elevation measurements available for most reservoirs. For instance, even the most recent mission providing dynamic elevations, ICESAT-2 by Markus et al. (2017), covers 93% of the known water reservoirs, yet it only provides two measurements for many of them (Cooley, Ryan, & Smith, 2021). Additionally, this method often requires knowledge of the reservoir's bathymetry to determine its associated volume. Thus, while dynamic elevations can be a useful tool for studying surface area and water level relationships, in-situ measurements remain crucial for reliable analysis of reservoirs. More detailed information about the methods employed dynamic DEMs to establish the hypsometric curve and volume time series will be provided in Section 2.6.

On the other hand, there exist 'static' DEMs, which are elevations measured in a short duration mission. So, the static DEM presents elevation for one moment in time. The static DEMs are applied in studies that utilised Hutchinson's long-hold assumption (1957) that the terrain beneath a lake surface is shaped by the same physical processes that created the terrain surrounding the lake, including in Messager et al. (2016), Heathcote, et al. (2015), Hollister, et al. (2011), Pistocchi & Pennington, (2006) and Sobek, et al. (2011), to estimate the global freshwater reserves. These studies have used static DEMs to estimate reservoir bathymetry by interpolating the elevations of the surrounding terrain, which in turn allows for the estimation of the volume in the reservoir. Although, these estimates are, as mentioned by Messager et al. (2016), not accurate enough for lake-to-lake analysis, this approach could serve as a foundation for reconstructing reservoir bathymetry. Also, for static DEMs, detailed information about methods that employed static DEMs to reconstruct reservoir bathymetry is be provided in Section 2.6.

2.4 How Spaceborne LiDAR and Radar are used in the construction of DEMs

The DEMs described in Section 2.3 were used to construct the hypsometric curve. This section aims to provide an understanding of the physical principles behind the technologies used to construct the DEMs: Spaceborne Light Detection and Ranging (LiDAR) and Synthetic Aperture Radar (SAR).

2.4.1 How LiDAR Technology Measures Surface Elevations

LiDAR operates by transmitting a laser beam to the Earth's surface, where photons are reflected and received by the satellite's receiver. The time it takes for the reflection of the laser beam to reach the satellite is used to derive the elevation of the Earth's surface. Figure 2.3 represents the point cloud measurements of ICESAT-2 in the western Pilbara region of the North West Australian coast. The photons received in the backscatter of the laser beam provide measurement points, resulting in a cloud of elevation measurements on a linear transect as shown in Figure 2.3 (Parrish et al., 2019). The laser beam pairs provide three LiDAR tracks with ~3 km spacing, which enabled Cooley, Ryan & Smith (2021) to detect 463,252 lakes for their study using ICESAT-2 observations and a global water-body mask. LiDAR has shown to provide vertical accuracies of better than 10 cm and a resolution of less than 6.5 m (Neumann et al., 2019; Alsdorf, Birkett, Dunne, Melack, & Hess, 2001; Magruder, Neuenschwander, & Klotz, 2021; Cooley, Ryan, & Smith, 2021). The frequency and wavelength of the laser beam depends on the specific LiDAR technology but is always part of the infrared and visible part of the electromagnetic spectrum. More specifically, the ICESAT-2 LiDAR beam's pulse repetition frequency is 10 kHz (~tracking every 0.7m on the ground) and its associated wavelength is 532 nm (NASA, 2019). The wavelengths indicate that laser beams do not contain enough energy to penetrate water vapour. Therefore, the LiDAR measurements can be affected by clouds in the atmosphere and does not always provide sufficient elevation data.

Noticeable is that LiDAR technology has the ability to measure depths of clear waters to some extent, but it is not sufficient for deriving lake bathymetry. Water selectively absorbs wavelengths of light, allowing the laser beam to penetrate water to a certain depth (Jerlov, 1976). Green and blue laser beams can detect seafloors up to significant depths, such as the green laser beam of the Advanced
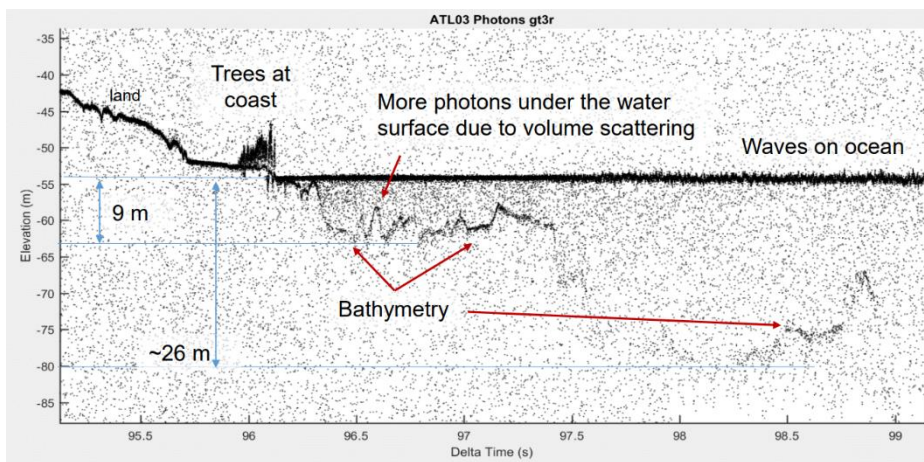
Figure 2.3: The point cloud measurements of ICESAT-2 in the western Pilbara region of the North West Australian coast. The ICESAT-2 profile shows points below the water surface, where the green laser beam of the Advanced Topographic Laser Altimeter System (ATLAS) was able to detect seafloors as deep as -38 m in very clear coastal waters, and points above the water, where the laser beam did not penetrate the water surface. This image serves as an example of the potential for LiDAR technology to measure the depth of clear waters in various locations. Figure adapted from Parrish et al. (2019).

Topographic Laser Altimeter System (ATLAS) launched in NASA's ICESAT-2 mission (2018), which detected seafloors as deep as -38 m in clear coastal waters, as shown in Figure 2.3. However, to use such seafloor detections as bathymetry measurements, correction for the air-water interface and the speed of light in the water column is required. Similarly, in a study by Arsen et al. (2014), the red laser beam of the Geoscience Laser Altimeter System (GLAS) was used to obtain the hypsometric curve of a Bolivian inland lake by measuring the elevation of the lake. However, the volume estimations could only be retrieved with measurements of the lake bottom when the reservoir was completely dry. The GLAS elevation measurements were then linked to surface area measurements from NASA's Landsat and Moderate Resolution Imaging Spectroradiometer (MODIS) missions to derive the volume. Figure 2.4 represents depth measurements of Lake Poopó, a Bolivian inland lake obtained using the GLAS red laser beam. Interestingly, GLAS measurements in clear shallow waters could reveal depth to a certain extent, as shown in Figure 2.4, but the red wavelength contains less energy than green or blue, and can penetrate water to a lesser extent. In conclusion, while LiDAR technologies may provide accurate elevation measurements in clear waters after compensating for the air-water interface, volume estimation can only be obtained when the reservoir is completely dry, which makes it difficult to apply to numerous reservoirs worldwide.

2.4.2 Comparing LiDAR Technology to SAR Technology

SAR is another remote sensing technology that has been used to measure elevations from space. Similar to LiDAR, SAR derives elevation by measuring the time it takes for a signal to travel to and return from Earth. However, SAR emits radar waves in the microwave frequency, instead of photons, which are echoed back by the Earth's surface and detected by the antenna of the satellite. This enables SAR to retrieve the distance between the Earth and the satellite and to construct a more complete dataset as SAR echo's enable a three-dimensional reconstruction of the surface elevation (Vernimmen, et al., 2020). SAR technology includes wavelengths in the range of 0.8-100 cm and frequencies between 0.3 and 12 GHz, as mentioned by NASA (2019), making it possible to penetrate water vapor and avoiding the influence of atmospheric conditions and lighting differences between day and night. SAR, therefore, is in many cases more favourable than LiDAR, although LiDAR provides higher accuracy (Neumann et al., 2019; Alsdorf et al., 2001; Magruder et al., 2021).

SAR technology can only penetrate a few millimeters into liquid water particles at higher wavelengths (<~23 cm), while LiDAR can measure a significant distance through water (Knyazev et al., 2003). Figure 2.5 represents the ensitivity of SAR wavelengths to forest structures. In SAR measurements, this phenomenon can result in artifacts, as the elevation provided would be that of the top of the vegetation rather than the terrain. To cope with these artefacts, it is recommended to use longer wavelengths for measuring surface elevation, which will penetrate the vegetation, as presented in Figure 2.5 (NASA, 2019). Lastly, interferometric SAR (InSAR) measurements are commonly used to construct global digital elevation models, which improves the accuracy of SAR. This method involves simultaneous measurements obtained by two SAR antennas on very similar positions, which increases the SAR resolution of the constructed DEM (Massonnet & Feigl, 1998).
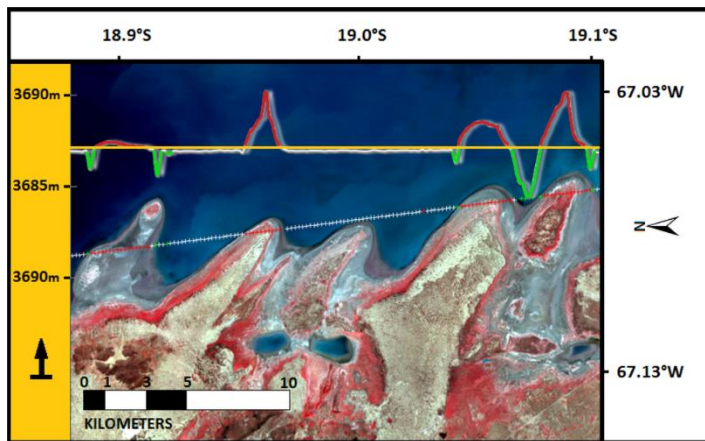
Figure 2.4: Depth measurements of Lake Poopó, a Bolivian inland lake obtained using the GLAS red laser beam, as part of NASA's first ICESAT mission. GLAS measurements of water levels were linked to surface area measurements from Landsat and MODIS missions to derive the lake's volume. The GLAS measurements in clear shallow waters could also measure its depth, despite the red laser beam's lower energy compared to green or blue wavelengths Figure adapted from Arsen et al. (2014).
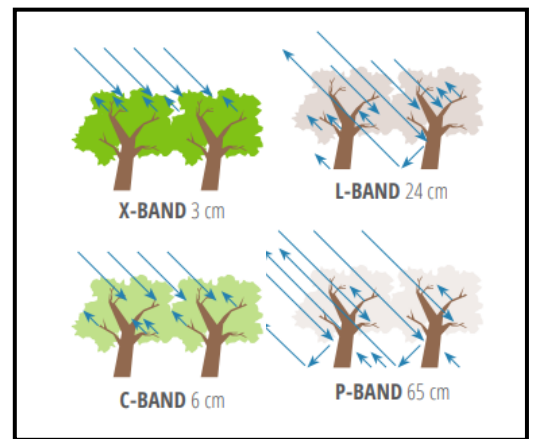
Figure 2.5: Sensitivity of SAR wavelengths to forest structures. The radar-transmitted energy penetrates into the forest canopy and reflects back from forest components such as leaves, branches, stems and underlying soil. The larger wavelengths penetrate deeper into the canopy. Figure adapted from NASA (2019).

2.5 Surface Area detection by Global Water Watch

As previously discussed in Section 2.3, the LiDAR and SAR DEMs can be used for construction of the hypsometric curve if combined with surface area measurements. Measurements of reservoir surface area can be obtained by analysis of visual imagery of satellite overpasses, for example with the use of missions like the Moderate Resolution Imaging Spectroradiometer (MODIS), NASA's Landsat program, or ESA's Copernicus program (Annor et al., 2009; Gao, Birkett, & Lettenmaier, 2012; Khandelwal et al., 2017; Donchyts et al., 2022). Most recently such surface area dynamics have been provided by the Global Water Watch initiative.

Global Water Watch provides reservior surface area dynamics and distinguishes itself from existing datasets that provide surface water area dynamics by providing information on a significantly larger group of 71,208 reservoirs, with a focus on small to medium-sized reservoirs between 0.01 and 100 km2. The group of reservoirs in Global Water Watch was constructed by harmonising different vector maps into one global dataset, including the Global Reservoir and Dam database (GRanD) by Lehner et al. (2011) and the GlObal geOreferenced Database of Dams (GOODD) database by Mulligan et al. (2020). For each reservoir, analysis is conducted using freely available data from NASA's Landsat 7 & 8 and ESA's Copernicus programs, including Sentinel-2.

The algorithm for water detection applied to construct the Global Water Watch database is presented by Figure 2.6. The Global Water Watch initiative employs a specialised water detection algorithm, as illustrated in Figure 2.6, to overcome challenges encountered in previous studies for water surface area detection in reservoirs worldwide (Khandelwal et al., 2017). First of all, Global Water Watch partially occluded satellite images due to clouds or shadows were filtered out fully or partially. Secondly, computer vision and image processing methods like Canny Edge detection and Otsu thresholding were used to delineate the reservoir pixels indicated as water. This step accounted for different spectral properties in the images that vary by location and season through calculating separate Otsu threshold for each single reservoir separately based on the Normalised Difference Water Index (however it was indicated that any other spectral index would work) (step 2 – 5). Lastly, water slope variability due to wind, water flow, or the presence of floating masses were adressed by gap filling based on the probability of surface water occurrence (step 6 – 8) (Donchyts et al., 2022). These steps combined provide near real-time surface area dynamics for man-made reservoirs of over 70.000 reservoirs worldwide.
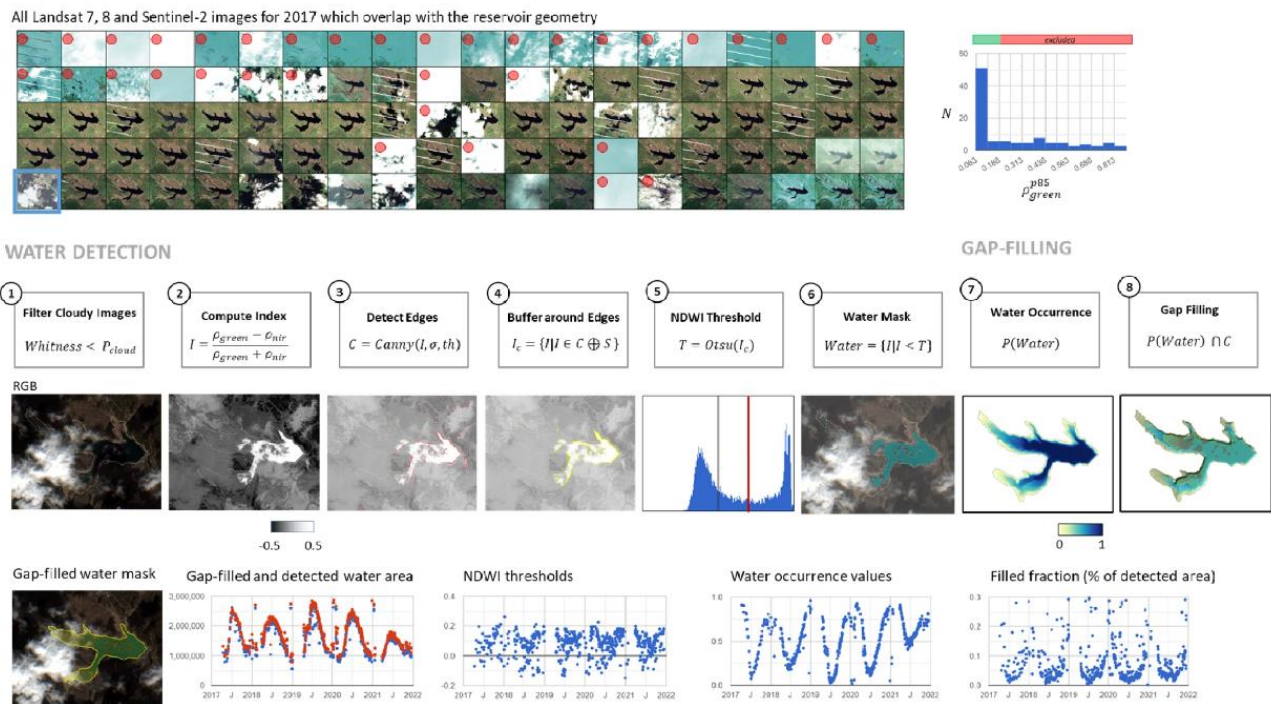
Figure 2.6: The algorithm for water detection applied to construct the Global Water Watch database involves the following steps. First (1), images that contain clouds are filtered from all Landsat 7, 8, and Sentinel-2 images that overlap with the reservoir geometry based on a threshold P_{cloud}. Then (2), the spectral water index (NDWI) is determined for each pixel, and (3) the Canny edge detection is applied to determine the water/land edge, including (4) a buffer. Next, (5) the NDWI in each detected pixel is used to determine the optimal threshold for the Otsu method, which is then used to determine (6) the surface water area. Finally, (8) a gap fill is performed to remove incorrectly detected pixels from the resulting water mask. Figure adapted from Donchyts et al. (2022).

In the developing proces of Global Water Watch in total 768 reservoirs were validated. The algorithm demonstrated high goodness of fit in daily in-situ water level and storage measurements, with a coefficient of determination r^2 greater than 0.7 for 67% of the reservoirs Therefore, the data can be used as a proxy in reservoir storage dynamics.

On a general note, the utilization of satellite imagery extends beyond the application of water detection. As encompassing studies focused on Earth's processes, such as monitoring vegetated areas worldwide by Global Forest Watch (2023), delineating the world's free-flowing rivers in a study by Grill et al. (2019), and estimating global water reserves in a study by Messager, et al. (2016).

2.5.1 Challenges in Lake Surface Area Detection

Several challenges have been identified in lake surface area detection, which still should be taken into account when it comes to shallow lakes. In a study by Gao et al. (2012) it was found that when the water level in shallow lakes decreases, the lakes leave behind small ponds that are difficult to filter from the detected water surface area, leading to an overestimation of the actual lake volume. Additionally, lakes with a large shoreline-to-area ratio, such as many man-made reservoirs, are more susceptible to uncertainties, even when the lake is relatively full, because many pixels are involved in the delineation process and each pixel introduces an additional error. Lastly, the use of altimeter-based water levels presents a challenge, as discussed earlier, due to their narrow swaths and large footprints that measure only a small percentage of the total population of lakes. Therefore, shallow lakes were found to be particularly susceptible to overestimation of the lake volume if no correction is applied to the surface area detection.

2.6   Methods for Estimating Reservoir Volumes using Digital Elevation Models

Hypsometric curve can be established with the help of DEMs, as discussed in Section 2.3. For this, three trends can be found in literature: the use of solely dynamic DEMs, the combination of static and dynamic DEMs and the use of solely static DEMs, which are discussed in Section 2.6.1, Section 2.6.2 and Section 2.6.3 respectively.

2.6.1   Establishing Volumes with Dynamic DEMs

Several studies have successfully employed dynamic DEMs to construct the hypsometric curve of lakes (Gao, Birkett, & Lettenmaier, 2012; Li, Gao, Jasinski, Zhang, & Stoll, 2019; Cooley, Ryan, & Smith, 2021). This can be done for lakes where sufficient measurements and area classifications are available, allowing for the accurate retrieval of hypsometric relations between area and elevation (Cooley, Ryan, & Smith, 2021).

The volume in Gao et al. (2012) is extracted while comparing it to the volume at capacity in the following Formula 2.2:

$$V_o = V_c - (A_c + A_o)(h_c - h_o)/2 \qquad (2.2)$$

where V_o (m³) is the estimated storage, V_c (m³) the storage at capacity, A_o (m²) the observed area, A_c (m²) the area at capacity, h_o (m) the observed height, h_c (m) the height at capacity.

The advantage of this method is that LiDAR instruments can deliver elevation measurements with high accuracies, such as the ATLAS instrument on board of NASA's ICESAT-2 mission, which provides accuracies within 3 centimetres (NASA, 2023). However, a disadvantage is that the knowledge on the reservoir at capacity is needed to derive the volume. Furthermore, the method is not always applicable to man-made reservoirs where water levels are strategically maintained at the same level and to man-made reservoirs with unknown information on lake bathymetry. Lastly, there are not always enough measurements available for the construction of a hypsometric curve (Cooley, Ryan, & Smith, 2021). Lake overpasses can be limited, or lakes can be entirely excluded from the datasets due to the spacing between the laser beams. Therefore, the method is not applicable to every reservoir worldwide.

2.6.2   Coupling Dynamic and Static DEMs

Literature shows that coupling of static and dynamic DEMs could lead to volume time series estimations in lakes. While the static DEMs provide elevation measurements at a specific moment in time, they can be used in conjunction with the highly accurate dynamic DEM measurements to estimate lake hypsometric curve. Tseng et al. (2016) developed a bathymetry method that linearly extrapolates terrain slope from a static ASTER DEM in a 3x3 kernel from the nearest grid cell on the shoreline to estimate the depth in each lake cell. In case multiple shoreline cells had the same distance to the lake cell, the average of all slopes was taken. However, this method may overestimate the lake bottom and cause extrapolation artifacts, which limits its ability to realistically mimic the lake bottom. Figure 2.7 represents The Hoover Dam segment of Lake Mead, consisting of several sub-figures that highlight the impact of linear interpolation on the DEM and Figure 2.8 represents Bathymetry map of Lake Mead constructed using the method proposed by Tseng (2016). Despite the limitations studies such as Li (2019) and Li (2020) have successfully estimated lake volume using the extrapolation method by Tseng et al. (2016), and have found an accuracy of 0.85 m for simulated water level heights in the Hoover Dam-segment of Lake Mead as also shown in Figure 2.7 and 2.8. In conclusion, the coupling of static and dynamic DEM enables to obtain the lake bathymetry and the lake hypsometric curve, which allows conversion of surface areas into volumes.
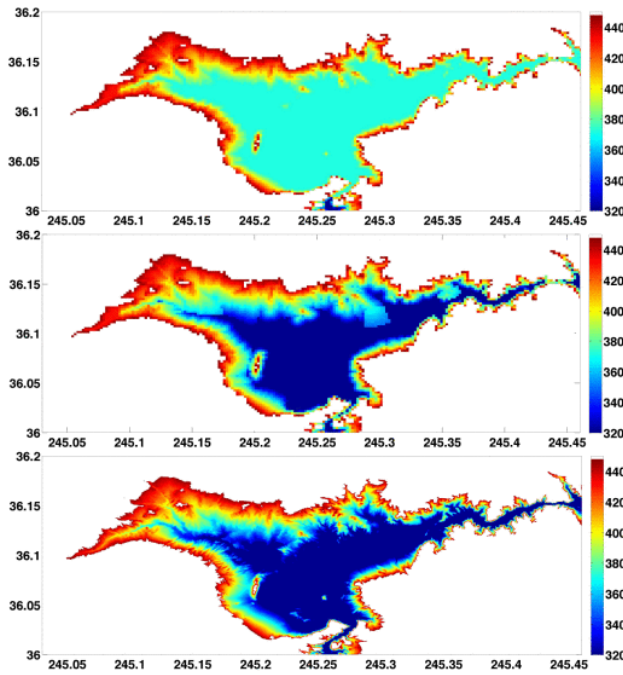
Figure 2.7: The Hoover Dam segment of Lake Mead, consisting of several sub-figures that highlight the impact of linear interpolation on the DEM (GMTED2010). The top sub-figure represents the DEM measurements without any interpolation, the middle sub-figure demonstrates the results of the linear extrapolation method proposed by Tseng et al. (2016), and the bottom sub-figure presents the actual values. This figure is adapted from Tseng et al. (2016) and is used to illustrate the interpolated results with an accuracy of 0.85 m in the Hoover Dam segment of Lake Mead.
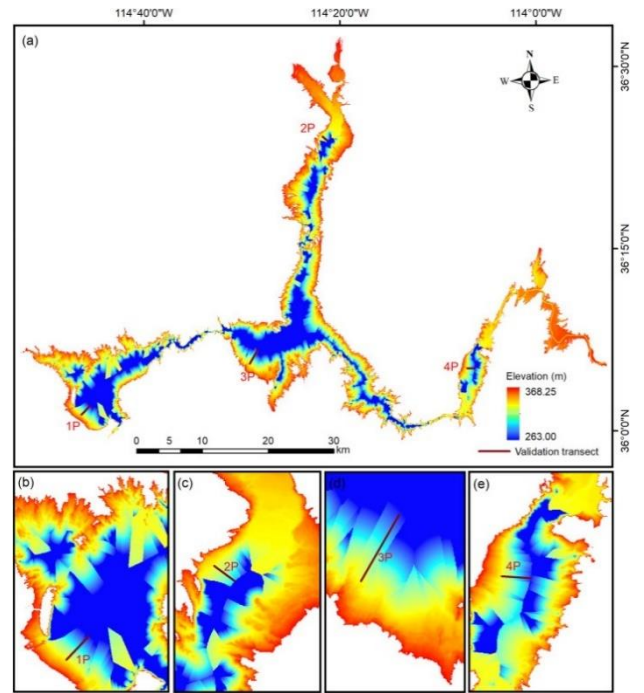
Figure 2.8: Bathymetry map of Lake Mead constructed using the method proposed by Tseng (2016), and corrected for overestimation according to Lake Mead's maximum capacity in the database by Lehner (2011). The lower figures show magnified views of specific sections of the upper figures, highlighting the interpolation artifacts. The figure was accessed through Li, Gao, Zhao, & Tseng's (2020).

These studies utilised Formula 2.3 to calculate lake volume:

$$V_n = \sum_{i=1}^{n=1} \frac{(h_{i+1} - h_i)(A_{i+1} + A_i)}{2} \qquad 2.3$$

Where V represents the volume based on the number of measured water levels n (-), the water level height of the of the ith contour is h_i (m), the surface area enclosed by the ith contour is A_i (m²) and the volume V_n(m³). To address the tendency to overestimate lake volume, Li et al. (2019) terminated the process once the lake capacity in the Global Reservoir and Dam Database (GRanD) provided by Lehner et al. (2011) was reached

2.6.3 Establishing Volumes with Static DEMs Only

Over the past three decades, literature has presented various methods for lake volume estimation based on static DEMs only (Feng, 2011). Estimating lake volumes based on static DEMs only offers the advantage of not being limited by the number of overpasses that altimetry missions make. Many studies have focused on the storage of large groups of lakes in specific regions (Håkanson & Peters 1995; Pistocchi & Pennington, 2006; Hollister & Milstead, 2010; Sobek, 2011; Hollister, Milstead, & Urrutia, 2011; Heathcote, Giorgio, & Prairie, 2015). The only global study has been conducted by Messager et al. (2016).

Earlier studies have only partially relied on DEMs, as they also included in-situ measurements of the maximum depth in the reservoir, which requires in-situ access to the lake and makes it difficult to scale

the method to a global level (Håkanson & Peters, 1995; Hollister & Milstead, 2010; Hollister, Milstead, & Urrutia, 2011; Arsen, Crétaux, Berge-Nguyen, & Abarca Del Rio, 2014).

Later studies have solely relied on data provided by the DEM, such as slope and elevation characteristics. Different slope characteristics were sampled in these methods, with Sobek (2011) and Messager (2016) applying the slope sampled at the nearest shoreline point, and Pistocchi (2006) and Heathcote (2015) using the mean slope within a buffer around the lake. Notable performances were seen in the studies of Sobek et al. (2011), Sweden and Heathcote et al. (2015), and Quebec, yet Messager et al. (2016) which showed the overall best performance.

Messager et al. (2016) conducted a successful global analysis of lake volumes, making no distinction between natural lakes and man-made reservoirs. The region of interest for each lake in the DEM was delineated and divided in grid cells. The slope was derived for every cell based on the difference in elevation between neighbouring cells. Potential outliers were smoothed by recalculating the mean slope in a 3x3 neighbourhood for each cell. The lake depths were determined by multiplying the slope sampled at the nearest grid cell on the shoreline and the distance towards that grid cell, with the average depth representing the mean lake depth. The resulting mean lake depths were validated against 173 European lakes in a variety of geomorphologic settings, mostly clustered in the Baltic countries, the Alps, and Ireland. The results were prone to overestimation of the lake depth. In Messager et al. (2016) it is believed that this overestimation can be reduced by reconstructing the flattening of the lake bottom towards their centre. Additionally, it should be noted that the volume estimates relate to aggregated global or regional lakes, and the accuracies do not allow for single lake-to-lake analysis.

2.7 The Impact of Sedimentation in the Lake Bottom

Reservoir sedimentation significantly impacts the global water storage capacity, as it replaces 0.5-1% of the capacity annually, which was mentioned by White (2000) and Trimble (2012) and should therefore be accounted in storage estimation models. The extent of sedimentation in lakes depends on various factors in the hydrology of catchments and characteristics of river basins. Principally the reduced kinetic energy of the river flow, for example because of dam construction or a sudden natural impoundment, reduces transport of sediment in the river and thereby causes gradual sedimentation. This significantly impacts reservoirs beds (Dargahi, 2012). Figure 2.9 shows the longitudinal sedimentation profile of the Dez Reservoir. Sedimentation processes are complex and highly influenced by turbidity currents within the lake. However, often they strengthen the flattening of the lake bed to the middle and, in case of man-made reservoirs, towards the dam as shown in the example of the Dez Reservoir in Figure 2.9 obtained from Li et al. (2019) successfully introduced the concept of flattening the lake bottom, which is strenghtened by sedimentation, to their volume estimation method that translates areas into volumes. They stopped the linear extrapolation process once associated volumes matched the reference values for maximum capacity, as presented in previously shown Figure 2.7. This approach corrected for the overestimation caused by linear extrapolation, however this cannot be upscaled to a global level as maximum capacity values are not widely available for every reservoir worldwide.
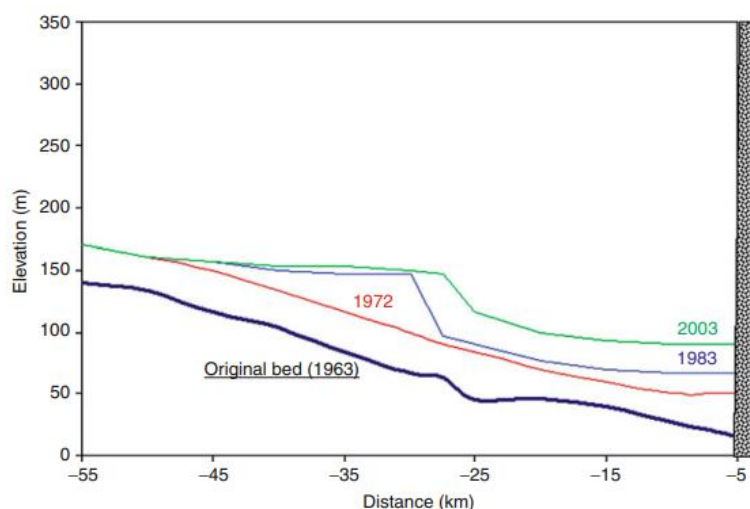
Figure 2.9: The longitudinal sedimentation profile of the Dez Reservoir from 1963 to 2003, showing a uniform sedimentation layer in the intial 9-year period followed by flattening of the bottom. The figure was accessed through Dargahi (2012).

Figure 2.10 represents an illustration of the misalignment of elevation in the centre of a lake. Messager et al. (2016), the benchmark study in for this thesis, made several attempts to introduce the flattening of the lake bottom with the goal to mimic more realistically the lake bed. The gains in predictive power were not consistently observed, possibly due artefacts in the centre of the lake where elevations do
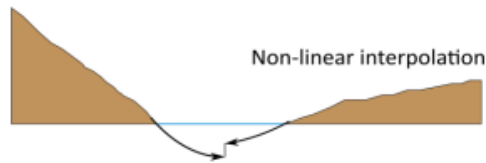
Figure 2.10: An illustration of the misalignment of elevation in the centre of the lake as an effect of the interpolation of slope towards the center according to Messager et al. (2016), which includes a parameter for flattening of the lake bottom. Figure adapted from Messager et al. (2016).

not align with each other, as illustrated in Figure 2.10.

The attempts included a power function in the calculation of the topographic depth, which account for the flattening of the lake bottom. Formula 2.2 is used to determine the topographic depth in each cell:

$$D_t = d^k \tan(s) + C \qquad (2.2)$$

where D_t (m) represents the topographic depth, d denotes the distance (m) towards the grid cell on the shoreline, s (rad) represents the allocated slope sampled in the nearest shoreline grid cell, and C (m) represents the datum (reference elevation). The k (-) component introduces the flattening, and the values 0.95, 0.97, and 0.99 were explored. Additionally, attempts were made with various mean slope values sampled in a buffer up to 1000 meters around the lake.

2.8 Models for Prediction of Water Availability

The previous sections have focused on estimating the current volume state of a reservoir, providing valuable information about the current water availability. This information could benefit decision making in anticipatory actions. However, this data may not provide sufficient time to take the actions. Therefore, predictions are necessary for early indications lacking water availability.

Over the years, models have been utilised to forecast water availability by converting hydrological observations and forecasts into predictions. The models comprised various fluxes, such as evaporation, runoff, transpiration, infiltration, percolation, discharge, condensation, and states including volumes in glaciers, aquifers, reservoirs, ice sheets, clouds, and lakes (Sene, 2010). Two distinct approaches can be taken for this: process-based modelling, as discussed in Section 2.8.1, and data-driven modelling, as discussed in Section 2.8.2.

2.8.1 Process-Based Models

Process-based models could be physically based models or conceptual models. Depending on the modelling objectives, studies can choose the appropriate approach to suit the modelling purpose.

Physically based models, also known as mechanistic models, are constructed using a bottom-up approach by dividing the distributed catchment into smaller grid cells assumed to be small, continuous, and homogenous control volumes (Hrachowitz, 2017). Physical processes within each cell are described using the Navier-Stokes equation for fluid movement in porous media, conserving mass, momentum, and energy. These models provide high degrees of spatial and process detail, but correctly describing the heterogeneous characteristics of each grid cell can be a significant challenge, requiring large computation power. Catchments are inherently heterogeneous, making it difficult to

realistically describe them as homogeneous in the model. Therefore, ideally, to accurately describe the catchment, physically based models would extreme large amounts of samples, which is difficult to achieve (Hrachowitz, 2021). Examples of physically based distributed models include DHSVM (Wigmosta et al., 1994), MIKE-SHE (Refsgaard and Storm, 1996), PARFLOW (Kollet & Maxwell, 2008), CATFLOW (Zehe et al., 2001), HYDRUS-3D (Šimunek et al., 2008), CATHY (Camporese et al., 2010), HydroGeoSphere (Jones et al., 2006) or PIHM (Qu and Duffy, 2007).

Conceptual models, on the other hand, follow a top-down approach by describing the system starting from the overall system response. For instance, lumped models represent the catchment as one entity, while semi-distributed models distribute the model into smaller entities based on catchment characteristics but in a less extreme way than in distributed models. Lumped conceptual models include unit hydrograph (Sherman, 1932), HBV (Bergström, 1976), or SUPERFLEX (Fenicia et al., 2011). Semi-distributed conceptual models, such as FLEX-Topo (Gharari et al., 2014), HYPE (Lindström et al., 2010), NWSSacramento (Burnash, 1995), GR4J (Perrin et al., 2003) or VIC (Liang et al., 1994), account for spatial heterogeneity in a less extreme approach than in distributed models by considering multiple larger entities within one catchment based on its characteristics. These models have the potential to efficiently accommodate organizational features and their temporal evolutions (Savenije & Hrachowitz, 2017).

In conceptual models, it is important to consider the concept of equifinality, which refers to the existence of multiple ways to model the same output, making it difficult to determine which approach provides the most accurate physical representation of the system. Equifinality arises due to the presence of unobservable parts of the system, the uncertainties associated with available observations, or when models are calibrated with a single aggregated error metric that compresses multidimensional problems into a single value. To account for equifinality, the parameter space and degrees of freedom in the model can be reduced, or individual parameters can be calibrated to compensate for errors in other parameters and uncertainties in other parts of the model. The reduction of parameters or the expansion of validated outputs can help to minimise equifinality in conceptual models (Hrachowitz, 2021).

2.8.2 Data-driven models

Data-driven models offer an alternative approach to hydrological process-based modelling by relying on empirical relationships, statistics, or machine learning techniques, whereas process-based models are based on physical principles. The advantage of data-driven models is their ability to extract information from data series, providing an alternative when computational speed is critical, or underlying relationships are poorly understood (UNESCO, 2005). The models process information in a 'black-box' method, where the output is based on a combination of the inputs values. Linear regression is a common approach for data-driven models, as it is simpler to use and interpret. However, non-linear regression may be necessary if the specific curve being modelled does not fit a linear relationship (IBM, 2021). Data-driven models include a variety of methods, such as (multi-)linear regression, autoregressive, decision tree models, random forest models, artificial neural network models, long short-term network models, and Bayesian network models.

The primary advantage of data-driven models is their ability to detect previously unknown relationships between variables, without requiring prior knowledge of the catchment. They provide a relatively straightforward means for modelling catchment characteristics (Hrachowitz, 2021). However, long series of training data is required to accurately calibrate these models. Furthermore, as these models are not based on physical principles, they run the risk of violating fundamental thermodynamic laws (e.g., Navier-Stokes) and the causality of relationships between variables is not always guaranteed. Due to this, so-called, 'black-box' approach, the resulting structure of a data-driven model does not offer any insight into the inner workings of the system, but only offers the model's output.

2.9   Linear Regression Models for Man-Made Reservoirs

Linear regression models are widely used in data-driven modelling due to their simplicity and interpretability (UNESCO, 2005). These models can also be applied to estimate volume dynamics in man-made reservoirs, with the selection of model type depending on the input variables used in the modelling process. The volume time series can be explored using an autoregressive model, as discussed in Section 2.9.1, and additional information based on other time series variables can be explored using a multi-linear regression model, as outlined in Section 2.9.2.

2.9.1   Brief Introduction to Autoregressive Models

Autoregressive models have been widely utilised for predicting hydrological time series since 1960, including streamflow forecasting in a study by Li et al. (2015), rainfall forecasting in a study by Burgan (2016), and volume estimations in a study by Chen & Boccelli (2014). Figure 2.11 represents The tge concept of an autoregressive model. Autoregressive models are a type of data-driven model commonly used in time series analysis. In such models, the output variable is modelled as a linear combination of its past values. This means that, like presented in Figure 2.11, the current value of the variable depends on its previous values, which allows the model to capture the patterns and trends in the time series data. The autoregressive model is a simple yet powerful tool for predicting future values in a time series. It can be used to identify and model trends, seasonality, and other patterns in the data. Additionally, it is an interpretable model since the coefficients that represent the impact of past values on the current value are easy to understand (Brownlee, 2017).
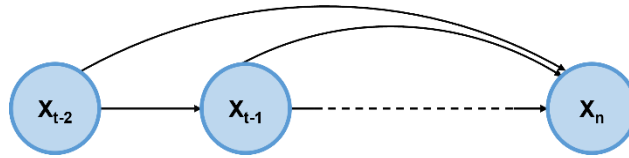
Figure 2.11: The concept of an autoregressive model, where a linear combination of the past values in the time series (x_{t-2}, x_{t-1}) of the dependent variable are used to describe the new dependent variable. To illustrate, in this Figure, the model uses two past values, yet this should be determined with the lagged correlation in the time series.

To build an autoregressive model, each historic input value is assigned a coefficient, which is optimised through ordinary least squares with the training data. The number of historic inputs taken along in the regression model is depended on the lagged autocorrelation, which is elaborated on in Section 2.9.3. The model is then used to make predictions about future values of the variable based on the previous values. The trends in the data which are not described by the autoregressive memory is referred to as 'white noise' and described by the error. The accuracy of the model can be evaluated by comparing its predictions to the actual values in the test data set. The autoregressive model is described in Formula 2.3:

$$X_t = b_0 + \beta_1 X_{t-1} + \beta_2 X_{t-2} + \cdots + \beta_i X_{t-i} + \varepsilon_t \qquad (2.3)$$

where X is the dependent variable, b_0 is the intercept, where i represents the number of preceding timesteps t in the autoregressive model. $X_{t-1}, X_{t-2}, \dots X_{t-i}$ are the values associated with the preceding timesteps and $\beta_1, \beta_2, \dots \beta_i$ (-) represent their associated weights. Last, ε_m is the uncertainty or "white noise" that comes with the prediction in the respective timestep.

2.9.2 Brief Introduction to Multi-Linear Regression Models

Multi-linear regression models are a type of data-driven models that are commonly used to estimate the relationship between multiple explanatory variables and a single dependent variable. Figure 2.12 shows the concept of an multi-linear regression model. They have been applied in hydrological time series predictions (McGuire et al., 2006; Kim et al., 2018). Unlike autoregression models, which only use the historical values of the dependent variable to make predictions, multi-linear regression models incorporate a range of additional explanatory variables that may influence the dependent variable as shown in Figure 2.12.
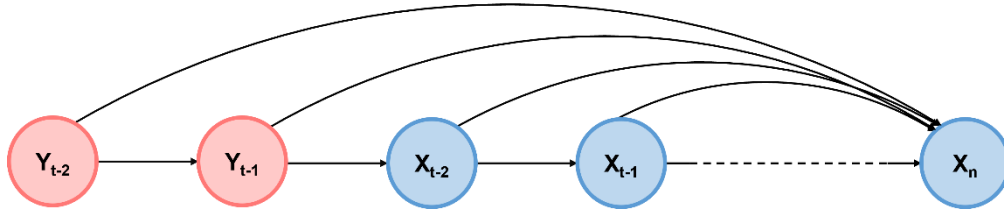
Figure 2.12: The concept of an multi-linear regression model, which is an extended version of the autoregressive model in Figure 2.11. The main difference is that the predicted value X_n of the dependent variable is obtained by a linear combination past values of multiple explanatory variables ($y_{t-2}, y_{t-1}, x_{t-2}, x_{t-1}$). To illustrate, in this Figure, the model uses two past values for both variables, yet the exact amount of input values is determined by the lagged correlation between the input and output variables.

The multi-linear regression model functions similarly to the autoregressive model, in that it assigns coefficients to each input variable using ordinary least squares fit, while the white noise component represents the unexplained trend in the data. Formula 2.4 can be used to express the multi-linear regression model:

$$X_t = b_0 + \beta_1 Y_{t-1} + \beta_2 X_{t-1} + \cdots + \beta_i Y_{t-i} + \beta_i X_{t-i} + \varepsilon_t \qquad (2.4)$$

where Y_{t-i}, and X_{t-i} represent the explanatory and dependent variables, respectively, in the ith month preceding the respective month. The weights associated with each variable value are represented by $\beta_1, \beta_2 \dots \beta_i$ (-). b_0 is the intercept, and ε_m is the 'white noise' or uncertainty in the prediction at the respective timestep t.

2.9.3 The Number of Inputs Depends on the Lagged Correlation

The number of input values utilised in autoregressive and multi-linear regression models is determined by the lagged correlation between the input time series and the dependent variable. The autoregressive model assesses the internal correlation, while the multi-linear regression model considers the correlation between the lagged explanatory variables and the dependent variable. Formula 2.5 can be used to calculate the correlation coefficient:

$$r = \frac{\sum \left(\left(x_i - \frac{1}{n} \sum_{i=1}^{n} x_i \right) \left(y_i + \frac{1}{n} \sum_{i=1}^{n} y_i \right) \right)}{\sqrt{\sum \left(x_i - \frac{1}{n} \sum_{i=1}^{n} x_i \right)^2 \sum \left(y_i + \frac{1}{n} \sum_{i=1}^{n} y_i \right)^2}} \qquad (2.5)$$

where r is the correlation coefficient for each single lag, x the value of the dependent variable, y the value of the lagged variable, and n the total number of lagged variables. The correlation coefficient ranges between -1 and 1, with values close to these extremes indicating a strong correlation and values close to 0 indicating a weak correlation. Values that exceed the range in which 95% of the values fit, are considered to vary significantly from zero correlation and can be included in the regression model. The points within the range are not considered to vary significantly from zero corelation and are likely to be "white noise" in the time series. The band including 95% of all values can be calculated according to Formula 2.6 in which n is the length of the time series:

$$\text{band}_{95\%} = \frac{\pm 1.96}{\sqrt{n}} \qquad (2.6)$$

2.10 Assessing the gained Forecasting Skill

To forecast the volume in man-made reservoirs, a wide range of model constructions can be explored, incorporating infinite variations of variables. To determine the best-performing model for a particular type of prediction, skill scores are often used. Skill scores quantify the improvement in forecast accuracy relative to a perfect forecast. The purpose of these scores is to provide a measure of how much better a given forecasting system performs compared to a reference system (Wheatcroft, 2019). By comparing all models to the same reference system, skill scores enable effective comparison of each model's performance. Skill scores are conventionally calculated using Formula 2.7:

$$\text{skill score} = \frac{A_f - A_r}{A_p - A_r} \qquad (2.7)$$

where A_f and A_r represent the accuracy of the forecasting model being evaluated and the reference data, respectively, and A_p represents the accuracy of a perfect forecast. The Heidke Skill Score is a measure used to evaluate the overall skill of prediction in the context of binary categorical problems. For categorical variables, the forecast is the prediction of the occurrence within a predetermined range of values such as for example, in regional climatological forecasts, occur in categories named 'above normal', 'normal' and 'below normal' (Chandimala & Zubair, 2007; EUMeTrain, 2023). Figure 2.13 shows the contingency matrix that classifies the forecasting outcomes into four categories: 'hit', 'miss', 'correct rejection', and 'false alarm'. In the score there are four possible outcomes considered, which are presented in Figure 2.13: hits, false alarms, misses, and correct rejections. A hit occurs when a prediction correctly identifies an event that falls below a predefined threshold. A false alarm occurs when a prediction identifies an event that does not actually fall below the threshold. A miss occurs when a prediction fails to identify an event that does fall below the threshold. Finally, a correct rejection occurs when a prediction correctly identifies that no event falls below the threshold. The Heidke Skill Score evaluates a model's performance by counting the occurrences of each possible outcome. The Heidke Skill Score is calculated using Formula 2.8:

$$\text{Heidke Skill Score} = \frac{2(ad - bc)}{(a+c)(c+d) + (a+b)(b+d)} \qquad (2.8)$$

where, a represents the number of hits (true positive), b represents the number of false alarms (false positive), c represents the number of misses (false negative), and d represents the number of rejections (true negative). The score indicates the proportion of correctly forecasted observed values relative to what would be expected by chance. A perfect forecast is indicated by a value of 1, while a score of 0 indicates no skill. A negative score suggests that the forecast performs worse than a forecast by chance.

		True value (observation)	
		Positive (1)	Negative (0)
Modelled forecast	Positive (1)	Hit	False Alarm
	Negative (0)	Miss	Correct Rejection

Figure 2.13: The contingency matrix that classifies the forecasting outcomes into four categories: 'hit', 'miss', 'correct rejection', and 'false alarm'. A 'hit' occurs when the model correctly forecasts an event to occur, a 'miss' occurs when it fails to forecast the occurrence of the event, a 'correct rejection' occurs when it forecasts the non-occurrence of the event, and a 'false alarm' occurs when it incorrectly forecasts the occurrence of the event that does not happen. The Heidke Skill Score (HSS) is then calculated using the number of hits, false alarms, misses, and correct rejections. This score provides a measure of the model's performance.

3

Methods

The methods chapter of this thesis presents the techniques used in this study to derive reservoir bathymetry, benchmark the novel method, and the method to test the predictive skill in regression models that predict water availability. In Section 3.1, the method to derive reservoir bathymetry in a novel way by utilising digital elevation models is explained. Section 3.2 elaborates on the method used to benchmark the novel method to existing methods established by Messager et al. (2016). Section 3.3 presents the method used to explore the predictive performance for water availability using regression models. Section 3.4 introduces the case study and the datasets applied. Overall, this chapter provides a detailed overview of the methodology used to analyse the reservoirs and their associated water availability.

3.1 Estimating Water Volumes in Man-made Reservoirs

The aim in this first part of this thesis is to construct and test a method that can transform water surface area time series of any reservoir worldwide into volume time series by reconstructing bathymetry from static digital elevation datasets. Thereby the first research question in this thesis is addressed.

The method involves combining radar altimetry datasets with surface water observations from Global Water Watch, constructed by Donchyts et al. (2022), to generate a hypsometric curve for every specific reservoir. The elevation data utilised in this research is sourced from the hydrologically adjusted Multi-Error-Removed Improved-Terrain Hydro (MERIT-Hydro) digital elevation model (DEM), which is a static DEM (Yamazaki et al., 2017). This is obtained via HydroMT, an automated and reproducible tool for model construction and analysis (Eilander et al., 2023). To evaluate its performance, the coefficient of determination and relative error have been computed for reservoir filling states of 25%, 50%, 75%, and 100% of maximum capacity. The approach is visually represented in Figure 3.1 and further expanded in the subsequent sections.

3.1.1 The MERIT-Hydro Digital Elevation Model as a Base

The novel method relies on data obtained from the global MERIT-Hydro DEM (Yamazaki et al., 2017). The publicly accessible DEM has a resolution of roughly 90 meters (3 arc-sec), covering latitudes between N90 and S60, and is referenced to WSG84 and the EGM96 geoid. The resolution of this DEM, relative to the size of the reservoirs within the dataset (which range from 0.1-100 km^2), is sufficient for creating a distributed model. MERIT-Hydro is constructed from the MERIT DEM and comprises smoothed elevations in water surfaces, with most outliers removed. The hydrological adjustment has considered and corrected for the input elevation data errors resulting in dummy depressions in the DEM. Additionally, the location of the river streamlines has been realistically aligned with the existing global river channel data obtained from satellites. The hydrological correction of the DEM has made the MERIT-Hydro DEM suitable for flow-direction calculations, which is a critical requirement for the novel method, as discussed further in Section 3.1.3.
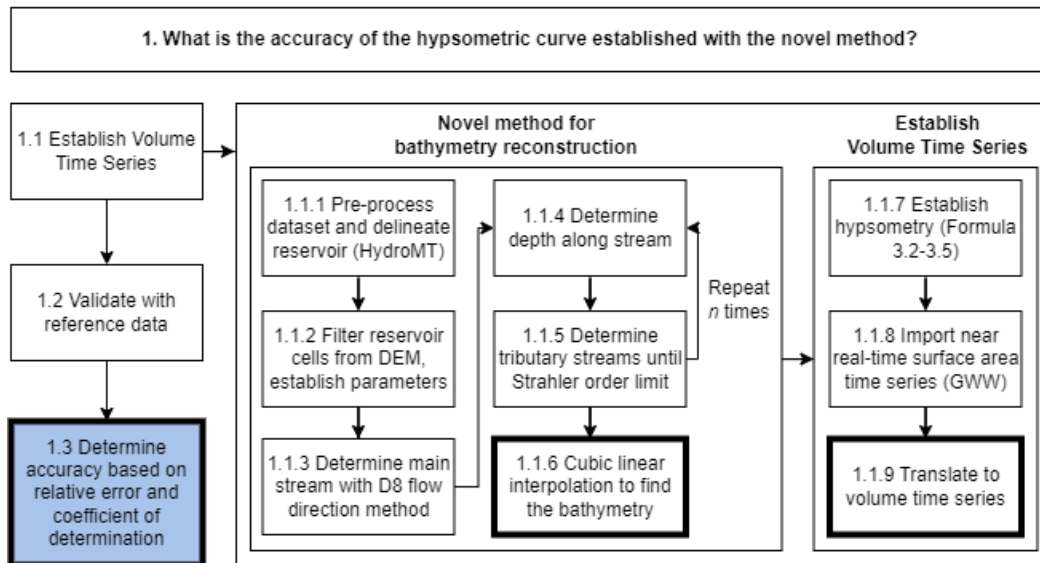
Figure 3.1: A conceptual representation of the methodology employed to answer the first research question, which comprises of three main components: retrieving volume time series (1.1), the validation process (1.2), and performance assessment (1.3). The method to retrieve volume time series (1.1) involves several steps that can be broadly divided into two phases. In the first phase, the reservoir bathymetry is constructed using a novel method, which is elaborated further in Section 3.1.3. This involves pre-processing elevation, slope, and flow direction data using HydroMT (1.1.1), an automated and reproducible tool for building and analyzing models (Eilander et al., 2023). Additionally, the reservoir data is filtered (1.1.2), and the original river stream is determined (1.1.3), followed by the determination of depth in each cell (1.1.4). Subsequently, tributary streams are delineated (1.1.5), and their depths are determined in a repeatable process until streams that deviate five Strahler orders from the main stream are identified. Lastly, the remaining elevations in the reservoir bathymetry are obtained using cubic linear interpolation. In the second phase, the reservoir hypsometric curve is constructed based on Formula 3.2-3.4 presented in Section 3.1.4. This curve is then used to translate the imported surface area data from Global Water Watch (1.1.8) into volume time series (1.1.9).

3.1.2 Why Reservoir Bathymetry is Reconstructed

A methodology to derive volume time series for a reservoir without requiring in-situ measurements involves the reconstruction of the reservoir's bathymetry through the use of a DEM, establishing a hypsometric curve, and subsequently translating surface area data into volume time series. This process relies on the fundamental assumption that the physical processes that shape the surrounding terrain also influence the bathymetry of a lake, as outlined by Hutchinson in (1957). Accordingly, interpolation of the surrounding DEM can effectively estimate the bathymetry of the lake. The assumption is supported by previous studies, which are discussed in Section 2.6, in similar domains (Pistocchi & Pennington, 2006; Hollister et al., 2010; Heathcote et al., 2015; Messager et al., 2016). From these studies, the method proposed by Messager et al. (2016) has shown to perform significantly better compared to other studies that employ a similar approach (Pistocchi & Pennington, 2006; Hollister & Milstead, 2010; Heathcote, Giorgio, & Prairie, 2015). Therefore, the proposed method in this thesis is based on the approach suggested by Messager et al. (2016), which relies solely on parameters derived from DEMs to estimate volume and has the advantage of not requiring in-situ access to the lake, thus making it easy to scale-up or apply in various (inaccessible) locations.

In addition to the method by Messager et al. (2016), this thesis argues that man-made reservoirs require a different approach than natural lakes due to the fundamental differences in their geometry, which were previously discussed in Section 2.1 (Morris & Fan, 1998). Messager et al. (2016) made no distinction between natural lakes and man-made reservoirs yet applied their method to the entire population of lakes. However, unlike natural lakes, the depth in man-made reservoirs increases

towards the dam wall. This is information that can be utilised to make a more sophisticated volume estimations in man-made reservoirs. As a result, the newly proposed method outlined in this thesis is tailored specifically for man-made reservoirs that exhibit this characteristic.

Datasets obtained through radar altimetry provide access to valuable information regarding the characteristic of the reservoir mentioned earlier. For instance, such datasets can reveal a distinct elevation shift at the location of the dam wall. By calculating the difference in elevation between the water level and the bottom of the dam wall, which is assumed as the maximum depth of the reservoir, the volume of water stored is be estimated. This approach provides a reliable means of reconstructing the reservoir bathymetry.

3.1.3 Steps in Constructing Reservoir Bathymetry

Accurately estimating the volume of a reservoir requires determining its bathymetry as the first step. As discussed in Section 3.1.1, this can be achieved using the MERIT-Hydro DEM as a base. The method relies on several parameters extracted from the DEM, such as the dam wall location, the flow direction, elevation difference covered by the dam wall, nearest upstream shoreline cell, and slope sampled in the nearest upstream shoreline terrain. These parameters are utilised in the method, as presented in Figure 3.2, to reconstruct bathymetry in individual reservoirs. Adopting this approach serves as the basis for estimating reservoir volume.

1. The reservoir and its surrounding terrain are initially delineated from the DEM (see Figure 3.2: *Step 1*). This is done with the use of the HydroMT software, developed by Eilander et al. (2023), which generates a raster with cells representing the elevations of the reservoir and its surrounding terrain based on a georeferenced location, which is retrieved for the specific reservoir through the Global Water Watch platform (Donchyts et al., 2022). To account for potential uncertainties in the delineated area, a buffer of 500 meter was introduced in the delineation process.

2. Subsequently, the cells that represent the reservoir surface are filtered from the raster (see Figure 3.2: *Step 2*). The cells are identified by a group of cells with similar elevation values. Also, other parameters are identified like the dam wall location, the flow direction, elevation difference covered by the dam wall, nearest upstream shoreline cell, and slope sampled in the nearest upstream shoreline terrain.

3. Then a main stream in the reservoir is estimated, which approaches the original river stream, based on the flow directions calculated with the D8 flow direction method (see Figure 3.2: *Step 3*). This method was originally proposed by O'Callighan and Mark (1984) and later applied by Jenson and Domingue (1988). In this method, the flow
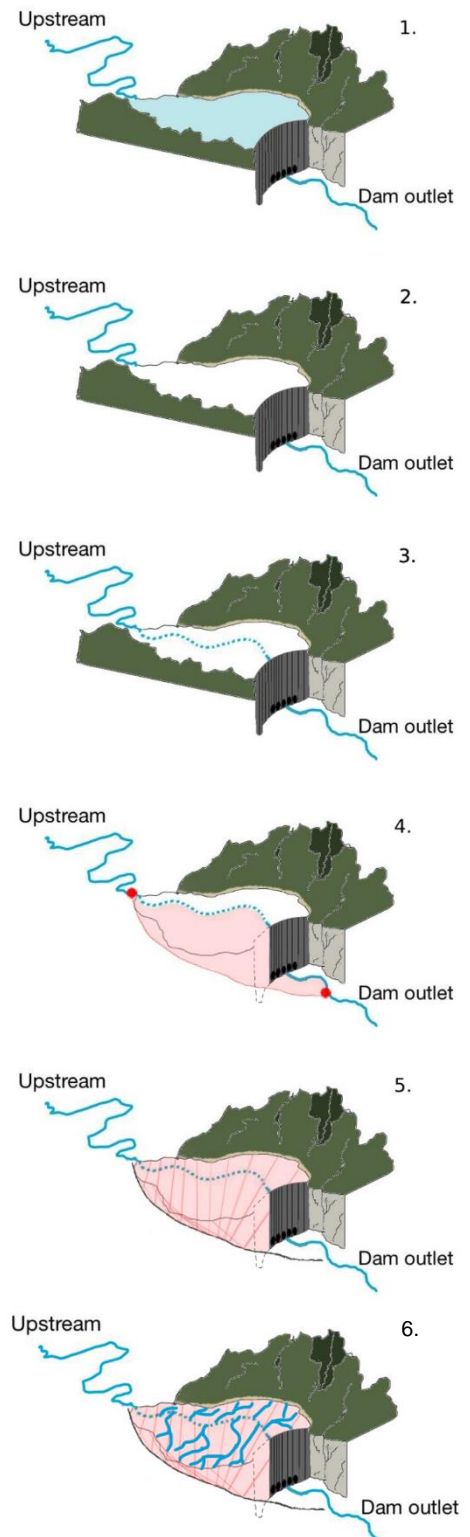
Figure 3.2: A visual illustration of the novel method, with the aim to conceptually explain the approach employed in deriving reservoir bathymetry. First, reservoir is delinated and filtered from the DEM (1-2). Subsequently, the identification of the main axis of the reservoir is established based on the flow directions (3), following the establishement of the topographic depth on the main axis (4). Furthermore, tributary axis are drawn in the reservoir, and associated elevations are derived (5). Cubic linear interpolation of the remaining cells results in the final bathymetry (6).

direction in a cell is determined based on the orientation of the neighbouring cell with the steepest descent, as shown in Figure 3.3. Compared to other flow direction methods such as D-Infinity or Multi Flow Direction, which consider the landscape curvature and flow into multiple neighbouring cells, the D8 method is less computationally intensive and faster (Tarboton, 1997; Qin, Zhu, Li, Zhou, & Yang, 2007). However, in cases where there is no clear flow direction, as in flat areas like the water surface of the reservoirs, a cell is assigned the flow direction towards the cell that does not lead towards a local depression after multiple steps. The main river stream obtained serves as the foundation for the reservoir bathymetry.
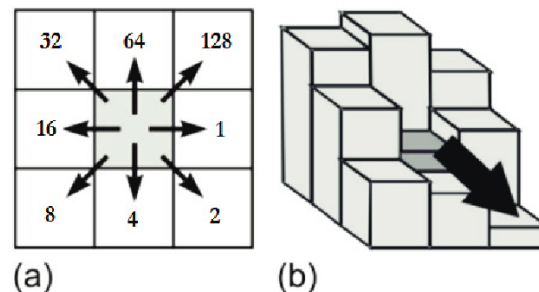
Figure 3.3: Illustration of the D8 flow direction method as introduced by O'Calligan and Mark (1984). The surrounding cells are assigned consequtive values in the power of 2, which function as directional coordinates. The lowest elevation in the neighborhood determines the actual flow direction if not leading to a local depression (b). This principle is used to reconstruct the stream network in the cells that represent the reservoir in step 3. The figure is adapted from Buarque et al. (2015).

4. In the next step (Figure 3.2: *Step 4*), the depth along the main stream is determined using Formula 3.1, while incorporating the reservoir-specific flattening parameter k (-). The purpose of introducing this parameter is to partly compensate for sedimentation in the reservoir. Unlike the approach by Messager et al. (2016), the novel method orients the flattening towards the dam wall instead of the centre of the lake. With that, this approach avoids bathymetry artefacts in the centre of the reservoir like those previously discussed in Section 2.7 and illustrated in Figure 2.9a. To simulate calculate the topographic depth on the main stream, the previously presented Formula 2.2 is used:

$$D_t = d^k \tan(s) + C \qquad (2.2)$$

    where D_t (m) is the topographic depth, d (m) the distance from the nearest cell upstream of the reservoir, s (rad) the sampled slope in that cell, C (m) its datum (reference water level), and k (-) the flattening parameter. The latter parameter is determined separately for each reservoir through a non-linear fit of the elevation sampled upstream of the reservoir and the elevation sampled within a 500 meters buffer downstream of the dam. The fit is optimised to match the slope s (rad) sampled in the nearest onshore upstream cell. These characteristics are derived from the surrounding terrain, suggesting that reservoirs in similar terrains are likely to have similar flattening parameters.

5. In addition, tributary streams are identified using a similar approach to step 3 (Figure 3.2: *Step 5*). The D8 flow direction method was utilised to locate tributary streams with Strahler orders that deviated up to 5 orders lower than the Strahler order identified in the main stream of the reservoir. The process in step 4 is then repeated for each tributary stream to determine its topographic depth. Consequently, a new parameter b (-) is obtained for each tributary, which involved the slope and elevation sampled at the nearest onshore cell upstream of the tributary stream and the elevation sampled at the intersection with the main stream.

6. Finally, the depth of the remaining cells is determined through a linear interpolation of the known bathymetry values on a grid (Figure 3.2: *Step 6*). This step yields a new elevation value for each cell, representing the final reconstruction of the reservoir bathymetry. With this step, the process of constructing the bathymetry for the specific reservoir is completed, paving the way for further steps towards determining the volume of the reservoir.

3.1.4 Modelling the Hypsometric Curve

The bathymetry in a reservoir, which can be reconstructed according to the previously proposed method in Section 3.1.3, provides a foundation for the establishment of the hypsometric curve, which represents the relationship between volume and area for a range of water levels. The reservoir area A (m²) for each water level h (m) is determined by the area sum of all cells for each water level, as shown in Formula 3.1:

$$A(h) = N(h)\, d_x d_y \qquad (3.1)$$

where N represents the number of pixels (-) and $d_x d_y$ represent the pixel surface area (m²). The functional relationship between the reservoir area and the corresponding water level can be expressed mathematically using Formula 3.2:

$$A = a(h - h_0)^c \qquad (3.2)$$

where A (m²) is the reservoir area, h (m) is the corresponding water level, h_0 (m) is the reference water level, and a (m) and c (m/m) are regression parameters obtained in the model through least squares fit. The reference water level h_0 (m) considered represents the deepest point in the reservoir and assumed to be equivalent to the elevation of the dam outlet. Consequently, the minimum value of D_t that is determined with Formula 3.1 is equivalent to h_0. The regression parameters can be obtained by implementing a non-linear regression on the available data, where a (m) represents the intercept of the fitted line, and c (m/m) represents the slope. Notably, the non-linear regression technique is preferred over linear regression on the logarithmic transformation of the data, as literature mentions it minimises the potential for systematic errors to be introduced (Xiao, White, Hooten, & Durham, 2011). The relation between the water level and the reservoir volume can be expressed using Formula 3.3:

$$V = \int_{h=h_0}^{h=h} a(h - h_0)^c dh$$

$$(3.3)$$

$$V = \frac{a}{b+1}(h - h_0)^{c+1} + C$$

where V (m³) is the reservoir volume, h (m) is the corresponding water level, h_0 (m) is the reference water level, and a (m) and c (m/m) are regression parameters. All the variables in these formulas are known, water level h (m), reference water level h_0 (m), and regression parameters a (m), b (-) and c (m/m). The parameter b, which is dependent on the characteristics of the surrounding terrain, has a notable influence on both the calculated hypsometric curve and the estimated volume of the reservoir. A value of $b = 1$ results in a linear elevation shift along the watercourse, whereas a smaller b value causes the reservoir bed to become flatter. Assuming a constant area A, a lower b value will lead to an increase in the h_0 parameter, which in turn causes the parameter set of (a, c) to increase. In conclusion, it should be noted that if assuming a constant area A, smaller values of b will result in a decrease in the calculated volumes (and vice versa). The integral of the hypsometric curve over the water level provides the relationship between the reservoir water level and volume. Upon completing this step, the relationship between volume and area is established for a range of water levels, allowing for the construction of the hypsometric curve.

3.1.5 Validation and Performance Evaluation of the Novel Method

Before validating the method, and testing the performance of the method, the modelled data is corrected for a systematic error related to the distinct datums in the datasets. The in-situ datum used in the validation data in many reservoirs differs from the reference elevation employed by the MERIT-Hydro DEM, which is, as previously discussed, referenced to the EGM96 geoid (Yamazaki et al., 2017). As a result, there may be a systematic offset between the observations of the model and the validation data, which could lead to poor model performance, even if the hypsometric curve suggests a strong relationship, indicated when the curve shows a similar shape. To address this issue, the systematic error (m) was calculated according to Formula 3.4:

$$\text{systematic error} = \frac{1}{n}\left(\sum_{i=1}^{n} h_{model_i} - \sum_{i=1}^{n} h_{validation_i}\right) \tag{3.4}$$

where, h_{model} (m) represents the modelled water level for the ith water level in the reservoir, $h_{validation}$ (m) represents the associated water level in the validation data and n (-) presents number of measurements. The systematic error is then subtracted from the water levels observed by the model. This correction for the distinct in-situ datums in the validation and modelled data will allow for fair analysis of the method.

3.1.5.1. Validation with a Group of Reservoirs

Then, accuracy of the hypsometric curves is determined as part of the qualitative analysis, which tests the performance of the method on a group of reservoirs. The coefficient of determination r^2 (-) is used to assess the overall performance of the reservoirs by comparing the absolute modeled values with the validation data at different filling rates (0%, 25%, 50%, 75%, and 100% of maximum capacity). To benchmark the r^2 values, literature values are used, which suggest values of 0.8 or higher, as seen in studies by Pistocchi & Pennington (2006), Hollister & Milstead (2010), and Heathcote, Giorgio, & Prairie (2015). Formula 3.5 was utilised to calculate the coefficient of determination:

$$r^2 = \left(\frac{n\left(\sum_{i=1}^{i=n} V_{model}V_{validation}\right) - \left(\sum_{i=1}^{i=n} V_{model}\right)\left(\sum_{i=1}^{i=n} V_{validation}\right)}{\sqrt{\left(n\sum_{i=1}^{i=n} V_{model}^2 - \left(\sum_{i=1}^{i=n} V_{model}\right)^2\right)\left(n\sum_{i=1}^{i=n} V_{validation}^2 - \left(\sum_{i=1}^{i=n} V_{validation}\right)^2\right)}}\right)^2 \tag{3.5}$$

where V_{model} represents the modelled volume and $V_{validation}$ (m³) the in-situ measured reservoir volume at each water level height, with n (-) representing the number of measurements. A coefficient of determination of 1 indicates a perfect fit, suggesting that the novel method is performing accurately for every reservoir in the reference dataset. However, a lower coefficient of determination suggests that the method may not be performing well for certain reservoirs in the dataset. When the coefficient of determination approaches 0, it may suggest that the novel method is unsuitable for estimating volumes in certain reservoirs of the reference dataset.

3.1.5.2. Validation of Individual Reservoirs

Finally, the relative error (-) is computed to evaluate the individual performance of the reservoirs with respect to their size, which adjusts for under or overprediction of reservoir volumes based on the reservoir size. This metric is expressed in Formula 3.6:

$$\text{relative error} = \frac{V_{validation} - V_{model}}{V_{model}} \tag{3.6}$$

where V_{model} (m³) represents the modelled volume, $V_{validation}$ (m³) the reference volume for specific water level heights (0%, 25%, 50%, 75%, and 100% relative to maximum capacity). A relative error ranging between 0 and 1 indicates an underestimation by the model, while a relative error of 1 indicates an accurate estimation of the reservoir volume. A relative error ranging between 1 and 2 implies an overestimation of the volume, while a relative error greater than 2 indicates an overestimation of twice the volume of the reservoir itself.

3.1.6 Transferability of the Novel Method

Ensuring the transferability of the method across different regions is crucial for its applicability to any reservoir worldwide within the Global Water Watch dataset. Some parameters discussed in Section 3.1.2 can be considered transferable as they are likely to be similar across multiple reservoirs, while others are untransferable and vary from reservoir to reservoir. These untransferable parameters are computed by the model and include the slope at the nearest upstream point, flattening parameter k, intercept, and slope parameters.

The method utilised in this thesis involves transferable input parameters such as the buffer around the initial delineated reservoir (Figure 3.2: *Step 1*), maximum Strahler order deviation from the Strahler order found in the main stream (Figure 3.2: *Step 4*), and downstream buffer considered for the downstream point (Figure 3.2: *Step 2*). These parameters are set similarly for reservoirs in the reference dataset. However, due to variations in reservoir size, shape, and surroundings, a single optimal parameter combination may not exist that applies universally to all reservoirs. Therefore, it is recommended to evaluate the performance of the parameter settings individually for each region.

The Strahler order deviation from the main stream plays a critical role in determining whether the entire reservoir is included in the computation. However, a larger deviation increases computation time significantly compared to smaller deviations. Additionally, the optimal downstream buffer considered for the downstream point may differ between smaller and larger reservoirs. It may be larger for larger reservoirs and smaller for smaller reservoirs. These variations in optimal parameter settings highlight that the optimal settings may vary between simple and complex-shaped reservoirs and may vary depending on the terrain and surrounding conditions.

The below Table 3.1 provides an overview of the untransferable input parameters used in the validation reservoirs, which can serve as a baseline for wider application of this method. The transferability of the parameters is further discussed in Section 3.4.

Transferable parameters	
Buffer around initial delineated reservoir (Figure 3.2: *Step* 1)	30 m
Downstream buffer from downstream point (Figure 3.2: *Step 4*)	500 m
Maximum Strahler order deviation from Strahler order found in main stream (Figure 3.2: *Step 5*)	5 (-)

Untransferable parameters	
Slope sampled at nearest upstream point (part of Formula 2.2)	Sampled from the DEM (m/m)
Flattening parameter k in main stream (part of Formula 2.2)	Obtained by linear regression (-)
Intercept a (part of Formula 3.1-3.3)	Obtained with least squares method (-)
Slope c (part of Formula 3.1-3.3)	Obtained with least squares method (-)

Table 3.1: The following tables provide an overview of the transferable and untransferable parameters utilised in the proposed method. The transferable parameters are given as input to the model, whereas the untransferable parameters are computed by the model itself. The transferable parameters listed in the table were applied in this thesis, but their optimal values may vary when applying the method to other regions and should therefore be thoroughly analysed and reconsidered.

3.2 Benchmark the Novel Method with Messager et al. (2016)

The objective of the consecutive research phase is to compare the performance of the novel method to literature. The novel method, described in Section 3.1, is benchmarked bathymetry reconstruction technique introduced by Messager et al. (2016), which was already introduced in Section 2.6 and is further elaborated on in Section 3.2.1. A schematic diagram of the conceptual framework for this benchmark experiment is presented in Figure 3.3.

To compare the effectiveness of the two methods, the volume time series produced by each approach were compared. The volume time series generated by the method described in Section 3.1 is compared with that generated using a bathymetry reconstruction approach proposed by Messager et al. (2016). This approach involves determining the topographic depth in each individual cell by extending the slope sampled in the nearest grid cell on the shoreline, using a 3x3 kernel towards the centre of the lake. The topographic depth in the cells is determined for each cell using Formula 2.2, which was previously presented. The effect of flattening of the lake bottom is taken into account by setting the flattening parameters k (-) to 0.95, 0.97, and 0.97. The resulting bathymetry is then used to derive the hypsometric curve.

To ensure consistency and comparability of the results, the derivation of the hypsometric curve using the bathymetry reconstruction approach in this study is performed with the same MERIT-Hydro DEM used in the novel method, as discussed in Section 3.1. Additionally, the DEM is accessed through HydroMT, a software developed by Eilander et al. (2023), in a similar manner, following comparable pre-processing steps such as region delineation and filtering of water surface cells with similar thresholds and methods as those described in Section 3.1.

As previously discussed in Section 2.6, the static approach proposed by Messager et al. (2016) is prone to sudden jumps in the bathymetry map of the reservoir. This is because the method relies on values sampled from the nearest cell on the shoreline to determine the topographic depth of a grid cell, which may differ for adjacent cells. Furthermore, the method's use of the generic parameter k to account for bottom flattening towards the centre of the lake is expected to result in an overestimation of volumes. These limitations may negatively impact the performance of the static approach by Messager et al. (2016) in comparison to the novel method.
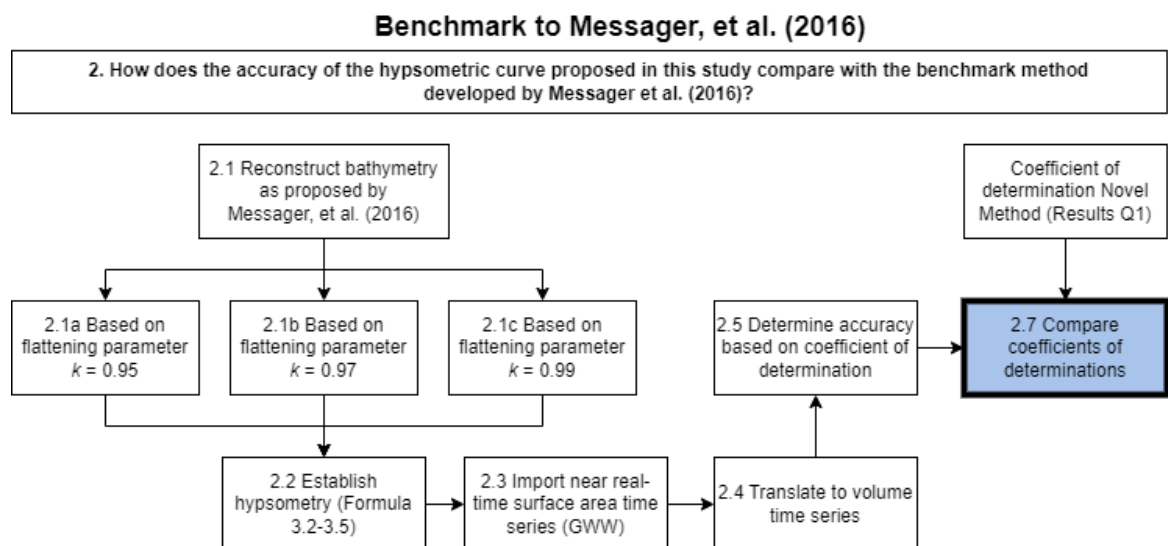
Figure 3.3: The figure illustrates the methodology employed to answer the second research question. First, the bathymetry is reconstructed using the method proposed by Messager et al. (2016) with varying flattening parameters k: 0.05 (2.1a), 0.97 (2.1b), and 0.99 (2.1c). Next, the resulting bathymetries are used to establish the reservoir hypsometric curve (2.2), which allows for the translation of the surface area time series (2.3) into volume time series (2.4). This newly established volume time series serves as the benchmark time series, and the coefficient of determination can be determined (2.5) and compared with the results of question 1 (2.7).

The hypsometric curve generated based on Messager et al. (2016) facilitates the conversion of the benchmark volume time series provided by Global Water Watch. Like the novel method, systematic errors are corrected in the benchmark time series, using Formula 3.4, before validation. Then, the coefficient of determination (r^2) for each reservoir is computed using Formula 3.5. This formula considers the modelled reservoir volume (V_{model}) at specific water level heights provided by the Messager et al. (2016) method, the validation volume ($V_{validation}$), and the number of measurements (n). An r^2 value of 1 indicates perfect performance for all reservoirs, while a lower value suggests suboptimal performance, and a coefficient of determination of 0 indicates unsuitability for volume estimations in the reservoirs in the validation dataset. By comparing the coefficient of determination between the novel method and the Messager et al. method, their performances could be compared.

3.3 Exploring the Predictive Performance for Water Availability

The last research phase is dedicated to predicting decreased water availability in reservoirs, with the help of the volume time series generated by the novel method in Section 3.1. For this purpose, the volume dynamics in the Hawane reservoir in Eswatini is examined. This reservoir is introduced and contextualised in the following Section 3.4, along with an overview of all other reservoirs examined throughout this thesis. This subsection will cover the data-driven models used for predicting water availability, the variables used for prediction, and the method applied to assess their predictive skill. Figure 3.4 provides a visual representation of this approach.

3.3.1 Predicting Water Availability with Regression Models

This subsection evaluates the skill of several regression models in predicting the decreased water availability in reservoirs during drought events. The volume time series used in this analysis is obtained with the method introduced in Section 3.1, which means that the models are not tested on in-situ measured volumes but rather on volumes derived from bathymetry estimations. The regression models are trained using a distinct subset of the entire time series, and their aim was to identify the gain in predictive performance compared to the seasonality.
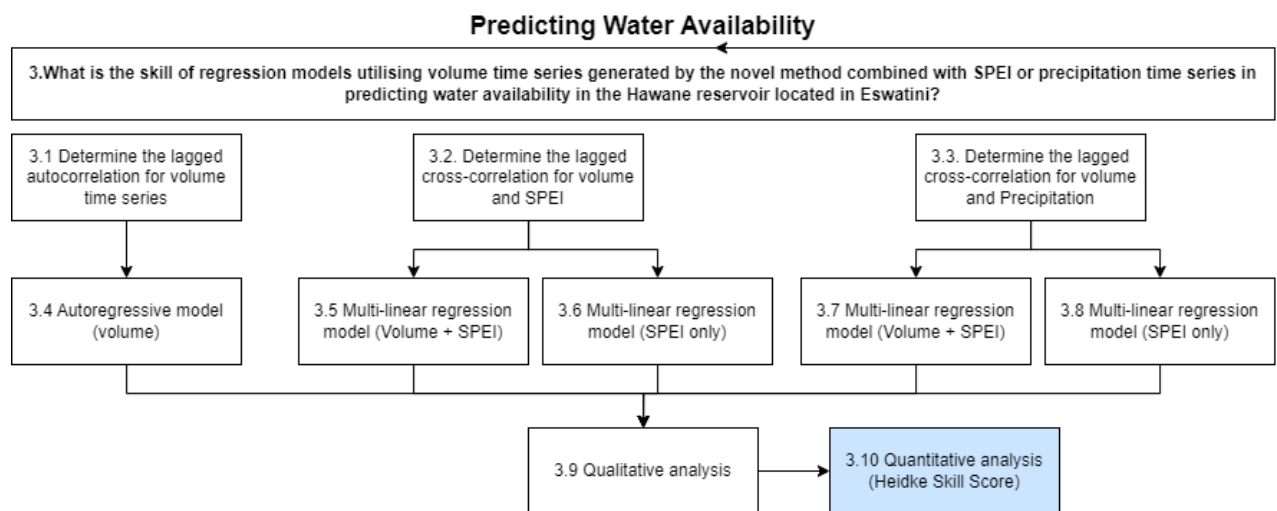
Figure 3.4: A conceptual representation of the approach to answer the third research question. The methodology involves retrieving the hypsometric curve of the Hawane Dam using the novel method outlined in Section 3.1 of this thesis. Subsequently, a narrative is created from a severe drought event that occurred in 2016 using three different versions of the regression model. The first model relies solely on volume time series (autoregression) (3.1), while the second version introduces the Standardised Precipitation and Evapotranspiration Index (SPEI) time series as a variable (multi-linear regression) (3.2). The third version explores the predictive skill of the precipitaiton (3.3). To determine the appropriate lag-time of each variable taken into account, the methodology entails employing lag-time analysis for each version of the model. Additionally, a autoregressive model (3.4) or a multi-linear regression model is created (3.5-3.8). The results of the models are analysed first in a qualitative analysis and then by the Heidke Skill Score in a quantitative analysis (3.9 & 3.10).

The predictor variables considered in the models are the volumes itself, the ERA5 precipitation in the catchment upstream of the reservoir by Hersbach et al. (2020), and the monthly Standardised Precipitation and Evaporation Index (SPEI) by Beguería et al. (2021). The motivation behind the selection of each predictor variable and the way they are used in the regression models will be presented in Section 3.3.2. Each model forecasts up to 6 months into the future using these predictors, resulting in a total of 72 predictions per year (starting at every month, for every consecutive month up to six months after).

As discussed in Section 2.9.3, the number of values included in the regression model varies depending on the lagged correlation with the dependent variable in the respective month, which is the current month (0) in this case. To calculate the correlation coefficient (r) for each lag, Formula 3.7 is applied:

$$r = \frac{\sum\left(\left(x_i - \frac{1}{n}\sum_{i=1}^{n} x_i\right)\left(y_i + \frac{1}{n}\sum_{i=1}^{n} y_i\right)\right)}{\sqrt{\sum\left(x_i - \frac{1}{n}\sum_{i=1}^{n} x_i\right)^2 \sum\left(y_i + \frac{1}{n}\sum_{i=1}^{n} y_i\right)^2}} \qquad (3.7)$$

where x represents the value of the dependent variable, y the value of the lagged variable, and n the total number of lagged variables. The correlation coefficient ranges from -1 to 1, with values closer to these extremes indicating a stronger correlation and values closer to 0 indicating a weaker correlation. It is expected that 95% of the values in the autocorrelation lay within two standard deviations from the mean, representing the white noise. The 95% bound is derived with Formula 3.8:

$$\text{bounds}_{95\%} = \frac{\pm 1.96}{\sqrt{n}} \qquad (3.8)$$

where n represents the length of the time series. If there are values that are outside these bounds, or if the entire series is outside these bounds, the series is likely to contain a signal, and is most probably not white noise only. The values inside these bounds are likely to show a correlation that does not differ from 0.

The outputs of the regression models are subjected to both qualitative and quantitative analyses. In the qualitative analysis, a series of predictions are examined starting at three distinct moments: the middle of the rainy season, the end of the rainy season, and the middle of the dry season. For each moment in time, predictions up to six months ahead are examined, and their behavior in correctly predicting the volume time series will be described. In the quantitative analysis, the models are evaluated based on their skill to predict whether the volume will fall below the threshold of one standard deviation from the seasonal trend, expressed with the Heidke Skill Score, which was discussed in Section 2.10 in Formula 2.8. The score is derived for every month of the year for each lead time in the forecast, and it indicates the proportion of correctly forecasted observed values relative to what would be expected by chance. A perfect forecast is indicated by a value of 1, while a score of 0 indicates no skill. A negative score suggests that the forecast performs worse than a forecast by chance.

3.3.2 Predictors and Models Under Consideration

This study aims to evaluate the predictive performance of regression models utilising the volume time series generated with the novel method, which was discussed in Section 3.1. To achieve this, three predictor variables are selected: volume, precipitation, and the Standardised Evapotranspiration and Precipitation Index (SPEI). The memory of the volume time series is tested using an autoregressive model, while the added predictive skill with precipitation and SPEI are examined through a multi-linear regression model. All predictors are evaluated as individual predictors as well as in combination with volume as a predictor. In the following subsections, each single predictor will be discussed in detail.

3.3.2.1. Autoregression with Volume Time Series

The autoregressive analysis is performed on the volume time series obtained from the novel method discussed in Section 3.1. The volume of a reservoir is not only determined by the inflow, outflow, and storage capacity, but also by its residence time, which refers to the duration of water storage in the reservoir before it is released. This residence time causes a lagged response of the reservoir to

external factors. For example, in case of the absence of inflow, the reservoir will take a period equal to its residence time to become completely depleted. Thus, the memory effect of the reservoir is expected to be a crucial factor in predicting its future state. In line with Section 2.9, the autoregressive model takes advantage of this memory effect in the dependent variable, which in this case is the volume time series. The autoregressive model employed in this study is based on the one described in Section 2.9 and can be mathematically represented by Formula 3.11:

$$V_m = C + \beta_1 V_{m-1} + \beta_2 V_{m-2} + \cdots + \beta_i V_{m-i} + \varepsilon_m \qquad (3.11)$$

where V is the dependent variable, C as the reference datum, i as the number of preceding months in the autoregressive model, $V_{m-1}, V_{m-2}, \dots V_{m-i}$ as the monthly volumes associated with the preceding months, and $\beta_1, \beta_2, \dots \beta_i$ (-) as the corresponding weights. The determination of the number of values used as input is described in Section 3.3.1 and is based on the lagged autocorrelation. Last, ε_m is the uncertainty or "white noise" associated with the prediction for the respective month m.

3.3.2.2. Multi-Linear Regression with Precipitation Time Series

The added predictive skill by the introduction of precipitation as a predictor is explored in multi-linear regression models. As previously discussed in Section 2.2, reservoir storages are supplemented by the runoff resulting from precipitation in the catchment upstream. Thus, the amount of precipitation resulting in runoff into the reservoir is expected to be an important factor in predicting its future state. As mentioned in Section 2.9, the multi-linear regression model takes advantage of the information in time series of an explanatory variable, which in this case is the precipitation time series.

The aim of this analysis is to determine whether incorporating precipitation time series, obtained from the ERA5 dataset by Hersbach et al. (2020), into the previously presented model in Section 3.3.2.1 would enhance its predictive power, given that precipitation contributes to reservoir storages through runoff from the upstream catchment. It is anticipated that the addition of precipitation time series to the model will improve its predictive ability, particularly during the wet seasons when more precipitation is expected, while during the dry seasons, minimal to no precipitation is expected, and the effect on the model may be limited. The approach starts with analysing the predictive performance of precipitation as the sole predictor using a multi-linear regression model described in Formula 3.12:

$$V_m = C + \omega_1 P_{m-1} + \omega_2 P_{m-2} + \cdots + \omega_i P_{m-i} + \varepsilon_m \qquad (3.12)$$

where V (m³) is the dependent variable at the respective month m, while the explanatory variable is the precipitation P (mm) for the preceding months. The determination of the number of values used as input is described in Section 3.3.1 and is based on the lagged correlation between volume and precipitation. $\omega_1, \omega_2, \dots \omega_i$ (-) represent the weights associated with the precipitation values of the preceding months, C is the reference datum and ε_m is the "white noise" or uncertainty in the prediction at the same respective month m.

Next, the predictive performance of a combination of precipitation and volume time series is explored. The multi-linear regression model aims to find the volume V (m3) at the respective month m by combining volume (as both dependent and explanatory variable, like in autoregression) and precipitation (as explanatory variable). Specifically, this is described in Formula 3.13:

$$V_m = C + \beta_1 V_{m-1} + \omega_1 P_{m-1} + \beta_2 V_{m-2} + \omega_2 P_{m-2} + \cdots + \beta_i V_{m-i} + \omega_j P_{m-j} + \varepsilon_m \qquad (3.13)$$

where V_{m-i} represents volume in the ith month preceding the respective month. For each volume value the associated weights are presented by $\beta_1, \beta_2, \dots \beta_i$ (-). P represents precipitation in the jth preceding month, with associated weights $\omega_1, \omega_2, \dots \omega_i$. Again, the number of values used as input is based on the lagged correlation between volume and precipitation. C is the reference datum, and ε_m is the "white noise" or uncertainty in the prediction at the respective month m.

3.3.2.3.   Multi-Linear Regression with Monthly SPEI Time Series

Last, the added predictive skill of the monthly SPEI by Beguería et al. (2021) is explored in a multi-linear regression model. As noted in Section 2.2, both precipitation and evapotranspiration have direct and indirect impacts on reservoir conditions, which are captured by the SPEI, representing the standardised discrepancy between precipitation and potential evapotranspiration. This index provides an indication of drought conditions relative to normal conditions. The SPEI serves as an indicator of drought conditions relative to normal conditions in a 1x1 degree latitude-longitude spatial resolution. In addition to providing insight into precipitation and evaporation levels, it also reflects the demand for water in the surrounding environment, which is likely to increase during times of drought. As a result, the SPEI is anticipated to be a crucial factor in forecasting the future state of a reservoir. The multi-linear regression model takes advantage of the information in the SPEI time series, as explanatory variable.

First, the predictive performance of the SPEI as the sole predictor is explored in a multiple linear regression model, which is expressed in Formula 3.14:

$$V_m = C + \varphi_1 S_{m-1} + \varphi_2 S_{m-2} + \cdots + \varphi_i S_{m-i} + \varepsilon_m \qquad (3.14)$$

where V (m³) represents the dependent variable for the corresponding month m, while the explainable variable is the SPEI S (-) for the previous months. Again, the number of values used as input is based on the lagged correlation between volume and SPEI. The weights assigned to the SPEI values of the previous months are represented by $\varphi_1, \varphi_2, \dots \varphi_j$ (-) with C serving as the reference datum and ε_m representing the "white noise" or uncertainty in the SPEI for the same corresponding month m. Last, the SPEI is integrated with the available volumetric time series, as detailed in Formula 3.15:

$$V_m = C + \beta_1 V_{m-1} + \varphi_1 S_{m-1} + \beta_2 V_{m-2} + \varphi_2 S_{m-2} + \cdots + \beta_i V_{m-i} + \varphi_j S_{m-j} + \varepsilon_m \qquad (3.15)$$

where V_{m-i} refers to the volume in the ith month before the respective month. The associated weights for each volume value are presented as $\beta_1, \beta_2, \dots \beta_i$ (-). Additionally, the SPEI S in the same ith preceding months and is represented by ∂ (-), with associated weights $\varphi_1, \varphi_2, \dots \varphi_i$ (-). Again, the number of values used as input is based on the lagged correlation between volume and SPEI. C denotes the reference datum, and ε_m signifies the "white noise" or uncertainty in the prediction for the respective month m.

3.3.2.4.   Additional Analysis with SPEI Time Series

Previous studies have demonstrated successful analysis of water availability or deficits using climate indices similar to SPEI in regression models (Dibike et al., 2016; Ghasemi et al., 2021; Jiao et al., 2021; Gurrapu et al., 2021; Li et al., 2023). However, in some reservoirs, it is possible that there is no significant lagged correlation between the SPEI and the volume time series. The hypothesis is that reservoirs with longer residence times may not exhibit enough variation in volume dynamics to have a lagged correlation with SPEI. In such cases, it is decided to use three SPEI values in the multi-linear regression model for the subject reservoir, even if no lagged correlation is found. Furthermore, an examination is carried out on a different reservoir, which exhibited volume dynamics that closely corresponded with the seasonality and, therefore, presented more fluctuations. The hypothesis is that due to this variability, there would be a higher lagged correlation between the SPEI and the volume of water in the reservoir.

3.4 Description of Case Studies and Reference Data

In this thesis, reservoirs from Zambia, India, Eswatini, and Lesotho are studied to address the research questions. This section provides an introduction to the reservoirs and their datasets and explains why they were selected. The Zambian reservoirs are discussed in Section 3.4.1 and the Indian dataset is introduced in Section 3.4.2. The reservoir in Eswatini is extensively emphasised in Section 3.4.3 becasue it is part of the third research question of this thesis. Last the Lesotho reservoir is introduced in Section 3.4.4. To provide a clear overview of all the reservoirs and their details, Table 3.1 highlights the information for each reservoir and the experiments in which they are utilised in this thesis.

3.4.1 Zambian Reservoirs examined for Validation Novel Method

Two reservoirs in Zambia, Mita Hills and Mulungushi, are primarily examined to validate the novel method described in Section 3.1. Figure 3.5 presents an overview on the Mita Hills Dam in Zambia and Figure 3.6 on the Mulungushi Dam:
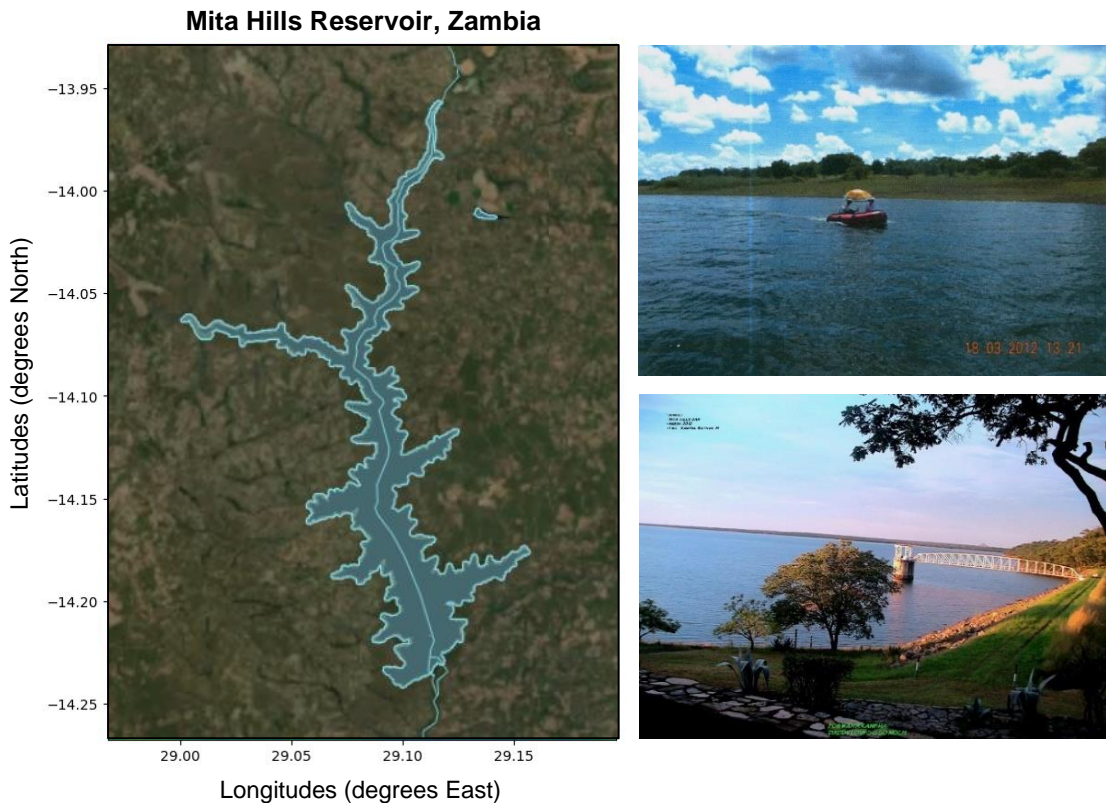

Figure 3.5: A map by Global Water Watch and photos that provide an impression of the Mita Hills reservoir in Zambia. The reservoir has a dendritic shape with several tributaries, as can be seen from the Global Water Watch image on the left (Donchyts, 2022). On the right-hand side, photos are displayed to provide an impression of the vegetation and the relatively flat area surrounding the reservoir. Source: Left: Map by Global Water Watch (2023). Upper right: Photo by Studio Pietrangeli (2012a). Lower right: Photo by Blog (2013).
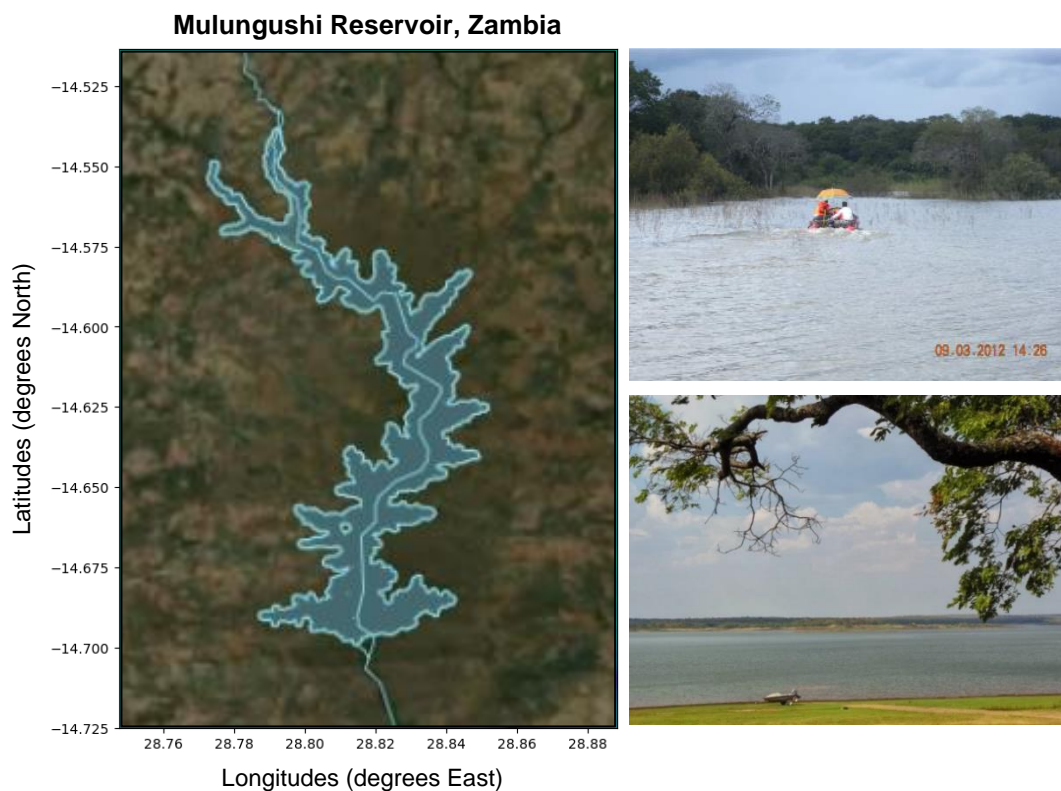
Figure 3.6: Also for the Mulungushi Dam in Zambia a map and photos are shown. Like Mita Hills, the shape is dendritic with smaller tributary areas. On the right, several photos provide a glimpse of the reservoir's surroundings, which are relatively flat and covered in vegetation similar to that of the Mulungushi Dam. Source: Left: Map by Global Water Watch (2023). Upper right: Photo by Studio Pietrangeli (2012b). Lower right: Photo by Muwowo (2012).

Both reservoirs are situated near Kabwe, the capital of Zambia, and are primarily utilised for hydropower generation. As the figures show, they share similar terrains in terms of vegetation and elevation. Both have a dendritic shape and contain several smaller tributaries. The Mulungushi reservoir was established in 1925 and is approximately 20 kilometres in length and 2-3 kilometres in width. The larger Mita Hills Reservoir was constructed in 1955, spans 30 kilometres in length and 3-5 kilometres in width.

The main motivation for the examination of these reservoirs is because of the high-quality bathymetric reference data for the reservoirs was made available by the Zambian Water Resource Management Authority (WARMA) (Studio Pietrangeli, 2012a; 2012b). The data from the bathymetric report was created during a survey with a single-beam sonar system and included relationships between volume and area for a range of water level heights. This high-quality data enabled the validation of a sub-step in the method for generating volume time series.

To optimise the transferable parameters of the novel method for the Zambian reservoirs, the method applied a parameter set with a Strahler order deviation from the main stream to 5, the delineation buffer in HydroMT was set to 30 meters and a buffer of 500 meters downstream of the lowest sampled point was used.

3.4.2 Indian Reservoirs examined for Further Validation

A total of 94 Indian reservoirs are analysed, and their locations are depicted in Figure 3.7:

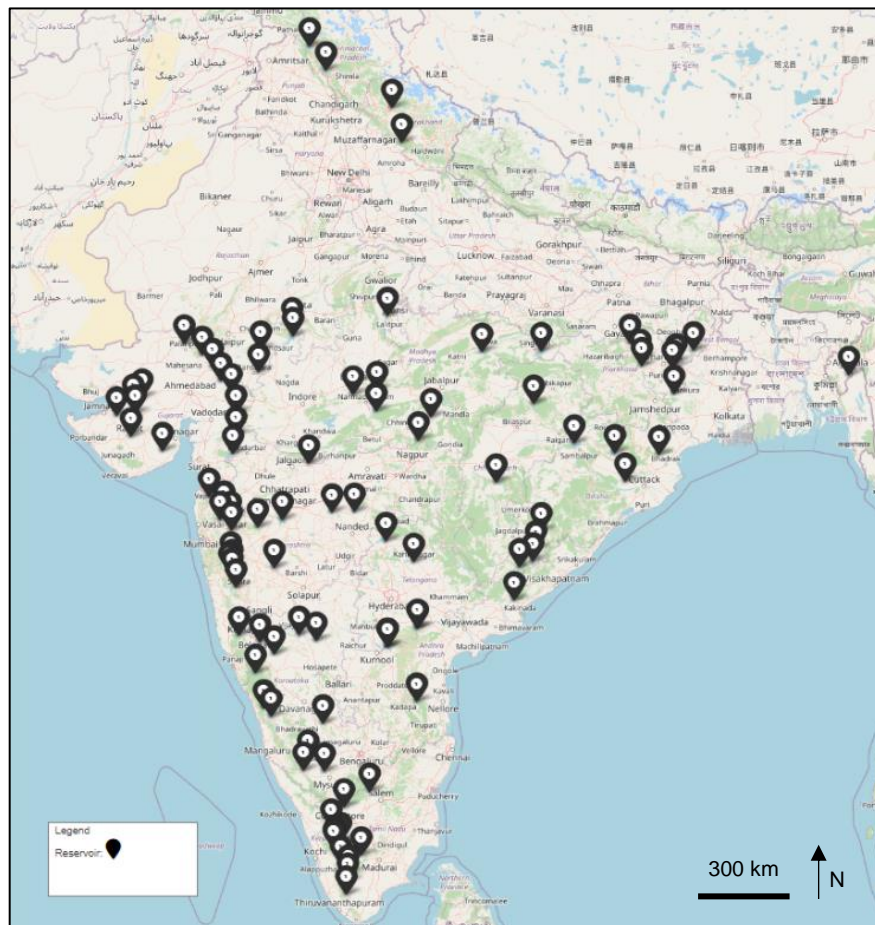**The Map of India showing the Locations of 94 Reservoirs**

Figure 3.7: The map of India indicating the location of each reservoir in the Indian reference dataset. The reservoirs are dispersed throughout the entire country, with a greater concentration in the west. The wide range of variation in the dataset presents an opportunity to test the effectiveness of the novel method.

As illustrated in the figure, these reservoirs are dispersed throughout the entire country and exhibit diverse characteristics such as varying sizes, shapes, elevations, and surrounding terrains. The decision to utilise the Indian dataset was primarily driven by the accessibility of data provided by the Indian Central Water Commission. The dataset includes volume time series for each reservoir in respect to an unknown in-situ datum and ranges from 2002 to 2018. The dataset's wide range of reservoir types made it particularly suitable for testing the proposed method. The method employed the same parameter settings used for the Zambian reservoirs to retrieve bathymetry.

3.4.3 Eswatini Reservoir for Water Availability Predictions

The predictive performance of regression models is applied to the Hawane reservoir in Eswatini due to societal importance of the Hawane reservoir. The data used in the prediction ranges from 2000 to 2021 and is obtained through Global Water Watch and translated into volumes with the novel method. The Kingdom of Eswatini, previously known as Swaziland and hereafter referred to as 'Eswatini', is a Southern African country with a population of approximately 1,2 million people. Eswatini shares borders with South Africa and Mozambique and has a land area of 17.360 km2, making it the smallest country in the Southern Hemisphere. The country has a subtropical climate characterised by wet summers from November to April, with average temperatures ranging between 15 and 27 degrees Celsius. The winters are generally dry, lasting from April to September, with average temperatures ranging from 14,6 to 25 degrees Celsius. Eswatini receives an average annual precipitation of around 800 mm, of which approximately 75% falls during the summer, as illustrated in Figure 3.8 and spatially presented in Figure 3.9 (World Bank Group, 2021).
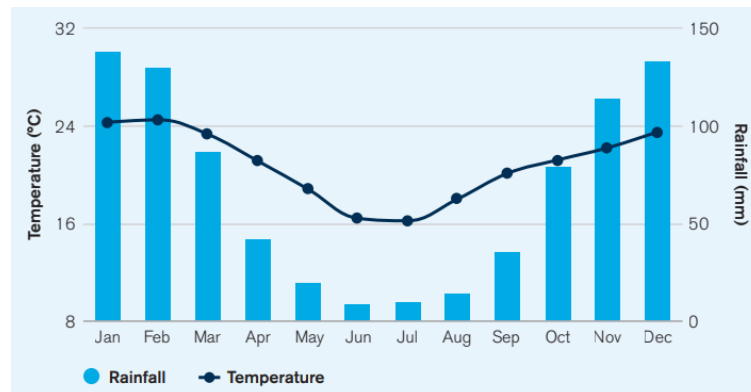

Figure 3.8: The average monthly temperature and rainfall for Eswatini, calculated over the period 1991-2020. Eswatini has a subtropical climate with wet summers that start in October and end in April. The figure illustrates that the annual temperature ranges from 15 to 27 degrees Celsius, while 75% of the annual rainfall occurs during the summer period from November to April, as noted in the World Bank Group report (2021).
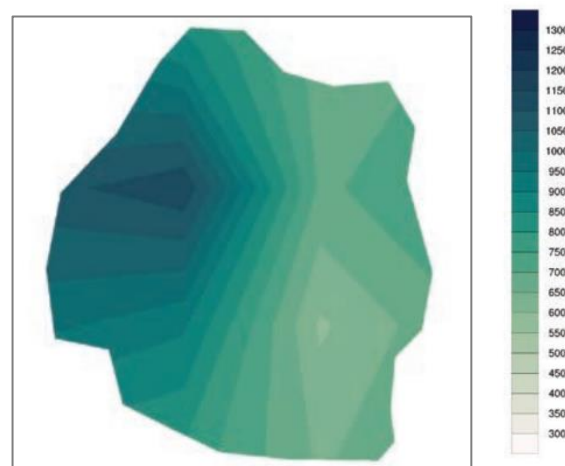

Figure 3.9: The spatial variability of the annual precipitation (mm) in Eswatini processed with interpolation between weather stations, causing the gradual pattern. The graph demonstrates that the majority of precipitation occurs in the western region of the country where the Highveld is situated. The Highveld is characterised by montane grasslands and aquatic systems, and the city of Mbabane is located within this region, as indicated in the World Bank Group report (2021).

Agriculture is the most significant economic activity in the country, with 77% relying on resources provided by livestock. Eswatini has faced various natural hazards over the past century, including tropical storms, epidemic diseases, forest fires, severe floods, and multi-year droughts. These events have had significant impacts on the country's population, with 25% of its population experiencing food and water insecurity. Climate change is considered a significant threat to the growing needs of Eswatini's vulnerable communities (World Bank Group, 2021).

3.4.3.1. The Severe Drought 2015-2016: Impacts on the Hawane Reservoir

In 2016, Eswatini experienced a severe drought induced by El Nino, which led to a decrease of over 50% in rainfall during the 2015-2016 season. The country suffered extensive damage, with fresh water reserves declining by more than half, and resources like the Hawane Dam and Mnjoli Dam almost completely drying up (Deputy Prime Minister's Office, 2016). The ESG News Eswatini (2016) reported that the government declared a state of emergency from February of that year and called for severe curtailments, which included cutting off the domestic water grid for four days a week until the arrival of the summer rains. The agricultural sector was severely impacted, with significant economic losses reported, particularly in sugarcane and vegetable production, where revenue losses of 30% and 80%, respectively, were observed as well as reduced crop qualities. The yields were also affected, with maize production reduced by 63% compared to the previous five years. By March, over 63.000 cattle had died, leading to many farmers losing their businesses (Magagula, 2016). This resulted in higher food prices and poor crops, which put 550.744 livelihoods (approximately 50% of the population) at risk.

The Hawane Dam serves as the primary source of water for Mbabane, the capital city of Eswatini, which has a population of 60.691 individuals (Tracks4Africa, 2013; AZ Nations, 2017). Located in the Hawane Dam and Nature Reserve, a protected area of approximately 232 hectares, the dam is situated along the Mbuluzi River northeast of Mbabane, as illustrated in Figure 3.9. Established in 1978, the nature reserve was created to preserve the marshes along the Mbuluzi River, which play a significant role in supporting the region's biodiversity. During the 2016 drought, water levels in the Hawane Dam fell to 9% of full capacity by August, as reported by ESG News (2016). Images capturing the nearly dried-up Hawane Dam are presented in Figure 3.10.

Hawane Dam, Eswatini
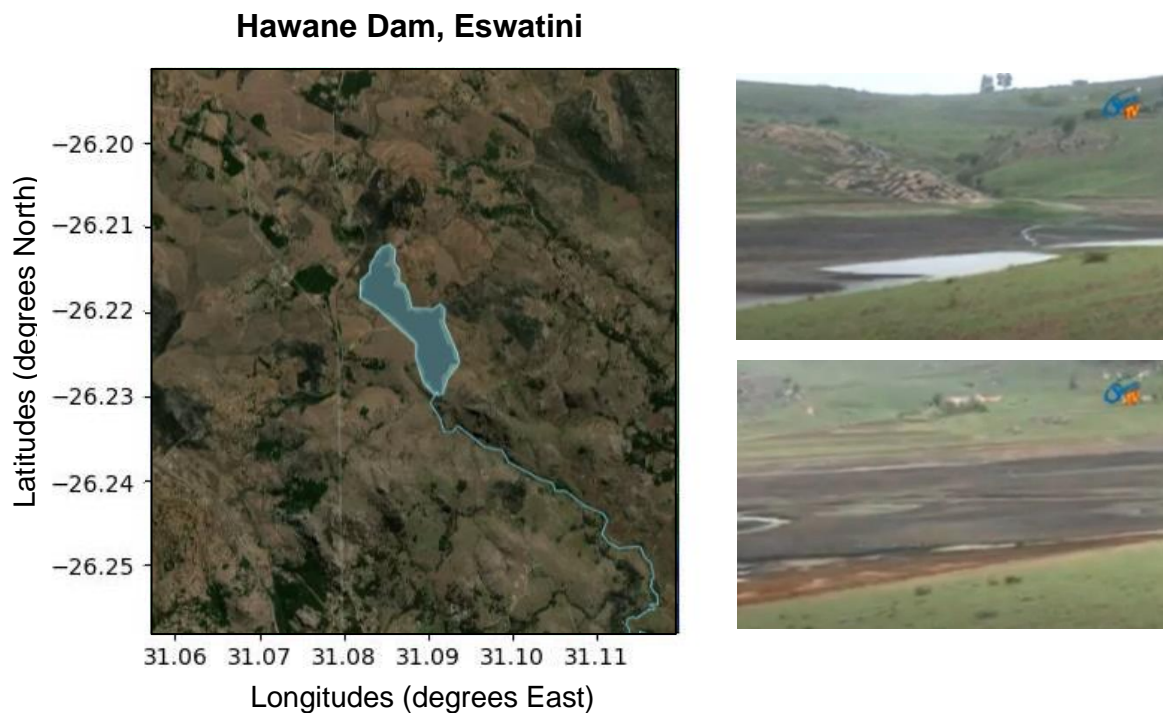
Figure 3.10: A map retrieved from Global Water Watch by Donchyts et al. (2022) showing the shape of the Hawane reservoir and its surroundings (left). Furthermore stills from a public TV broadcast by ESG News (2016) are presented (right). The broadcast was aired on November 8, 2016, after rainfall had started filling the Hawane Dam reservoir again. The provided stills depict the completely dried areas in the Hawane Dam earlier that year, which were used in the broadcast to compare the current situation (ESG News Eswatini, 2016).

3.4.4 Lesotho Reservoir examined for Seasonality in Volume Time Series

To investigate the effect of seasonality on the predictive performance of the regression model using the SPEI and volume, an additional study is conducted on the Katse Dam in Lesotho, which is presented in Figure 3.11:
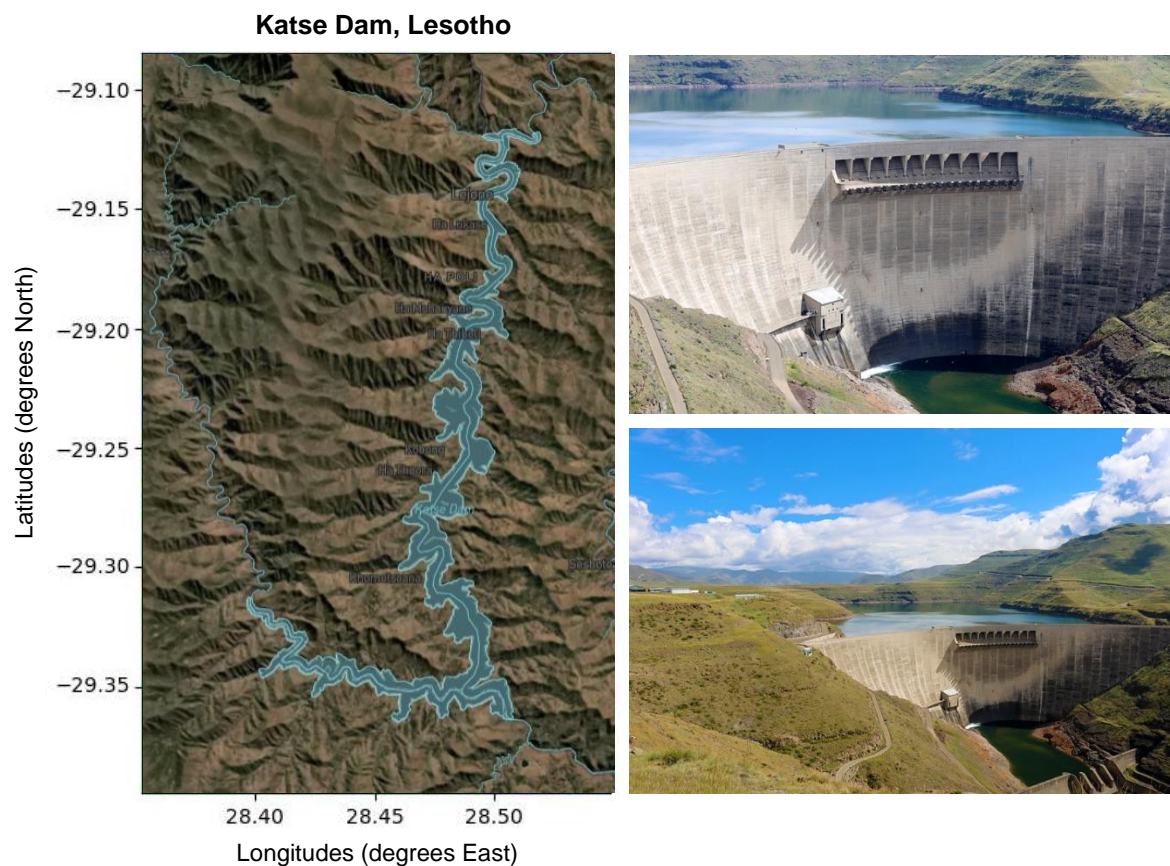

Figure 3.11: A map retrieved by Global Water Watch (Donchyts, 2022) and photos of the Katse Dam in Lesotho. It is evident from the images that the dam has a complex shape, where two longitudinal shapes converge at the dam. The satellite imagery on the left displays the shape of the Katse Dam, while the image on the right provides a view at the dam itself, as well as the surrounding elevations and vegetation. These photos were captured by Brian Cohen (2015).

Similar to the Hawane Dam, the analysis of the Katse Dam does not rely on reference data. The method used for bathymetry retrieval for the Katse Dam study is the same as the one used for the Zambian reservoirs. The selection of the Katse Dam for the additional study is based on its response to seasonality in its volume dynamics, which contrasts with the Eswatini reservoir that maintains a more constant dynamics except during drought events. The study's goal is to compare the predictive performance of the regression model using the SPEI and volume for the Katse Dam and the Hawane Dam.

3.4.5 Overview of Case Studies

Table 3.3 provides a summary of Section 3.4 as a whole:

Case study	Number of reservoirs	Description of reservoirs	Validation data	Experiments
Zambia	2 (Mita Hills and Mulungushi Dam)	Size ~ 5500 ha. (Mita Hills) and ~3000 ha. (Mulungushi) Man-made reservoirs Dendritic shape incl. smaller tributaries Constructed in 1955 (Mita Hills) and 1925 (Mulungushi)	Bathymetric Survey providing the hypsometric curve provided by WARMA (2012).	Applied in initial validation process for the novel approach in calculating bathymetry due to complete bathymetry validation data (Section 4.1).
India	94	Various sizes All man-made reservoirs. Mix of complex, cascading and 'standard' dendritic shapes Constructed over various years	Volume Time Series (2002-2018) provided by Indian CWC	Applied in testing of novel method for a wide range of reservoirs (Section 4.2)
Eswatini	1 (Hawane Dam)	Size ~232 ha. Man-made reservoir Dendritic shape Constructed in 1988	N.A.	Test the predictive performance of water volumes (qualitative and quantitative) using autoregression, precipitation and SPEI (Section 4.3 & 4.4). Chosen because relevant to society and recent impactful drought event in the reservoir.
Lesotho	1 (Katse Dam)	Size ~3.580 ha. / 1950 km^3 (max. capacity) Complex, two merging dendritic shapes Man-made reservoir Constructed in 1996	N.A.	Test the predictive performance of water volumes (qualitative and quantitative) using autoregression, precipitation and SPEI (Section 4.5). Chosen to validate against reservoir with high seasonality in volume time series.

Table 3.3: An overview of the reservoirs examined in the case studies, including the number of reservoirs, reservoir description, validation datum details (if applicable), and experiments done with the reservoirs. Abbreviations in the table: WARMA is the Zambian Water Resource Management Authority, CWC is the Central Water Committee in India and the SPEI is the Standardised Precipitation and Evapotranspiration Index.

The study examines several reservoirs in different countries to test the proposed method for calculating bathymetry and predicting water volumes. Two reservoirs in Zambia, Mita Hills and Mulungushi Dam, are used to develop and test the novel method because their reference data provided excellent reference data. The study also included 94 man-made reservoirs in India with varying sizes, shapes, and surrounding terrains, ideal for testing the novel method for a large number of reservoirs. In Eswatini, the study focuses on Hawane Dam, which experienced a severe drought event in 2016. This case study therefore allows to test whether predictive performance can be gained using volume, precipitation, and SPEI as predictors. Lastly, the study uses Katse Dam in Lesotho to validate against a reservoir with high seasonality in volume time series.

4

Results

The results chapter provides the in-depth analysis of the performance of the novel method for retrieving reservoir bathymetry and predicting water availability. Section 4.1 presents the results of the step-by-step retrieval process and the construction of associated hypsometric curves. In Section 4.2, the novel method is applied to 94 reservoirs in India, and the results are analysed. Section 4.3 compares the novel method with a benchmark method proposed by Messager et al. (2016). The results of the regression models in reservoirs in Eswatini are presented in Section 4.4. Finally, Section 4.5 provides additional analysis of the Standardised Precipitation and Evapotranspiration Index (SPEI) in the Lesotho reservoir. Overall, this chapter provides a comprehensive evaluation of the effectiveness and accuracy of the novel method and its potential for improving water resource management in various regions.

4.1   Step-By-Step Bathymetry and Hypsometry Construction

In this section, the step-by-step results of the retrieval process is presented for the bathymetry and hypsometry of two reservoirs located in Zambia, namely 'Mulungushi' and 'Mita Hills'. These are the results of the bathymetry method after multiple iterations and optimisation of the algorithm. The conceptual approach utilised in this process is visually presented in Figure 3.2. The hypsometric curve is shown in Figure 8.

4.1.1 Delineation of the Reservoir

The delineation process is carried out using the model generation tool HydroMT, software by Eilander et al. (2023), and reference coordinates accessed from the Global Water Watch platform (Donchyts et al., 2022). Mita Hills and Mulungushi reservoirs are identified using their respective reference IDs 88643 and 87292. Results of the delineation process, which is described in Step 1 and illustrated in Figure 3.2, are presented in Figure 4.3 for Mita Hills and Figure 4.4 for Mulungushi.

Mita Hills Reservoir, Zambia

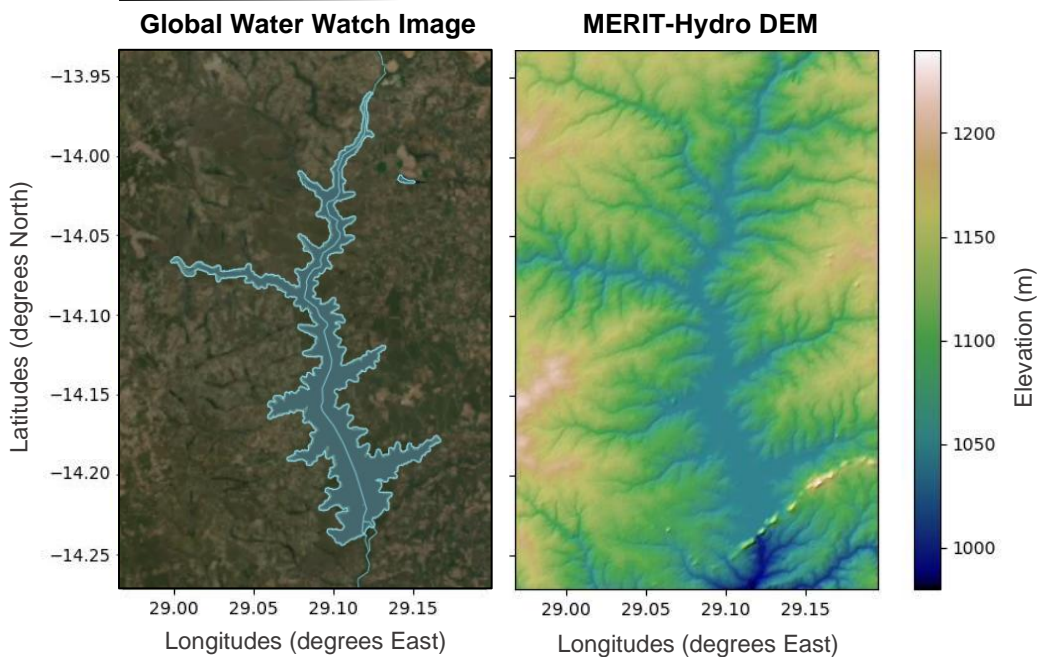**Global Water Watch Image**   **MERIT-Hydro DEM**

Figure 4.1: The satellite image including the reservoir shape obtained through Global Water Watch by Donchyts et al. (2022) (left) and MERIT-Hydro DEM by Yamazaki et al. (2017) (right) of the Mita Hills reservoir in Zambia. The surface water level of the reservoir at the time of measurement was approximately 1050 meters. The geospatial coordinate system in terms of latitude and longitude in degrees is presented on the y- and x-axis, while the z-axis represents the elevation in meters as indicated by the colorbar ranging from 900 to 1400 meters.

Mulungushi Reservoir, Zambia

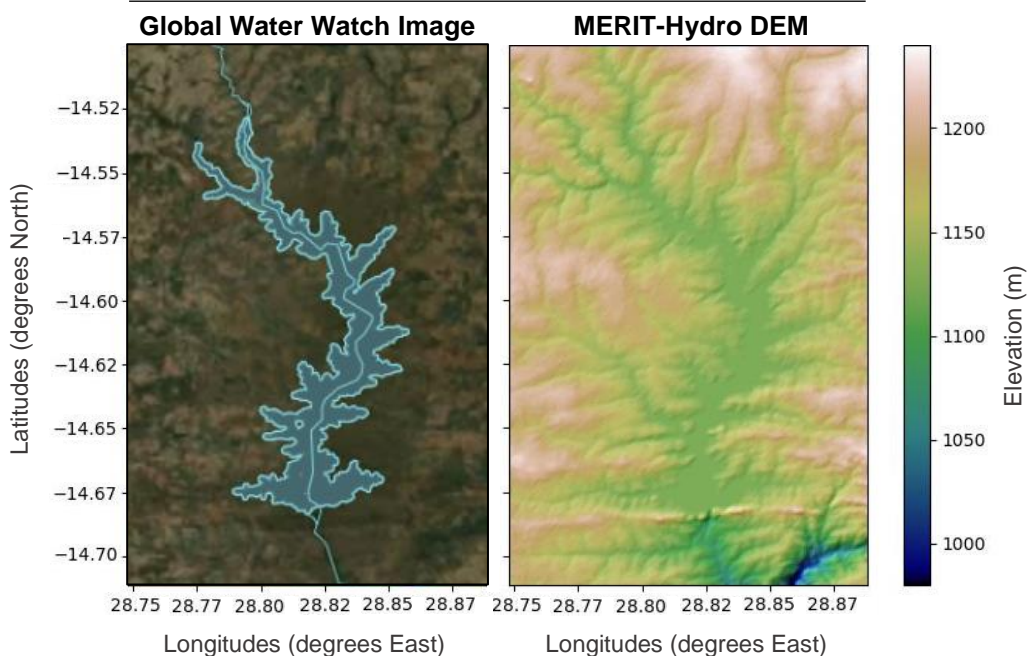**Global Water Watch Image**   **MERIT-Hydro DEM**

Figure 4.2: The elevation map of the Mulungushi reservoir in Zambia retrieved from Global Water Watch by Donchyts et al. (2022) (left) and the Hydro-MERIT DEM Yamazaki et al. (2017) (right). The reservoir's surface water level at the time of measurement recorded is around 1115 meters. Like Figure 4.3, the y-axis and x-axis represent the geospatial coordinate system in latitude and longitude, while the z-axis is represented in colors following the colorbar of elevation, ranging from 900 to 1400 meters.

The reservoirs have a typical man-made reservoir shape, characterised by a dendritic shape as discussed in Section 2.1. In addition, both reservoirs exhibit clear tributaries on each side of the reservoir, which is a common feature of man-made reservoirs where water follows the surrounding landscape elevations. Both reservoirs have similar terrain surroundings in terms of vegetation and elevation, as stated in the introduction of this section. However, the Mita Hills reservoir is situated approximately 65 meters below the Mulungushi reservoir, as shown in the Figures. Furthermore, both maps exhibit a sudden jump in elevation (for Mita Hills area at -13.97° latitude and 29.13° longitude, and for Mulungushi at -14.54° latitude and 28.825° longitude), which is assumed to correspond to the location of the dam wall.

4.1.2 Filtering the Reservoir Surface

The algorithm designed for the retrieval of reservoir bathymetry begins by filtering the surface water level from the reservoir, as is illustrated by Figure 3.2 and described by Step 2. This process is successfully executed for both Mita Hills (left), as shown in Figure 4.3, and Mulungushi (right).
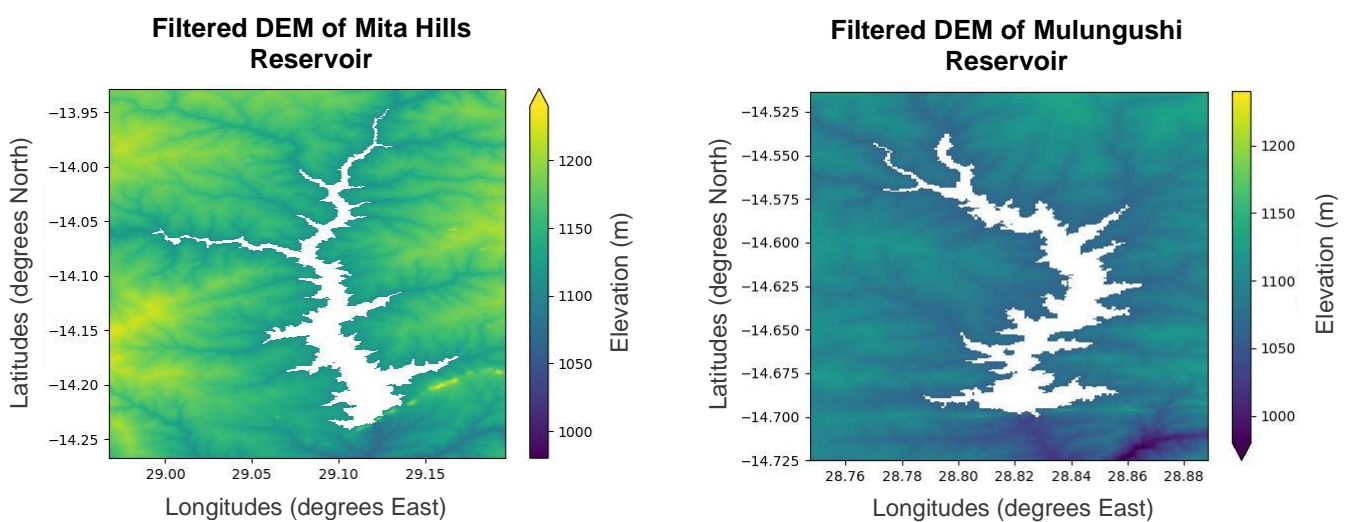

Figure 4.3: Elevation map of the Mita Hills reservoir (left) and the Mulungushi reservoir (right) in Zambia after filtering surface water cells, based on Hydro-MERIT elevation data. The remaining cells show the terrain elevation. Latitude and longitude are presented on the y- and x-axis, respectively, while elevation in meters is indicated by the colorbar (ranging from 900 to 1400 meters) on the z-axis.

The resulting output only include the cells that represent the reservoir surface water pixels, with all pixels upstream of the dam wall until the first elevation of the surrounding landscape removed as can be seen in the figure. Consequently, the remaining cells present the landscape prior to the filtering procedure.

4.1.3 Determining the Depth on Main Stream in Reservoir

In accordance with the methodology described in Step 4 in Figure 3.2, flow directions are determined for each reservoir to establish the main stream direction. As shown in Figure 4.4 for Mita Hills (left) and Mulungushi (right), the main stream flows from the most upstream cell towards the dam wall, which represents the outflow location in the reservoir.
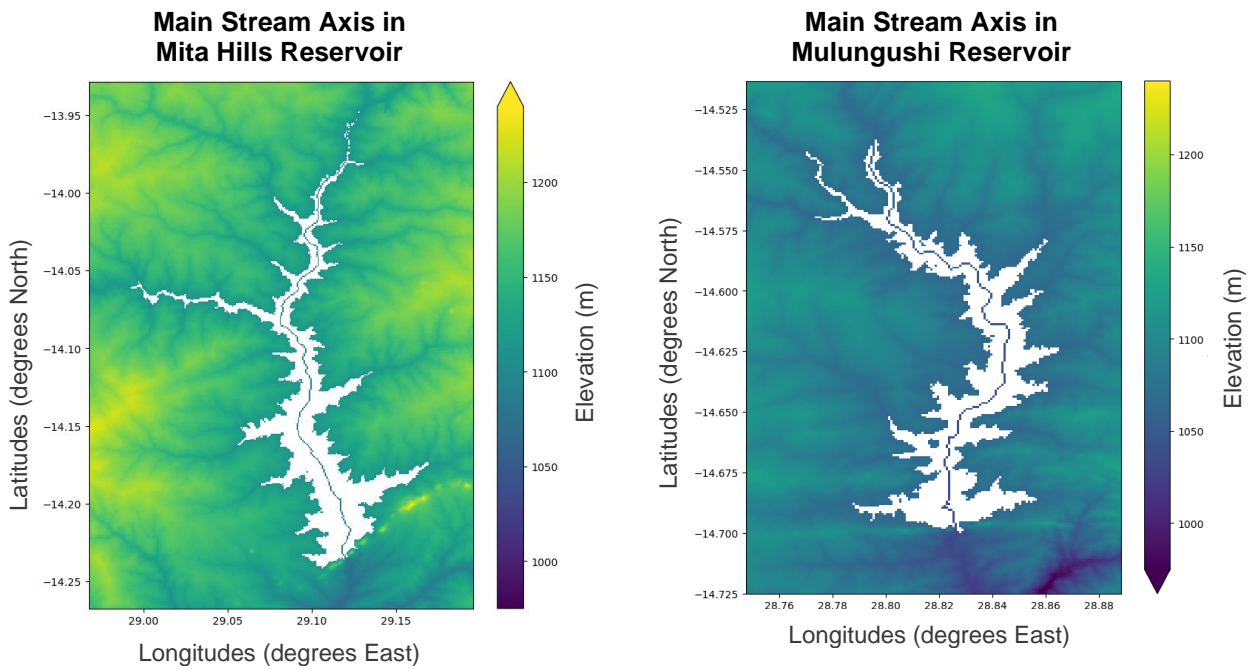
Figure 4.4: The elevation map of the Mita Hills (left) and Mulungushi (right) reservoir, with the main stream with the water surface filtered out, overlaid on the filtered elevation data. The main stream is identified based on the flow directions calculated following Section 3.1.3, and is represented by the line through the filtered area. The elevation data is obtained from the MERIT-Hydro dataset accessed through HydroMT (Eilander et al., 2023). The y- and x-axes represent latitude and longitude, respectively, while the z-axis represents elevation in meters as indicated by the colorbar ranging from 900 to 1400 meters.

As expected from the D8 method the main stream was found to roughly follow a central path through the reservoir. Subsequently, topographic depths are calculated for each cell along the main stream in accordance with the approach outlined in Step 5 of Figure 3.2. The resulting bathymetry for this line is presented in Figure 4.5 for Mita Hills (left) and Mulungushi (right).
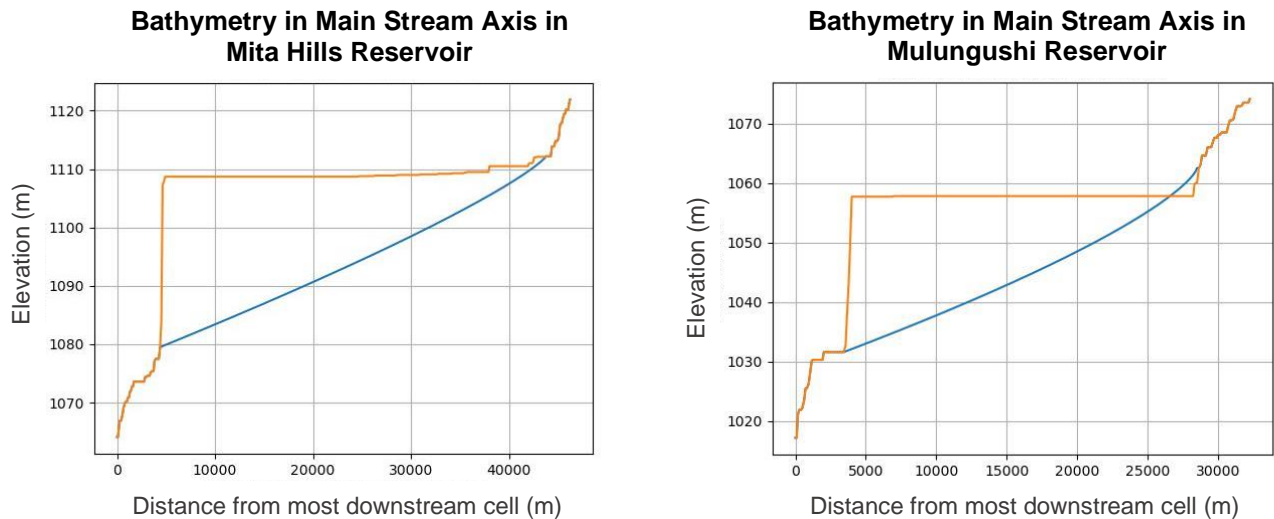

Figure 4.5: The cross-section of the main stream bathymetry and water surface elevation in the Mita Hills reservoir, with elevation in meters on the Y-axis and distance from the most downstream cell in meters on the X-axis. The water surface elevation is located at approximately 1109 meters for Mita Hills (left) and 1059 meters for Mulungushi (right), with the dam wall having a height of 119 meters and 26 meters. The length of the main stream is approximately 30000 meters, and the location of the main stream is shown in Figure 4.6. It can be seen that the bathymetry slightly incorporates flattenening of the reservoir bottom.

It is evident that the new bathymetry closely aligns with the surrounding upstream terrain and gradually flattens towards the dam wall downstream (note the dimension of the x-axis relative to the y axis). It is worth noting that in Mita Hills, the terrain downstream of the identified bottom of the dam wall is descending, while in Mulungushi, the bottom of the dam wall was identified at a point where the terrain begins to flatten downstream.

4.1.4 Identify the Stream Tributaries and Determining Associated Depths

In accordance with the procedure outlined in Figure 3.2 (*Step 5*), the tributaries of the reservoir are identified with a maximum Strahler order of 5 below the Strahler order of the main stream. This is set due to computational constraints. Figure 4.6 displays the identified tributaries for Mita Hills on the left, while the identified tributaries for Mulungushi are displayed on the right.
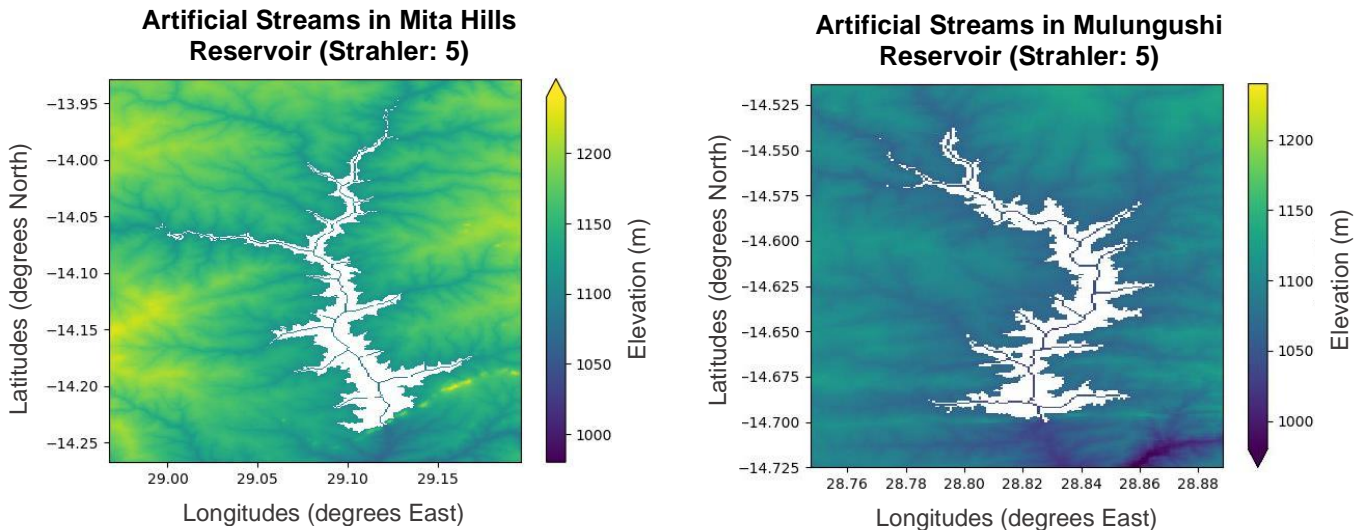

Figure 4.6: Tributaries plotted to the main stream presented in an elevation map of the Mita Hills reservoir (left) and the Mulungushi reservoir (right). The artificial streams are identified based on the flow directions calculated following Section 3.1 and is represented by the lines through the filtered area. The elevation data is obtained from the MERIT-Hydro dataset accessed through HydroMT (Eilander et al., 2023). The y- and x-axes represent latitude and longitude, respectively, while the z-axis represents elevation in meters as indicated by the colorbar ranging from 900 to 1400 meters.

As expected, the main tributaries of each reservoir exhibit identifiable streams. The bathymetry of each tributary is plotted, with the flattening of the elevation towards the intersection point with the main stream initially plotted within the reservoir.

4.1.5 Interpolation of the Bathymetry

The subsequent step in the method, as outlined in Section 3.1.3 and illustrated in Figure 3.2, involves determining the topographic depth for the cells that are filtered and thus are assigned no elevation values. Linear interpolation of the original elevation data and the surrounding elevations are employed to obtain the topographic depths, which are presented on the next page in Figure 4.7 for Mita Hills and Figure 4.8 for Mulungushi. The results show that the bathymetry for the cells with no elevation values has been successfully determined through linear interpolation of the surrounding elevations and the original elevation data, as illustrated in Figure 4.7 for Mita Hills and 4.8 for Mulungushi. The plots on the right provide a representation of the bathymetry, which appears to naturally fit into the surrounding landscape and the bathymetry naturally aligns with the terrain downstream. This also holds for the bathymetry in the main tributaries. However, this is not the case in the tributaries of the tributaries, where no stream axis was plotted.
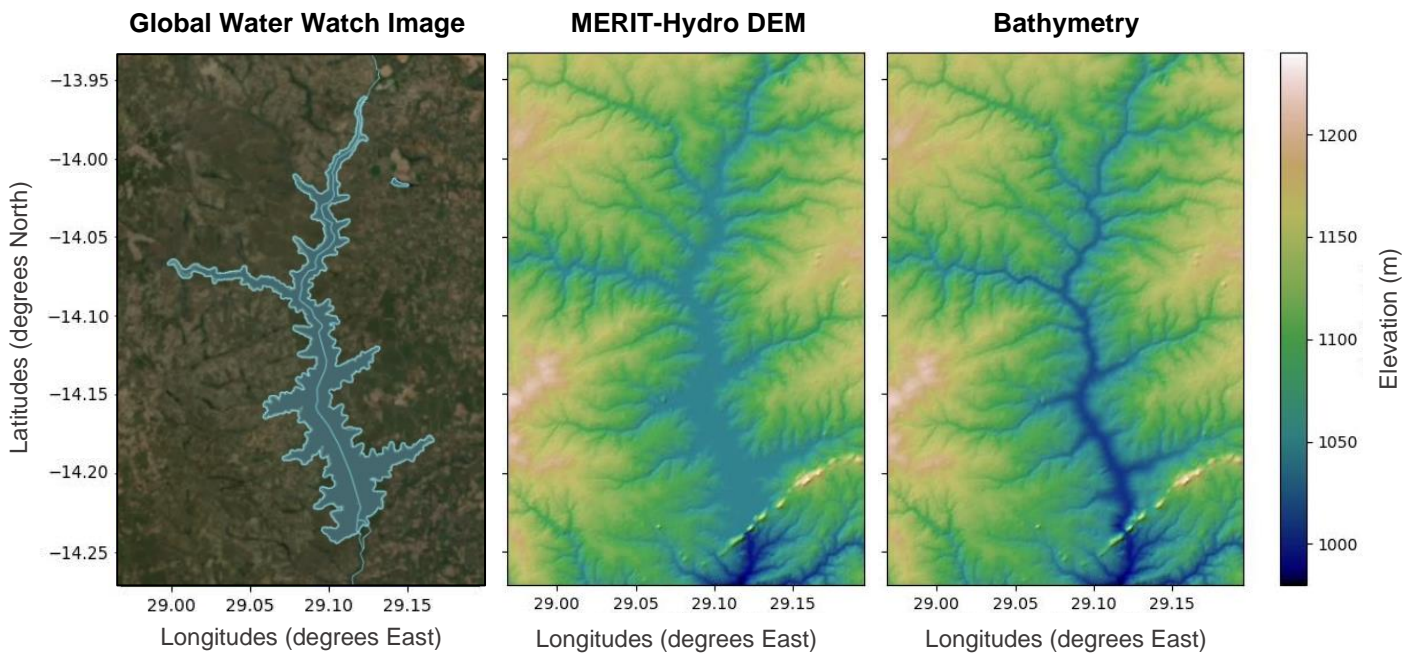
Mita Hills Reservoir, Zambia

Figure 4.7: Comparison of the elevation map of Mita Hills reservoir, with Global Water Watch image by Donchyts et al. (2016) (left), before (middle) and after (right) retrieval of the bathymetry. The original elevation data is retrieved from the MERIT-Hydro database accessed through HydroMT (Eilander et al., 2023). The bathymetry is obtained for each cell representing the water surface area using linear interpolation of the surrounding elevations. The resulting bathymetry data provide a more detailed representation of the reservoir's topography. The y- and x-axes represent latitude and longitude, respectively, while the z-axis represents elevation in meters as indicated by the colorbar ranging from 900 to 1400 meters.

Mulungushi Reservoir, Zambia
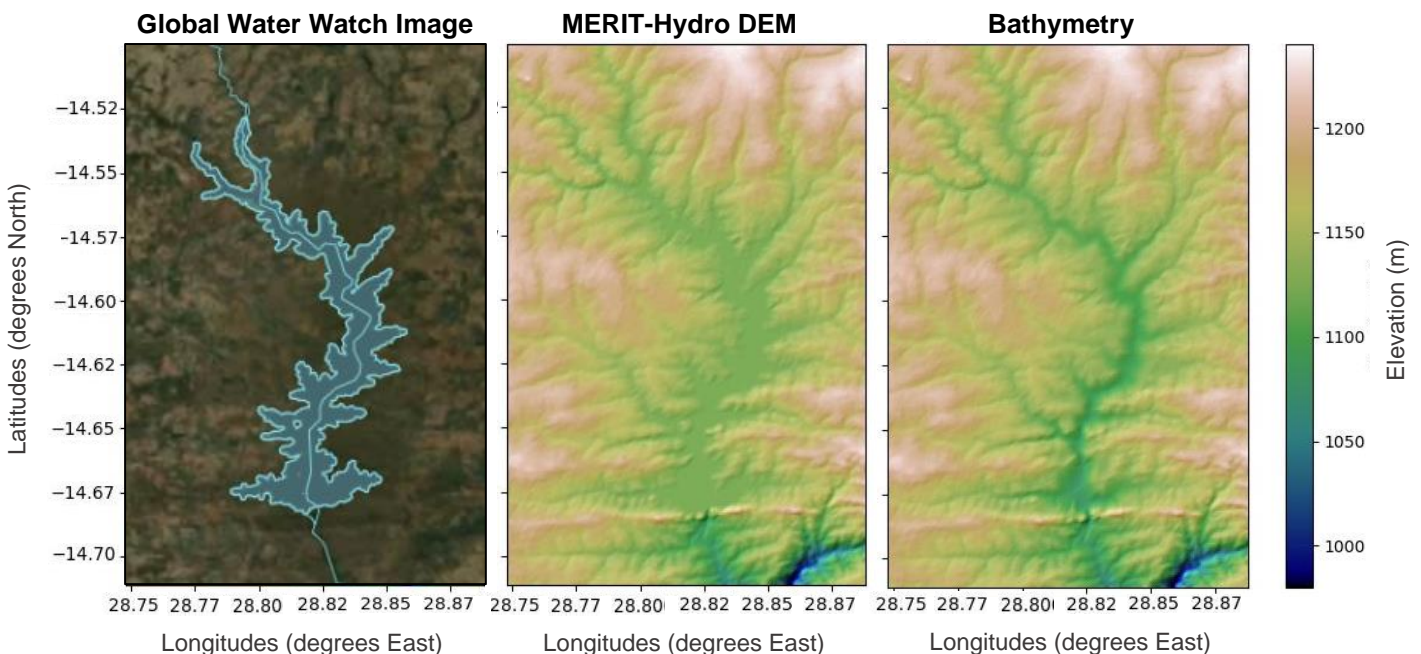
Figure 4.8: A similar comparison of the Mulungushi reservoir, with Global Water Watch image by Donchyts et al. (2016) (left), before (middle) and after (right) retrieval of the bathymetry. The original elevation data is retrieved from the MERIT-Hydro database accessed through HydroMT (Eilander et al., 2023). The bathymetry is obtained with linear interpolation of the surrounding elevations. The resulting bathymetry data provide a more detailed representation of the reservoir's topography. The y- and x-axes represent latitude and longitude, respectively, while the z-axis represents elevation in meters as indicated by the colorbar is similar to Figure 4.11.

4.1.6 Establishing the Hypsometric Relations

The hypsometric relation is established by deriving the reservoir bathymetry, following the methodology detailed in Section 3.1.3. The resulting hypsometry, which shows the relationship between volume and water for the Mita Hills and Mulungushi reservoirs, is presented in Figure 4.9.
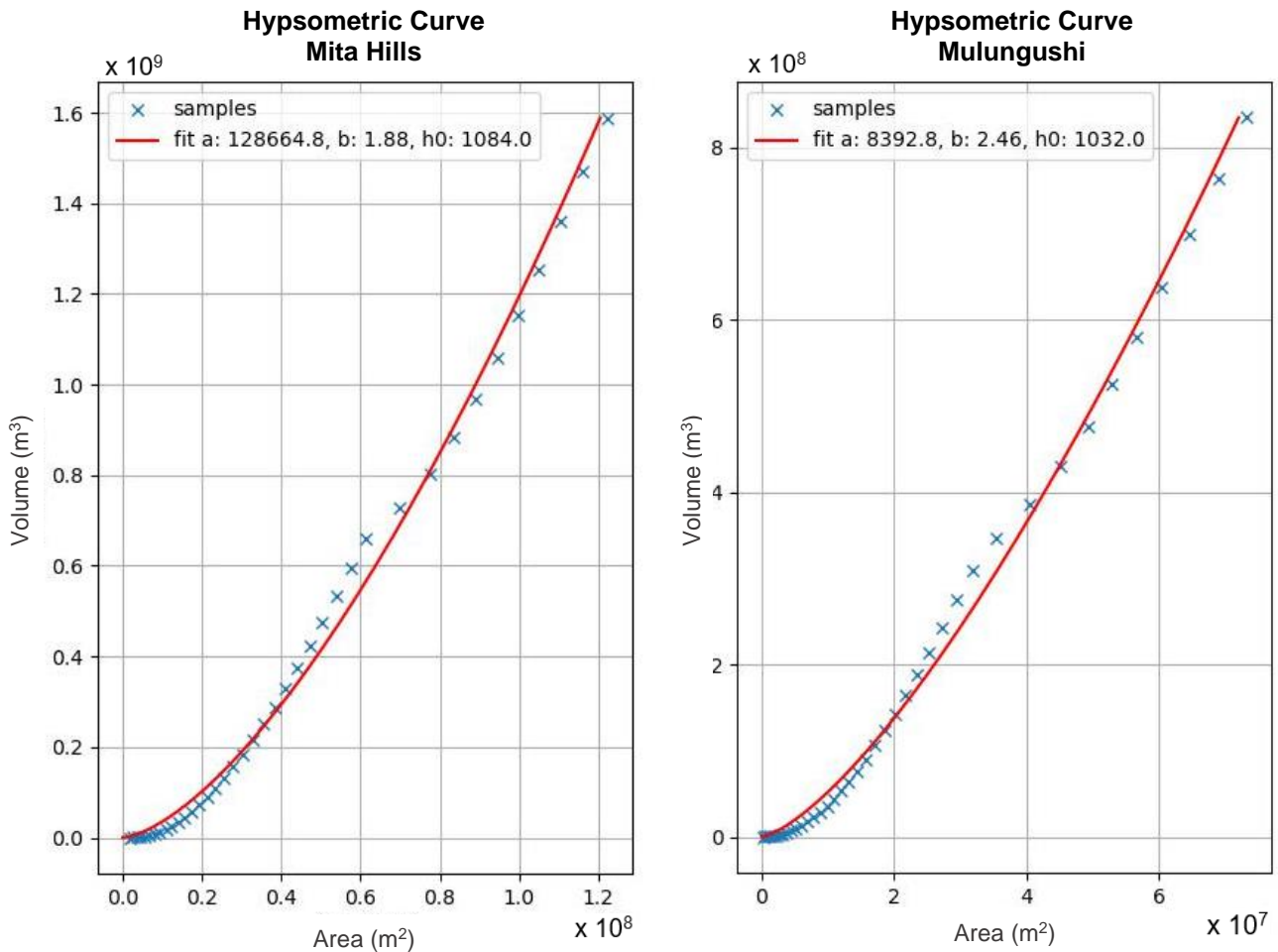

Figure 4.9: The hypsometric curves representing volume (m^3) and area (m^2) obtained with the novel method for the Mita Hills (left) reservoir and the Mulungushi reservoir (right) in Zambia. For each water level height the volume and the area is determined by the model, which allows for the relation establishement.

To derive the hypsometry, first the relation is established between water level and volume, and water level and area separately, which are detailed in Appendix B. The analysis reveals a non-linear relationship between the parameters, with larger area sizes corresponding to greater volume gains per step, consistent with the known characteristics of lakes and reservoirs, as discussed in Section 2.1.

In the results some deviations from the theoretical fit are observed in both the Mita Hills and Mulungushi reservoirs. Specifically, in the Mita Hills, a discrepancy is observed around an area of 60 km^2, with the volume diverging from the theoretical hypsometric fit. This finding suggests that for this area, there are smaller area gains for each increase in volume compared to what is predicted by the theoretical fit. However, around an area of 80 km^2, the samples meet the theoretical hypsometric fit again. Similarly, for Mulungushi, a similar deviation is observed around an area of 35 km^2 and 39 km^2.

4.1.7 Validation of the Hypsometric Curves in Mita Hills and Mulungushi

The validation of the results obtained through the novel method is done after retrieval of the modelled hypsometric curve. The validation results for the relationship between volume and water level are presented in the Figure 4.10 for Mita Hills (left) and Mulungushi (right).
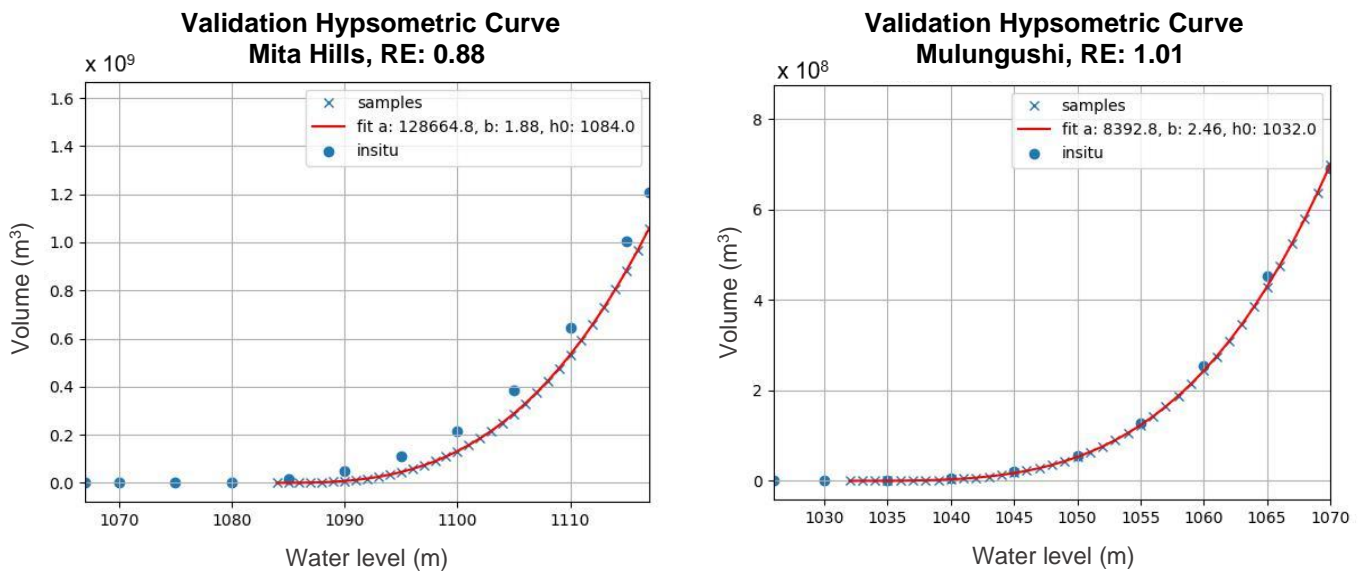

Figure 4.10: Validation of the hypsometric curves for volume (m^3) and water level (m) obtained with the novel method for the Mita Hills (left) reservoir and the Mulungushi reservoir (right) in Zambia. The blue dots, representing in-situ measurements, closely match the modeled hypsometric curve, shown as a red fit. Additionally, the relative errors (RE) for Mita Hills and Mulungushi are 0.88 and 1.01, respectively. This means that there was an underestimation of 12% for Mita Hills and an overestimation of 1% for Mulungushi in terms of their volumes.

As shown in the figures, a neat fit through the samples is observed for the volume versus water level relationship. The blue dots represent the in-situ samples, which closely align with the results obtained from the model for both Mita Hills and Mulungushi reservoirs. However, for the Mita Hills samples, it looks like an offset between the validation data and the model results would give a better result. For both reservoirs, the relative error is determined, and it was found to be 0.88 for Mita Hills and 1.01 for Mulungushi, which represents a 12% underprediction and 1% overprediction, respectively. These results demonstrate the effectiveness of the novel method in accurately predicting the relationship between volume and water level in the studied reservoirs.

4.2 The Novel Method Applied for Hypsometry in Indian Reservoirs

After establishment of the novel method, of which initial results are presented in previous Section 4.1, the novel method is employed to derive hypsometric curves for a larger validation dataset of Indian reservoirs. The dataset originally comprised 106 reservoirs; however, two of the reservoirs lacked an overlapping reference ID in the Global Water Watch database, and georeferenced data for 10 reservoirs could not be loaded due to an error in the algorithm, which, at the time of writing, has been resolved but due to time restrictions was not applied in the thesis. Consequently, the final dataset consisted of 94 reservoirs. This section presents both qualitative and quantitative analyses of the derived hypsometric curves for each reservoir in the validation dataset.

4.2.1 Qualitative Analysis of Hypsometry in Indian Reservoirs

The qualitative analysis involves visually inspecting all bathymetry plots of the main streams' reservoir-by-reservoir. The spatial distribution of the performance for the 94 reservoirs is illustrated on the map of India in Figure 4.11.

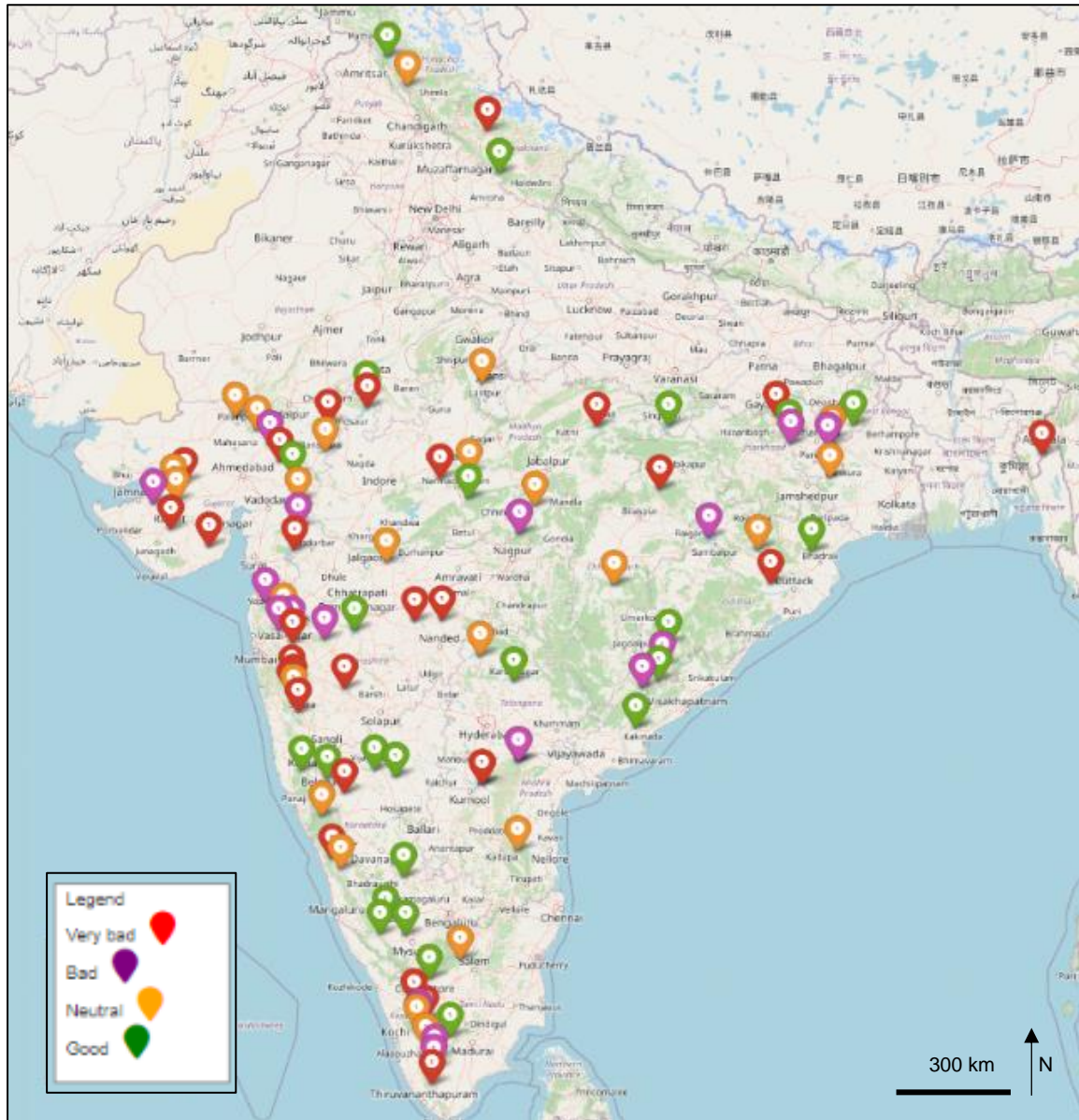# The Map of India and The Qualitative Analysis of 94 Reservoirs

Figure 4.11: A map of India indicating the locations of the 94 reservoirs included in the validation dataset for analysis. The arrows are color-coded to indicate the results of the qualitative analysis, which involves a visual inspection of the bathymetry drawn on the main stream axis. Red arrows represent reservoirs classified as "Very Bad," where no recognizable bathymetry is present. Purple arrows indicate "Bad" performance, where a recognizable bathymetry is present but with poor scores. "Neutral" performance is represented by orange arrows, where the bathymetry is clearly drawn with significant room for improvement. Finally, green arrows represent reservoirs classified as "Good" based on the quality of their drawn bathymetry.

The bathymetry plots on the relevant axis are classified into four categories based on their quality: "Very Bad" (red), where no form of bathymetry can be recognised is observed in 28 reservoirs "Bad" (purple), where a poorly drawn bathymetry is visible in 18 reservoirs, "Neutral" (orange), where a bathymetry is clearly drawn and looked good, but with room for improvement in 24 reservoirs, and "Good" (green), where the bathymetry is perfectly drawn in 24 reservoirs. There is no clear spatial pattern observed, although reservoirs with well-drawn bathymetry were somewhat clustered in the southwest and more evenly distributed in other parts of the country. Reservoirs with poorly performing bathymetry are predominantly clustered in the middle-west and more evenly spread throughout the rest of the country. Figure 4.16 – 4.19 provide examples on the classified bathymetry interpolations among the Indian reservoir data.
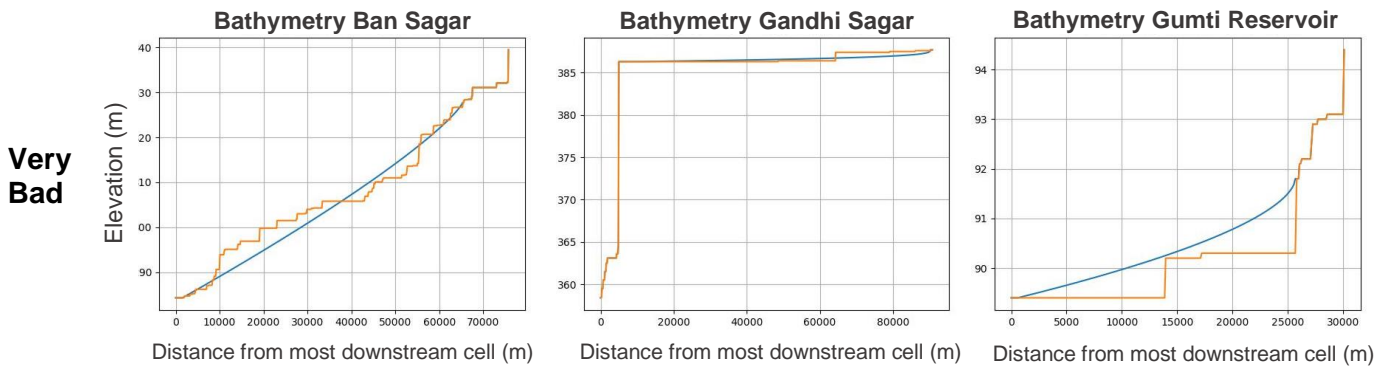
Figure 4.12: Three examples of bathymetry plots on the main stream that are classified as "*Very Bad*" due to their poor quality, which represent 28 out of 94 reservoirs in the Indian validation dataset. These plots are insufficient in presenting the bathymetry of the reservoirs, and are found to contain three distinct error scenarios: (1) a plot that failed to align with the cells located closest upstream and downstream of the reservoir (left), (2) a barely visible plot (middle), and (3) a plot that is partially above the current elevations (right).
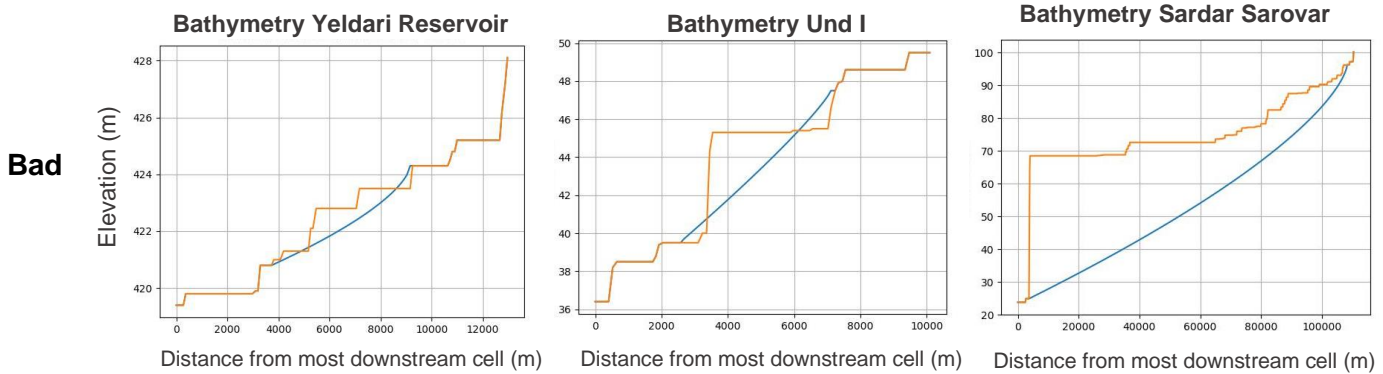

Figure 4.13: Three examples of bathymetry plots on the main stream that are categorized as "*Bad*" which accounted for 18 of the 94 reservoirs in the Indian validation dataset. Although these plots do present the reservoir bathymetry, the quality of the presentation is deemed inadequate. This category of plots exhibits three distinct error scenarios: (1) a plot that fails to align with the cells located closest upstream and downstream of the reservoir, covering multiple smaller horizontal patches (left), (2) a similar error in failing to snap the upstream and downstream cells but covering only one reservoir, resulting in a smaller error (middle), and (3) a plot with incorrect upstream or downstream alignment (right), leading to a significant under- or over-prediction of the reservoir volume.
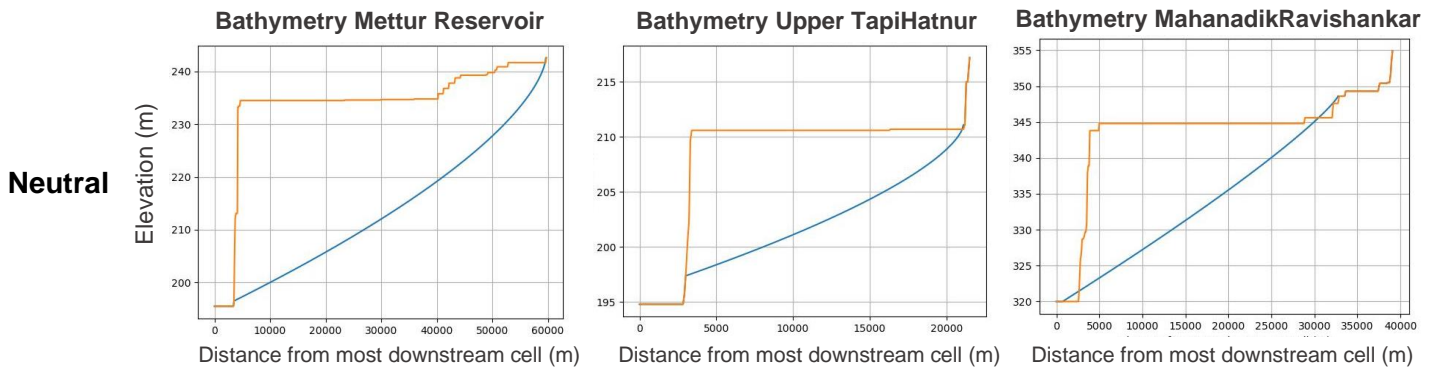
Figure 4.14: Three examples of bathymetry plots on the main stream that are classified as "*Neutral*", comprising 24 of the 94 reservoirs in the Indian validation dataset. These plots demonstrate an acceptable performance for the bathymetry on the main stream, although there is room for improvement, as indicated by the following: (1) a plot that fails to align with the nearest onshore upstream cell (left), (2) a plot that fails to align with the nearest downstream cell (middle), and (3) a plot in which both upstream and downstream cells are almost but not perfectly aligned, although the impact on the bathymetry is minimal. It is expected that these errors will not lead to significant inaccuracies in the results.

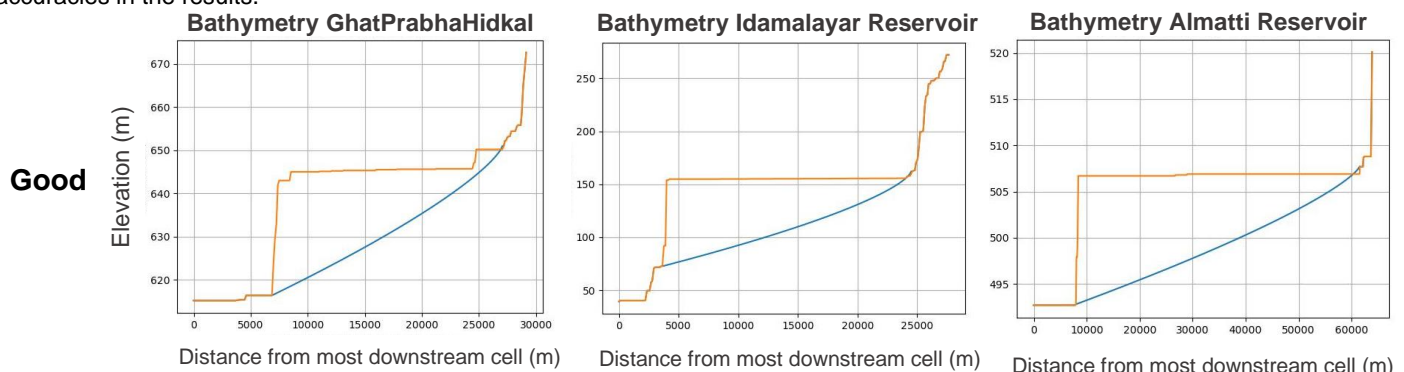**Figure 4.15:** Three examples of bathymetry plots on the main stream that are categorized as "*Good*" and show a perfect bathymetry plot, which account for 24 of the 94 reservoirs in the Indian validation dataset.

The reservoirs classified as "Bad" and "Very Bad" are excluded from further analysis, reducing the validation dataset to 48 reservoirs that were either classified as "Neutral" or "Good". It is important to note that there are numerous other ways to classify reservoirs, such as their size, shape, number of tributaries, whether they are fully man-made or partly natural, and soil type/geomorphology. These characteristics may provide valuable insights into the performance of a reservoir. However, given the scope of this thesis and the limitations of future research, they will not be explored further. Instead, the emphasis is placed on the quality of the bathymetry estimate on the main stream.

4.2.2 Quantitative Analysis of Hypsometry in Indian Reservoirs

A quantitative analysis is performed on a sample of 48 reservoirs in this study. For each reservoir, the coefficient of determination is calculated using the method described in Section 3.1.4. The analysis is based on the maximum capacity of each reservoir, which is determined as 100% of the maximum in-situ measurement recorded during validation. Figure 4.16 and 4.17 presents the correlation between the validation volume (in-situ) and the modelled volume for each reservoir.
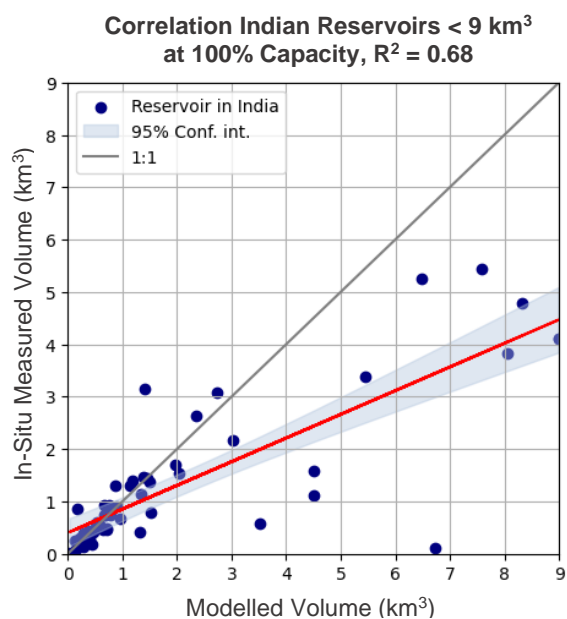

Figure 4.16: The correlation between in-situ measured volumes and modelled volumes for each Indian reservoir in the validation dataset. The coefficient of determination (r^2) for this correlation is found to be 0.68. The y-axis represents the in-situ measured volumes from the validation dataset, while the x-axis represents the modelled volumes.
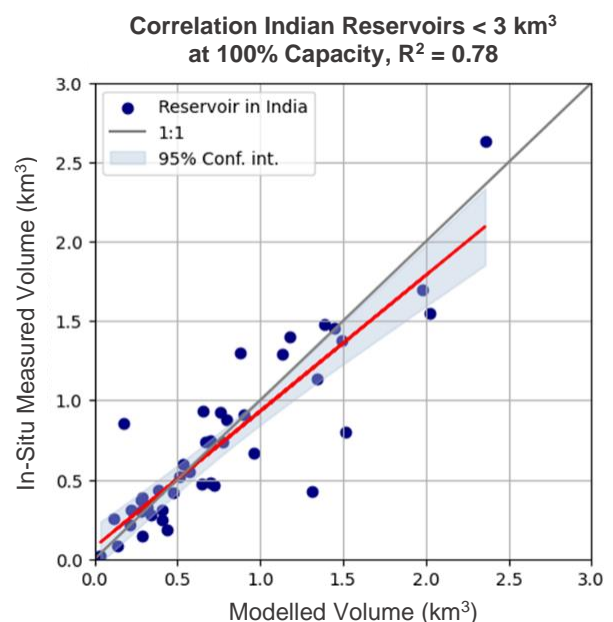
Figure 4.17: The correlation between in-situ measured volumes and modelled volumes for Indian reservoirs in the validation dataset that are smaller than 3 km^2. The coefficient of determination (r^2) for this correlation is found to be significantly better than that for the entire dataset, as it is 0.78. The y-axis represents the in-situ measured volumes from the validation dataset, while the x-axis represents the modelled volumes.

In the figures, the coefficient of determination (r^2) for all 48 reservoirs is found to be 0.68, as shown in Figure 4.20. The 95% confidence interval is represented by the blue shaded area. Notably, when focusing on reservoirs that are smaller than 3 km^3, which accounted for 43 of the 48 reservoirs in the sample, the coefficient of determination significantly improved, as shown in Figure 4.17. Specifically, the r^2 value for this subset of reservoirs is found to be 0.78. The analysis reveals that the model tends to overpredict reservoir volumes, particularly for larger reservoirs. A potential explanation for this observation could be attributed to the usage of distinct datums in the in-situ measurements and the novel method employed in this study. In particular, the in-situ volumes are reported against a local reference elevation, which could be for example the lowest operating level. In contrast, the novel method utilised in this research relies on the MERIT-Hydro dataset, which is vertically referenced to EGM96 (Minderhoud et al., 2019).

4.2.3 Hypsometry Performance for Varying Filling States

The quantitative study included an evaluation of model performance for different reservoir fillings. Figure 4.18 displays the correlation between modelled and validation (in-situ) data for reservoirs smaller than 3 km^3 at fillings of 0%, 25%, 50%, 75% of the water level relative to maximum in-situ measured capacity, as outlined in Section 3.1.5.
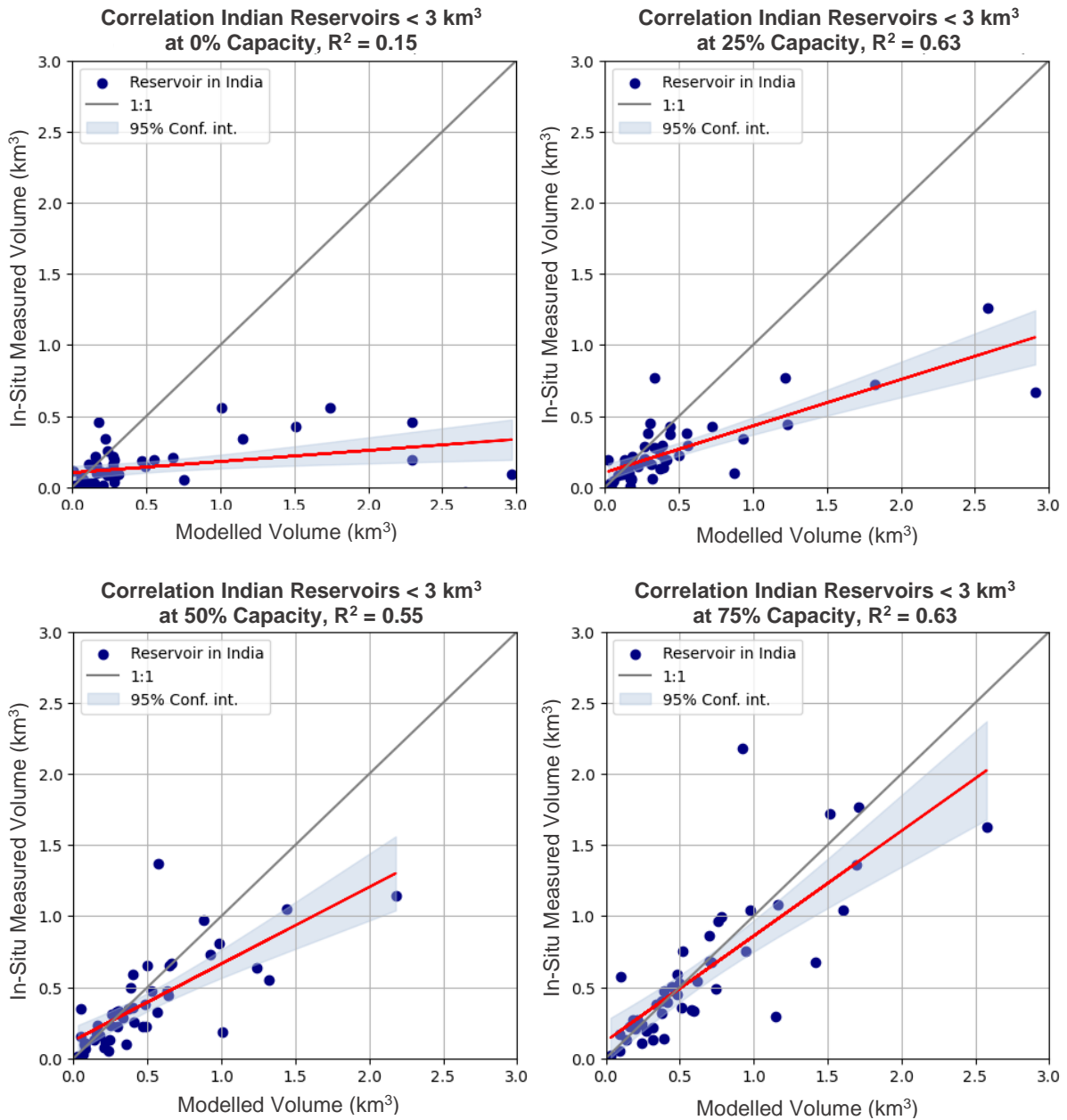
Figure 4.18: The correlation between in-situ measured volumes and modelled volumes for Indian reservoirs in the validation dataset with a maximum capacity below 3 km^3. The y-axis shows the in-situ measured volumes, while the x-axis represents the modelled volumes. The coefficient of determination (r^2) increases as the reservoirs reach higher fillings. Please refer to the previously presented Figure 4.16 and 4.17 for the correlation at maximum capacity.

The performance for filling at maximum capacity is shown previously in Figure 4.16 and Figure 4.17. Also, for some of the Indian reservoirs at 25% filling the validation data meets the reporting datum, such as the minimum operating level, while the remotely sensed method still reports a significant volume, affecting the coefficient of determination (r^2) score.

4.2.4 The Relative Error for Reservoirs Varying in Size and Location

In accordance with the method discussed in Section 3.1.5, the performance of the model was evaluated for each of the 48 Indian reservoirs in the validation dataset relative to their size, by computing the relative error. As shown in Figure 4.19, the relative error is presented on a spatial plot for each reservoir.

The Map of India and The Relative Error of 48 Reservoirs
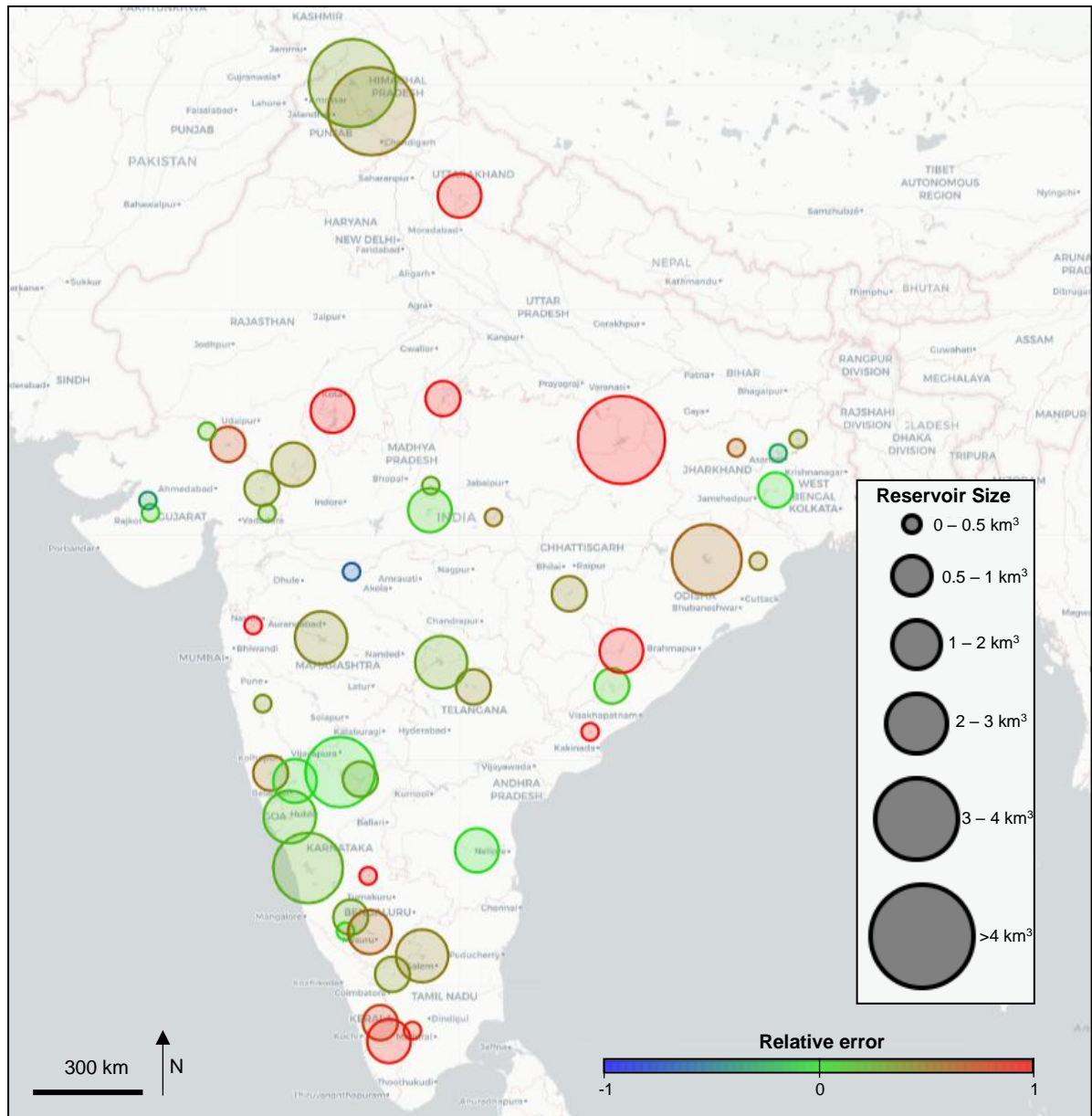
Figure 4.19: A spatial plot of the relative error for each of the 48 Indian reservoirs in the validation dataset, calculated according to the method described in Section 3.1.5, with circle size representing maximum in-situ measured capacity. The color of each circle indicates the relative error, where green represents a perfect fit, red an overestimation, and blue an underestimation. Notably, smaller reservoirs (below 3 km^3) located in central India tend to have better model estimations and are overestimated by maximum 1.5 times, while poorer estimations are found in the northern and southern regions of the country.

Each circle represents a reservoir, and its size corresponds to the maximum in-situ measured volumetric capacity. The colour of the circle represents the relative error, where green represents a perfect absolute estimate, red represents an overfit, and blue represents an underfit. A relative error of 1 indicates that the model overestimates the volume by at least a factor two, indicating a poor estimation. The smaller reservoirs (below 3 km^3) located in the central region of the country are generally estimated well or overestimated by less than 1.5 times. Conversely, complete bad estimations are found in the northern and southernmost parts of the country.

64

4.2.5 Attempt to Correct for Distinct Datum

Following the method in Section 3.1.6, an effort is done to address the systematic errors observed between the validation and modelled data. Although this approach significantly improved the relative error in many reservoirs, it was not effective in all cases. Some reservoirs still exhibited a large relative error, as presented in the upper examples in Figure 4.20, with relative errors of 6.56 and 2.43 which indicate an extreme overestimation with 556% and 143%, respectively.
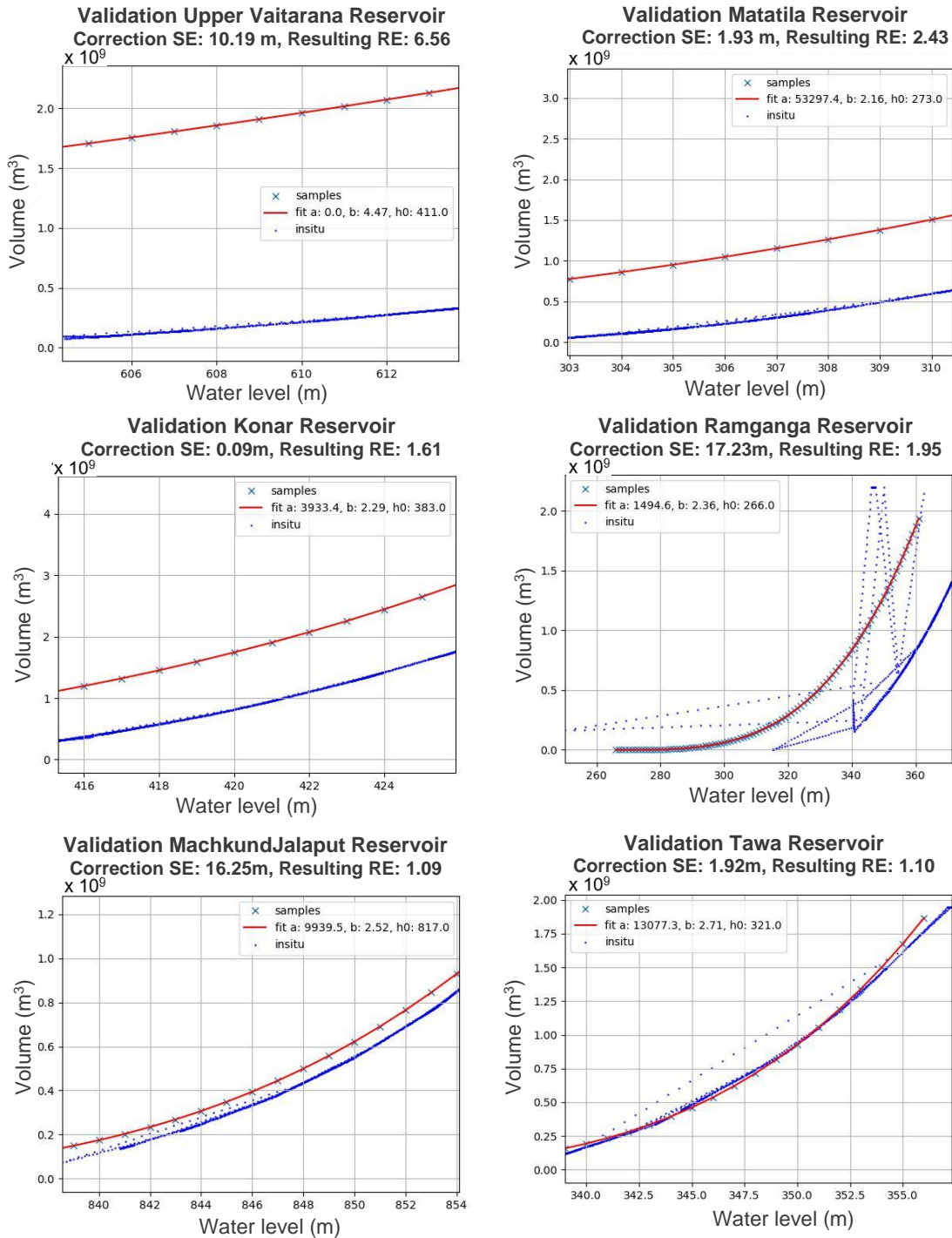
Figure 4.20: The validation results of the hypsometric curve for six reservoirs in the Indian dataset. The validation data is denoted by the blue curve, whereas the modeled result is represented by the red curve. The volume (m³) is plotted against the water level (m) on the y-axis and x-axis, respectively. The figure title indicates the size of the automated correction with "Corr" (m), and the relative error is denoted by RE. The systematic error is denoted by SE. The results reveal that the correction applied was not always sufficient to entirely eliminate the distinct offsets. Additionally, certain reservoirs in the validation dataset exhibit significant outliers.

The automated correction applied to these cases is not successful enough in those reservoirs, resulting in a negative correction of -10 meters and -1.9 meters to account for the offset. Conversely, the lower graphs in Figure 4.20 demonstrate successful correction attempts, resulting in relative errors of 1.09 (left) and 1.10 (right), indicating a 9% and 10% overestimation, respectively. The middle left and top graphs also exhibit an offset in both cases, and the middle right graph includes examples of outliers in the validation dataset.

4.3 The Novel Method outperforms Messager et al. (2016)

The ability of the novel method to estimate the reservoir bathymetry and establish the hypsometric curve is compared to a method for bathymetry reconstruction presented by Messager et al. (2016). The results of this benchmark experiment are presented in the following Sections.

4.3.1 Comparing the Novel Method to Messager et al. (2016)

The bathymetry is reconstructed for the 48 reservoirs in the Indian validation dataset according to the suggested method by Messager et al. (2016) which incorporates the flattening of the reservoir bottom towards the centre of the reservoir. The bathymetry is calculated for flattening parameters k of 0.90, 0.95 and 0.97, of which the validation versus modelled volume is shown in Figure 4.20 at a water level of maximum capacity.
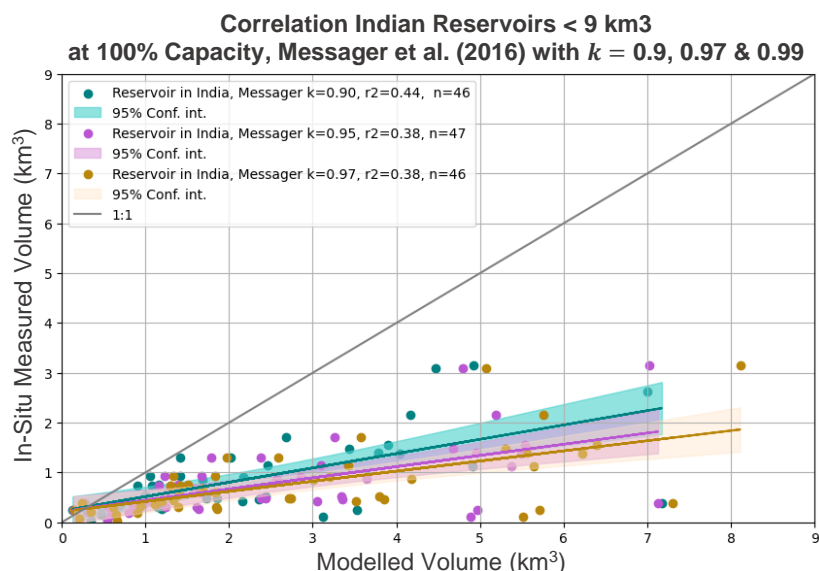
Figure 4.20: Correlation plot of the volumes in the Indian reservoirs at maximum water level computed for the different k values 0.90, 0.95 & 0.97 according the the method as proposed by Messager et al. (2016). The insitu measured volumes are plotted on the y-axis and modelled volumes are plotted on the x-axis. Each dot represents a reservoir volume calculated eigher with one of the values for k. From this plot it can be derived that the k value 0.90 provides the best overall score for reservoirs with maximum in-situ measured capacities of < 9 km^3.

The varying numbers of plotted reservoirs n is due to that some reservoirs calculated are larger than 9 km^3, for each of the k. The Figure shows that for $k = 0.90$ the coefficient of determination is highest. The results of a qualitative analysis of the bathymetry maps are presented in Figure 4.21, that presents the original the bathymetry as presented by Messager et al. (2016) with $k = 0.90$ for the Krishnaraja Sagar reservoir in India.

Figure 4.21: Spatial elevation maps of the Krishnaraja Sagar before the bathymetry estimate the bathymetry estimate according to the method as proposed by Messager et al. (2016) with k = 0.90. The coordinates are presented on the y-axis and the x-axis. The elevations are presented in the colors on the z-axis. The Messager et al. (2016) derived bathymetry shows sudden jumps in elevation. Also it tends to show a deeper estimate of the overall reseservoir depth.
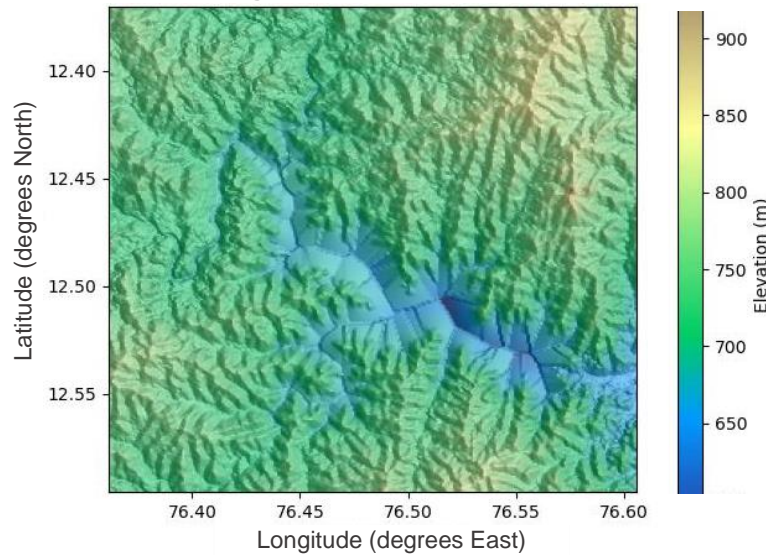
The Messager et al. (2016) plot shows a large depth in the reservoir bathymetry. Also, it is clear from the spatial map that the method by Messager et al. (2016) shows sudden jumps in elevations according at harsh edges in the reservoir, which is an expected outcome in the approach of Messager et al. (2016), because it determines the topographic lake depth by making use of the nearest onshore values. The correlation at a maximum in situ measured water level for all reservoirs in the Indian dataset for both the novel method presented in this thesis (green) is compared with the correlation obtained by the method by Messager et al. (2016) (blue) in Figure 4.22. The coefficient of determination r^2 of the novel method is 0.68, representing a 32% underestimation, relative to the r^2 of 0.44 which is achieved by the Messager et al. (2016) method, representing a 56% underestimation.
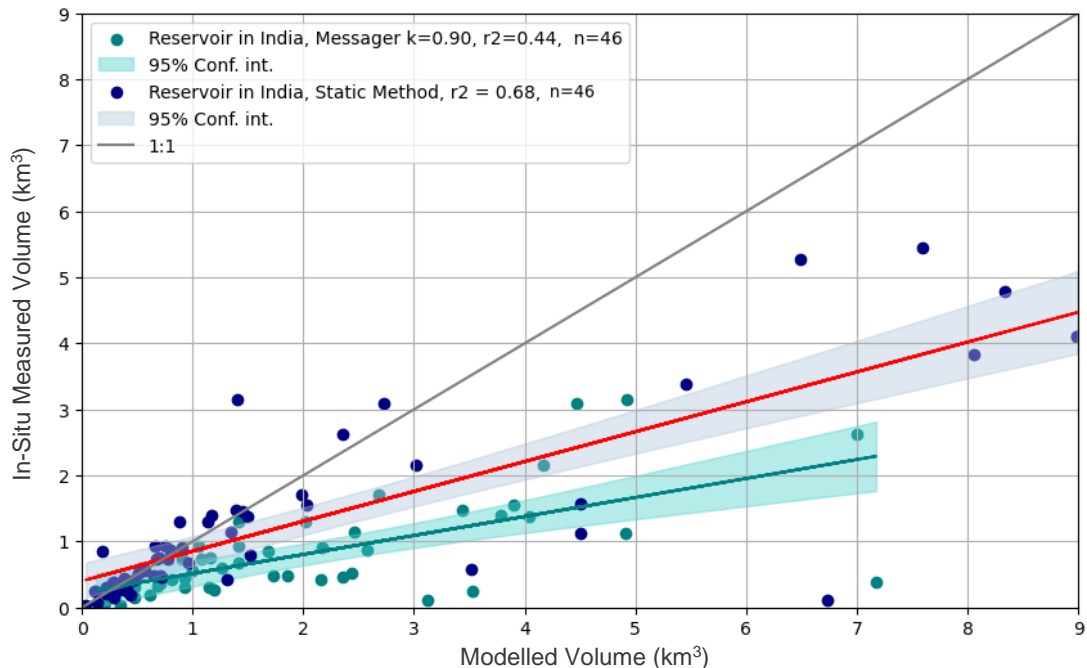
Figure 4.22: A comparison between two distinct techniques for correlating modelled volumes with in-situ measured volumes. The blue and red data points represent the novel method, while the green data points correspond to the method proposed by Messager et al. (2016). The latter method is executed with a k value of 0.9. The grey line indicates a perfect correlation, with a 1:1 relationship between the modelled and in-situ measured volumes. The results of this analysis suggest that the novel method performs better than the method proposed by Messager et al. (2016) when applied to Indian reservoirs. Each dot on the graph represents a reservoir volume computed using either of the two methods.

4.4 The Predictive Performance of the Novel Methods' Volume Time Series

Regression models are utilised to investigate the potential of volume time series data in predicting water availability for two reservoirs, namely, the Hawane reservoir located in Eswatini and the Katse reservoir situated in Lesotho. The models are constructed with varying combinations of predictors, for which its time series are presented below: volume, precipitation, and SPEI for the Hawane reservoir (Figure 4.23).
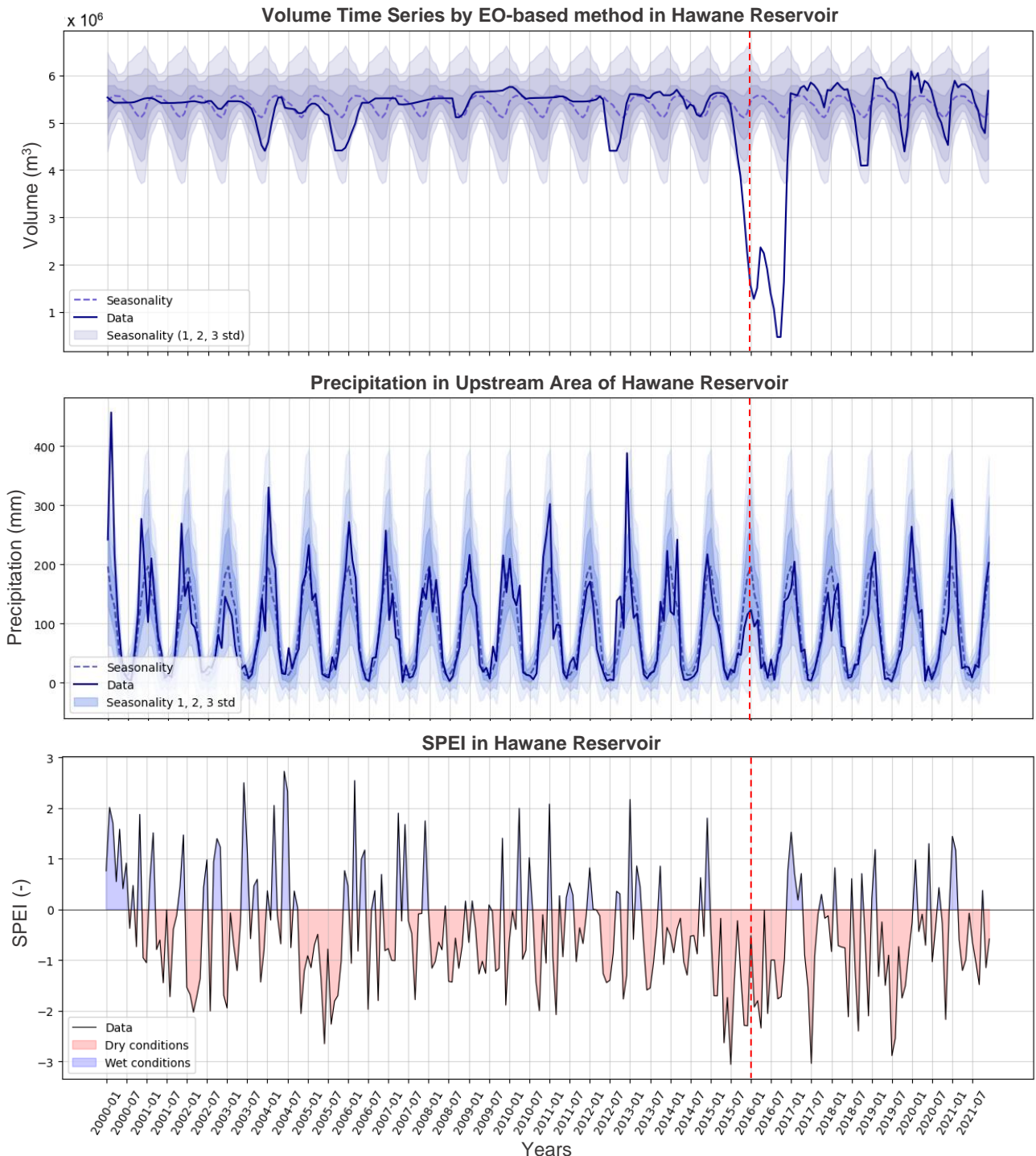
Figure 4.23: The time series of volume (m^3) (top), precipitation (mm) (middle), and monthly SPEI (-) (bottom) for the Hawane reservoir in Eswatini. These three variables are utilised as predictors in various regression models. The seasonality of volume and precipitation, calculated over two periods (2000-2015 and 2017-2021, excluding an extreme drought event), is illustrated in the background with dotted lines and their respective 1, 2, and 3 standard deviations. The red dotted line indicates the middle of the 2015-2016 wet season, which is characterized by lower than expected rainfall. During this time period, the volume time series shows a decrease by more than 3 standard deviations, the precipitation time series indicates a reduction by 1 standard deviation, and the SPEI of > -1.5 reveals extreme dry conditions.

The autocorrelation in the volume time series in the Hawane reservoir is presented in Figure 4.24.
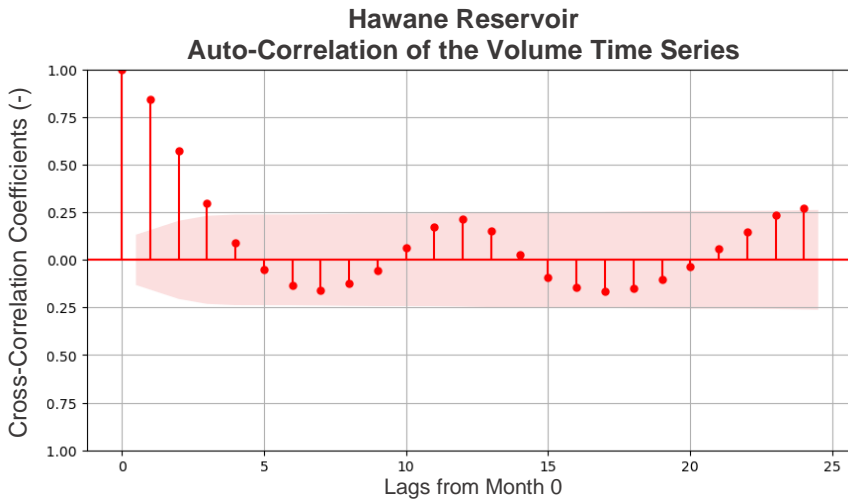
Figure 4.24: Autocorrelation analysis conducted on two years of volume time series data from the Hawane reservoir in Eswatini. The Pearson correlation coefficient is presented on the y-axis, while the lagged months relative to the dependent month (Month 0) are presented on the x-axis. The band, determined by Formula 2.6, represents the area where data is considere "white noise" is displayed in pink shading. The figure demonstrates that up to three months prior to the dependent month there is an indication of memory that can be utilised for prediction of the volume in Month 0.

The figure indicates that there are three preceding months, including the current month with a correlation that significantly varies from zero. Therefore, the autocorrelation takes three previous values into account. The lagged cross-correlation for the precipitation time series and the volume in the respective month 0 is shown in Figure 4.25.
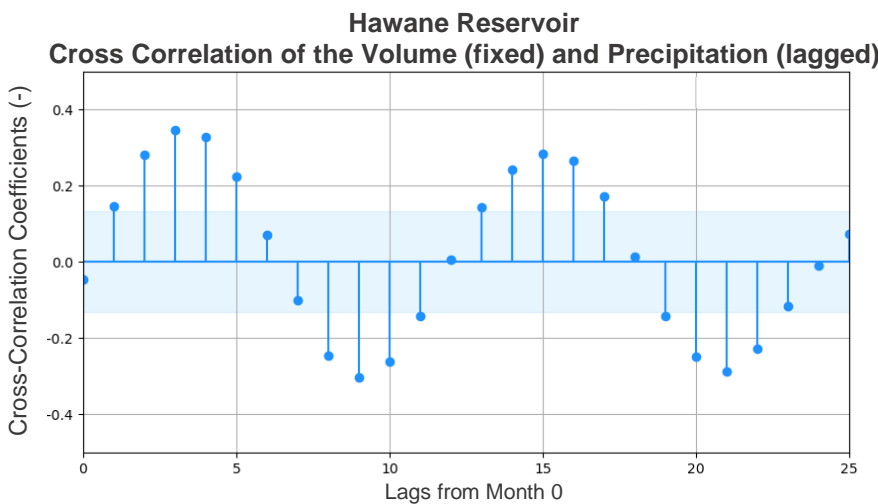
**Figure 4.25:** The cross-correlation between lagged-precipitation and volume in the month of interest (Month 0) conducted on two years of volume time series data from the Hawane reservoir in Eswatini showing strong seasonality. The cross-correlation coefficient is presented on the y-axis, while the lagged months relative to the dependent month (Month 0) are presented on the x-axis. The band, containing 95% of all values, is displayed in blue shading. The figure demonstrates that up to five months prior to the dependent month there is an indication of significant correlation that can be utilised for prediction of the volume in Month 0.

It can be observed that there are up to 5 values that are significantly deviating from the blue band. This means that 5 observations in history are taken as input in the regression model. The cross-correlation between SPEI and the volume in the respective month are presented in Figure 4.26.
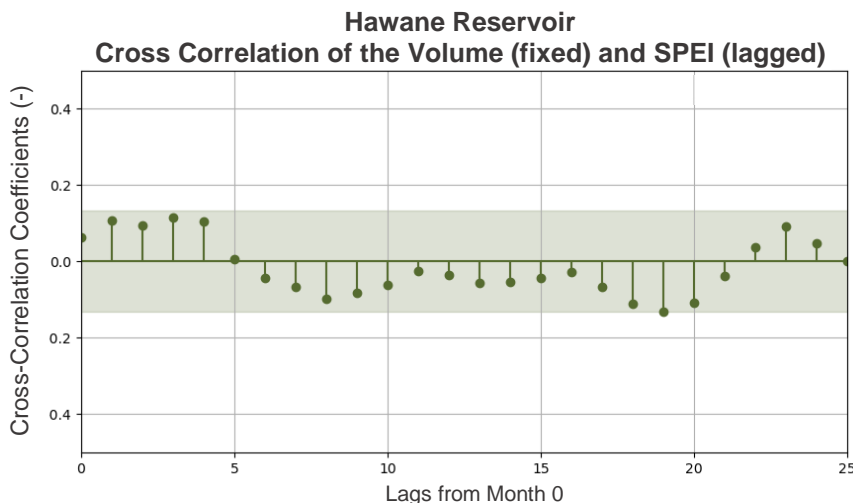
Figure 4.26: The second cross-correlation plot, but now with the lagged-SPEI and volume in the month of interest (Month 0) conducted on two years of volume time series data from the Hawane reservoir in Eswatini. The axis are similar to Figure 4.25. The band, containing 95% of all values, is displayed in green shading. The figure demonstrates that there is no significant correlation between the two variables. Therefore it should be noted that there is a possibility that the observed results occurred by chance.

Figure 4.26 shows no significant deviation from zero. No significant aggregated correlation is found between the lagged SPEI and the volume in the respective month, as demonstrated in Figure 3.16. Despite this finding, other studies have shown successful analysis of water availability or deficits through the use of similar type of climate indices in regression models (Dibike, et al., 2016; Ghasemi, et al., 2021; Jiao, et al., 2021; Gurrapu, S., et al., 2021; Li, et al., 2023). Thus, in this study, we will continue the analysis using three SPEI values, which is consistent with the number of months taken for the model. However, it is important to note that the lack of significant linear correlation raises the possibility that the observed results may have occurred by chance.

To assess the added predictive capability of each predictor regression models are employed. The models produced 6-month forecasts for each month of the year, resulting in a total of 72 forecasts per year. In the following three pages, the analysis is shown of the following figures: Figure 4.27 depicts the outcomes of the regression models applied to the Hawane reservoir from April 2015, with a projection of six months into the future. Similarly, Figure 2.28 displays the predictions made one year later, in 2016, following a notably arid wet season. Figure 4.29, on the other hand, showcases the progression of predictions across the months, beginning in May and forecasting six months ahead before advancing to June, July, and subsequent months.

Figure 4.27: The volume predictions with the distinct regression models for the Hawane reservoir, accompanied by precipitation (top) and SPEI (2nd from above) time series.

The forecast starts in April 2015 and predicts up to a maximum of 6 months lead time. The forecast commences from the midpoint (indicated by a black cross) of the chart and features the asso-ciated uncertainty range, represented by 1, 2, and 3 standard deviations, alongside each forecast. The wet season (i.e., October to April) is highlighted by the blue background, while the seasonal trend, and its of the associated uncertain-ty range, is denoted by the gray line and shades.

The models shown are an autoregressive model of the volume (red), a multi-linear regression (MLR) model of volume and precipitation (blue), a MLR model of volume and SPEI (green), a MLR with precipitation only (purple) and a MLR with SPEI only (yellow).

It can be observed from the graphs that all graphs show relatively similar behaviour, probably because the SPEI and precipitation do not deviate from seasonality during this period.
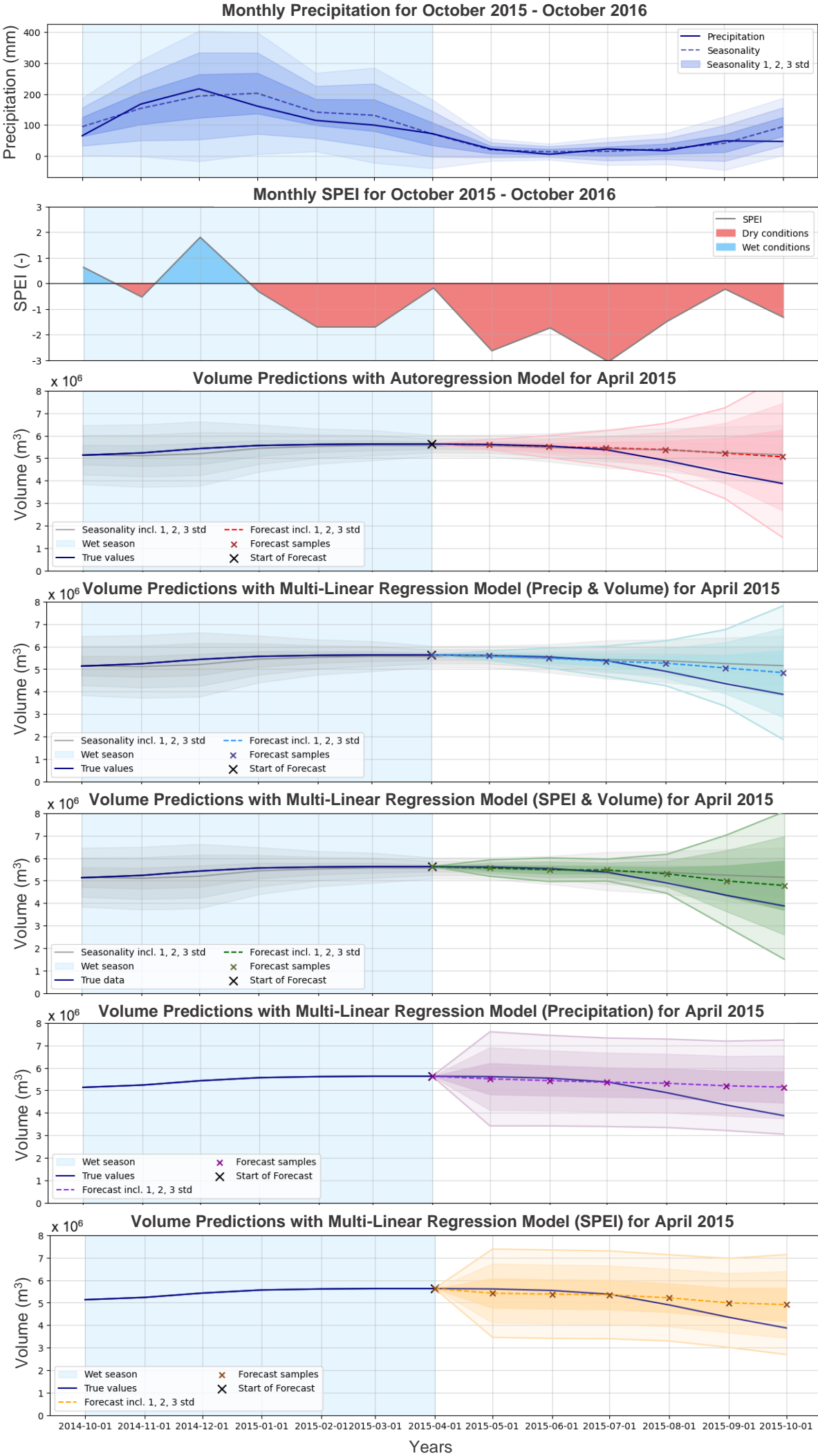
Figure 4.28: The volume predictions with the distinct regression models for the Hawane reservoir, accompanied by precipitation (top) and SPEI (2nd from above) time series.

The forecast starts in April 2016 and predicts up to a maximum of 6 months lead time. The forecast commences from the midpoint (indicated by a black cross) of the chart and features the asso-ciated uncertainty range, represented by 1, 2, and 3 standard deviations, alongside each forecast. The wet season (i.e., October to April) is highlighted by the blue background, while the seasonal trend, and its of the associated uncertain-ty range, is denoted by the gray line and shades.

The models shown are an autoregressive model of the volume (red), a multi-linear regression (MLR) model of volume and precipitation (blue), a MLR model of volume and SPEI (green), a MLR with precipitation only (purple) and a MLR with SPEI only (yellow).

It can be observed from the graphs that especially the MLR with volume and SPEI show additional predictability up to 4 months lead time.
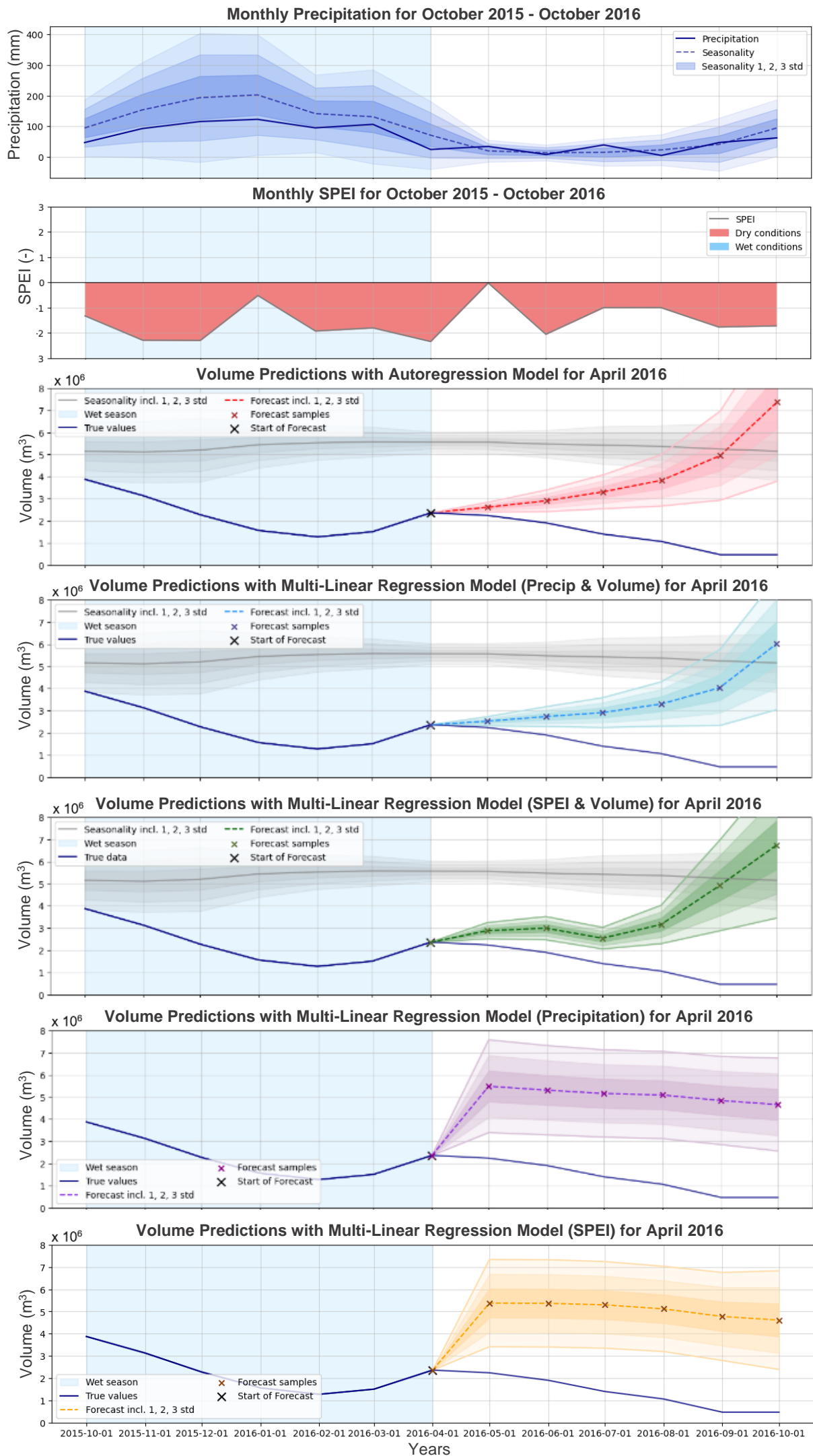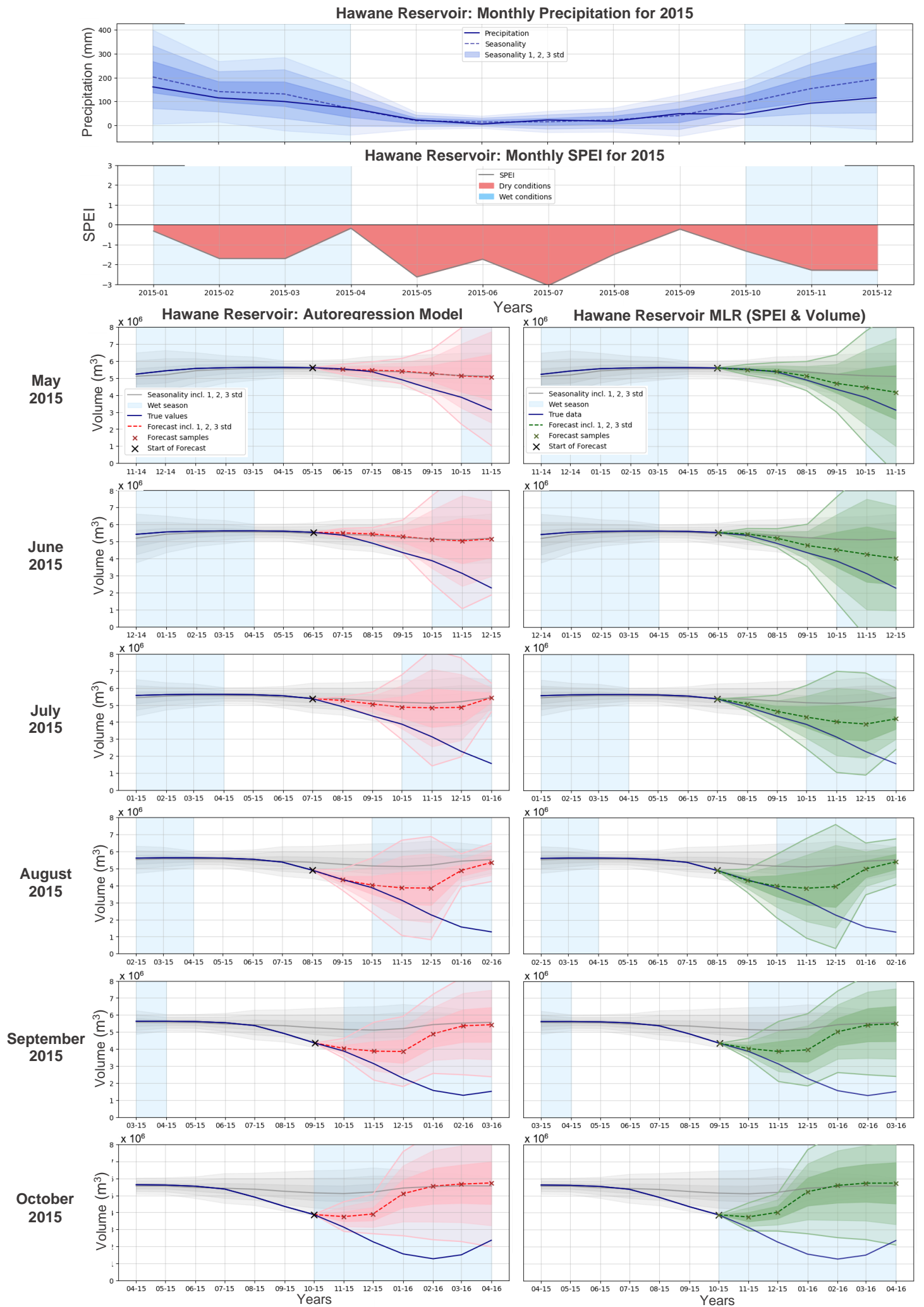
Figure 4.29: The volume predictions for Hawane reservoir moving through different starting months (please read from top to bottom), accompanied by the precipitation (mm) and SPEI (-) time series. Each prediction contains 6 months lead time starting from each month between May and October 2015 using volume (autoregression) and SPEI & volume (Multi-linear regression).

The following paragraphs will discuss Figure 4.27, Figure 4.28 and Figure 4.29. Figure 4.27 and Figure 4.28 present a forecast starting in April 2015 and April 2016. For each April, all regression models are presented in the figure, accompanied by separate sub-figures displaying the precipitation and Standardized Precipitation Evapotranspiration Index (SPEI) time series (upper two sub-figures). Figure 4.29 represents the behaviour of the model when moving through different starting months. In all figures, the volume time series is analysed in an autoregressive model (in red), hereinafter referred to as V_{auto}, which incorporates the values of the preceding three months that exhibit significant correlation with the respective month. Additionally, four multilinear regression models are employed. These models are analysed individually, with the precipitation model being referred to as P_{MLR} (in purple). The SPEI model, on the other hand, is referred to as $SPEI_{MLR}$ (in orange). Additionally, the models are evaluated in combination with volume, with the precipitation (in blue) and SPEI models (in green), respectively. These combined models are referred to as $V-P_{MLR}$ and $V-SPEI_{MLR}$. When considering precipitation, values from six preceding months are included, based on the lagged correlation discussed in Section 3.3.4.2. For SPEI, values of the preceding three months are included.

The first forecast in Figure 4.27, starting in April 2015, shows that the observed precipitation during the first half of the wet season fluctuates around the expected seasonal precipitation within one deviation. However, during the second half of the wet season, the precipitation tends to be lower than the seasonal expectations, which is a period in which the SPEI indicates dry conditions. The SPEI shows extreme dry conditions following the 2014-2015 wet season, while the precipitation does not deviate significantly from the seasonality. This might be because temperatures are relative to the low occurrence of precipitation, which is further discussed in Section 5.5. The regression models predict that the volume will follow its seasonal trend until July. Afterward, V_{auto} (red), P_{MLR} (purple), and $SPEI_{MLR}$ (yellow) fail to predict a significant decrease in volumes, although V_{auto} (red) still predicts the true values to be within one standard deviation. $V-P_{MLR}$ (blue) and $V-SPEI_{MLR}$ (green) predictions indicate slightly improves predictive skill relative to V_{auto} (red). From August onwards, these predictions correctly predict a decrease in volume compared to the seasonal trend, with $V-SPEI_{MLR}$ (green) predictions performing the best. The discussion on this figure is continued in Section 5.6.

The second forecast in Figure 4.28, starting in April 2016, comes right after the 2016 wet season that had decreased precipitation. The precipitation time series throughout the entire wet season deviated around one standard deviation, with the SPEI indicating dry conditions with SPEI values of -2. Volume time series extremely deviated and are observed far below three standard deviations from the seasonal expectation. Right after the wet season, the dry conditions continued, which follows expectations as the dry season started. The lack of water availability is captured in all regression models that included volume time series. The V_{auto} (red) shows decreased volume estimates relative to seasonality but failed to capture the ever-decreasing trend in the volume. $V-P_{MLR}$ (blue) only shows slightly better predictive skill than V_{auto} (red). The $V-SPEI_{MLR}$ (green) shows the best predictive skill, deviating from the seasonal expectation up to four months lead time, however predicting the volume to be refilled again in August, which was not the case. All models that considered volume time series tend to overestimate the seasonal occurrence in the prediction for a 6-month lead time and therefore failed to capture the ever-decreasing trend in volume. The P_{MLR} (purple) and $SPEI_{MLR}$ (yellow) directly deviate towards the seasonal trend and fail to represent the water scarcity scenario. The observations are further discussed in Section 5.6.

The third forecast, presents in Figure 4.29, provides an overview of the 2015 forecasts of the V_{auto} (red) and $V-SPEI_{MLR}$ (green) predictions up to 6 months lead time starting in May to October. The precipitation in 2015 follows the seasonal pattern early in the year, while staying within one standard deviation from normal. In the end of 2015, the precipitation significantly decreases and deviates from the seasonal pattern, indicating start of the 2016 drought event. Yet, extremely dry conditions preceding the 2016 drought event are already indicated by the SPEI throughout the whole year, especially around May and July, where the SPEI is around -2.5 and -3. April and September, on the other hand, are periods that show relatively medium SPEI circumstances. When comparing the V_{auto} (red) and $V-SPEI_{MLR}$ (green) predictions, there is added predictability found in the $V-SPEI_{MLR}$ (green) predictions and V_{auto} (red) is found to follow the seasonal pattern. The predictability in $V-SPEI_{MLR}$ (green) increases while the dry season is proceeding in August, where the model shows significant predictions for volume to go down below the threshold of 3 standard deviations from the seasonal expectation. After August, both V_{auto} (red) and $V-SPEI_{MLR}$ (green) fails to predict further decrease of volumes. The models and observations are further elaborated on in Section 5.6.

The Heidke Skill Score (HSS) is a widely used metric to evaluate the effectiveness of forecasting models and is, in this study, used to assess the models in predicting significant decreases in reservoir volume by one standard deviation. The calculation formula is described in Formula 3.15. Figure 4.30 represents the HSS for V-SPEI$_{MLR}$, which outperformed V-P$_{MLR}$ and V$_{auto}$, despite their relatively similar performance.
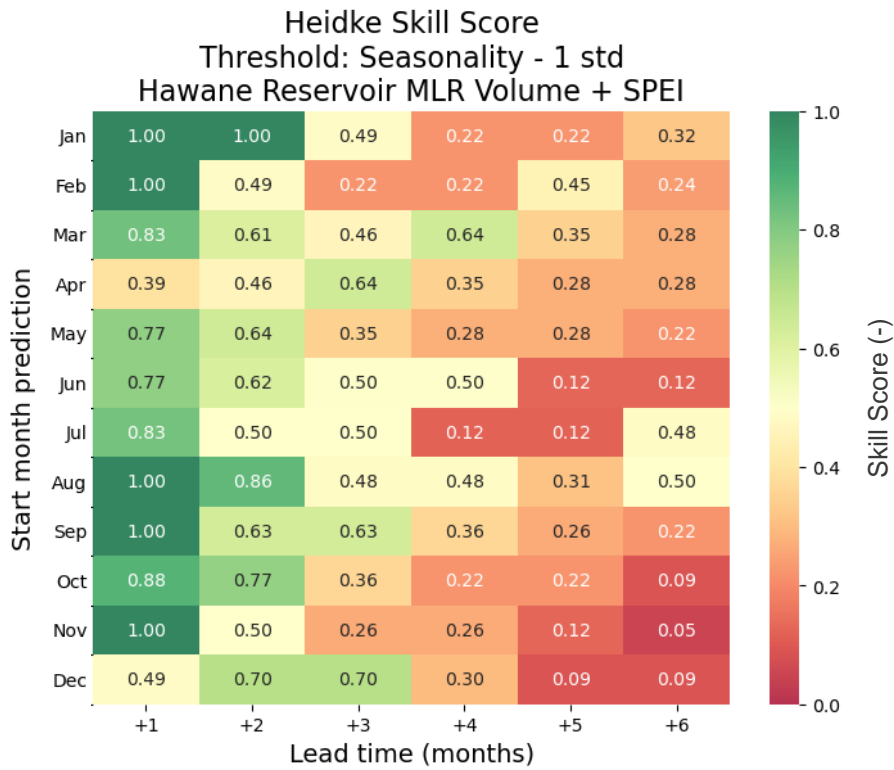
Figure 4.30: The performance of V-SPEI$_{MLR}$ model in predicting whether the true values deviate from the seasonality by 1 standard deviation is presented using the Heidke Skill Score (HSS), presented in Forumla 2.8. The HSS scores are colorcoded to indicate performance, with green indicating good performance and red indicating poor performance. The associated HSS values are also presented, with a score of 1 indicating good performance and a score of 0 indicating poor performance. The y-axis displays the starting month for each prediction, while the x-axis represents the lead time up to which the prediction is made. It is noteworthy that the results show a generally good performance for the first month in predicting deviations from seasonality. However, as the lead time increases, the performance of the model tends to decrease, which is as expected due to the increasing uncertainties in future forecasts.

The HSS values for all other models are available in Appendix F. Notably, the models that exclude volume time series, show similar performance to P$_{MLR}$ and perform poorly, as further elaborated in Section 5.6. The y-axis displays the starting month for each prediction, while the x-axis represents the predicted lead time up to 6 months. The HSS scores are displayed on a grid and color-coded, with a score of 1 indicating relatively good performance (green) and a score of 0 indicating poor predictive ability (red). The results indicate that the model performs well in predicting the threshold for one month ahead, particularly at the beginning and end of the wet season. As expected, the performance decreases as the prediction lead time increases due to increasing uncertainties in future forecasts. However, in July and August, the performance of the model for the 6-month lead time predictions shows an improvement compared to the preceding months. This is discussed in more detail in Section 5.6.

Also, the Heidke Skill Score for only SPEI$_{MLR}$ is provided in Figure 4.31.
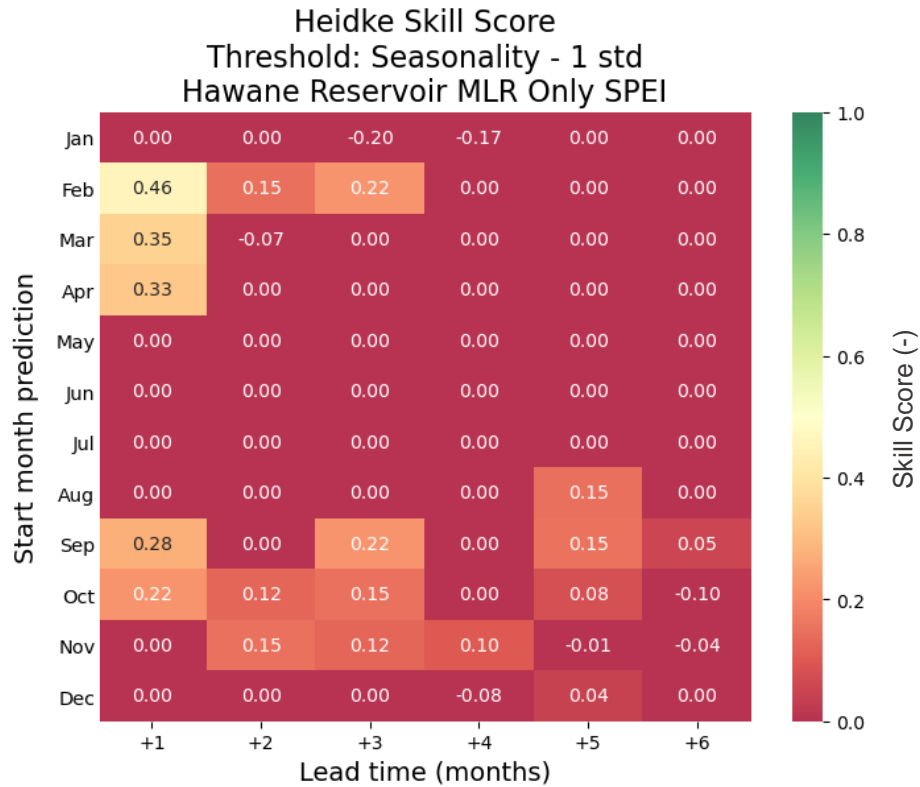
Figure 4.31: The Heidke Skill Score (HSS) for a range of predictions generated by the SPEI$_{MLR}$ model, which solely relies on SPEI time series. As always, a score of 1 indicates good performance and a score of 0 indicaties poor performance. Also the cells are colorcoded. The majority of forecasting scenarios utilizing this model exhibit insignificant skill in predicting values below one standard deviation from normal. Nonetheless, some degree of added predictability is observed in the months of February through April, as well as September and October, for one-month-ahead predictions. Additionally, little improvement in predictive ability is evident for lead times up to five months in the months of September through November.

The SPEI$_{MLR}$ model, which solely relies on SPEI data, displays limited proficiency in predicting values below one standard deviation from normal in the majority of forecasting scenarios. However, there is some degree of enhanced predictability during the months of February through April, as well as September and October, for one-month-ahead predictions. Nevertheless, the predictive ability exhibits slight improvement for lead times up to five months during the months of September through November.

4.5   Additional Analysis to SPEI

The additional analysis in the Katse Dam is done for the V-SPEI$_{MLR.}$ Figure 4.32 represents the SPEI (middle, SPEI-3 (bottom) and volume time series (top) in the Katse Dam.
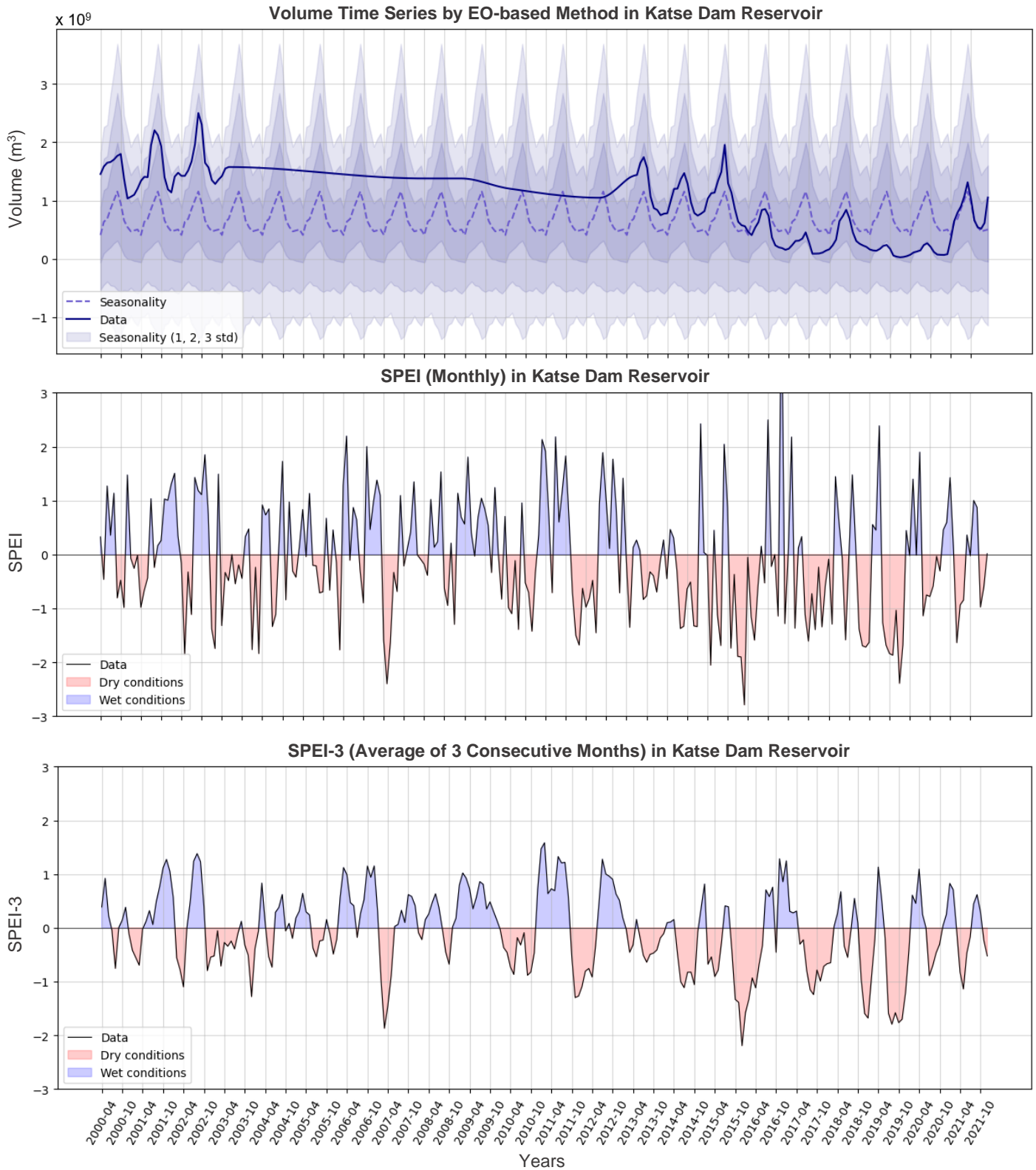
Figure 4.32: The volume time series in the Katse Dam (top), the monthly SPEI (middle), and the 3-month moving average of SPEI (SPEI-3). The volume time series exhibits fluctuations that follow the seasonal trend, with a notable period of relative constancy where limited data points are available, which are filtered from the data before calculation of the seasonal trend. Additionally, the SPEI-3 displays a pattern that is more analogous to the observations in the volume time series.

The study of Hawane Dam revealed that the V-SPEI$_{MLR}$ model exhibited the best performance in predicting whether the reservoir volume will deviate from the seasonal expectation by 1 standard deviation. However, it is also observed that the SPEI predictor does not display any lagged correlation with the volume in the respective month, as illustrated in Figure 4.26. Additional analysis is done to investigate the hypothesis that the lack of correlation between these two variables is mainly caused by the relatively constant water volume in the training data of the Hawane reservoir. Therefore, the predictive performance of the V-SPEI$_{MLR}$ and the V$_{auto}$ models are tested on the Katse reservoir in Lesotho, which exhibited greater variations in water volume in its training dataset. Figure 4.32 represents the SPEI (middle, SPEI-3 (bottom) and volume time series (top) in the Katse Dam.

The water volume time series of Katse dam is presented at the top of Figure 4.32. The figure illustrates clear seasonal fluctuations in the water level during the periods 2000-2003 and 2012-2021. However, the intervening period exhibits a rather constant trend, which is attributed to the limited observations in the remotely sensed dataset that is employed to capture the trend in volume. Notably, the mean water volume during the period 2012-2021 declined by approximately 5 x 10^8 m^3 relative to 2000-2003, which could be attributed to a variety of factors that will be discussed in Section X. Therefore, the dataset excludes the period 2003-2012 while predicting the seasonal mean. Also, the year 2013 is excluded as it was chosen to be the test data for the regression model. Figure 4.33 also includes the monthly SPEI and its 3-month moving average (SPEI-3), which is computed to test the hypothesis that the lack of correlation between the SPEI and the volume time series is due to the differences in dynamics.
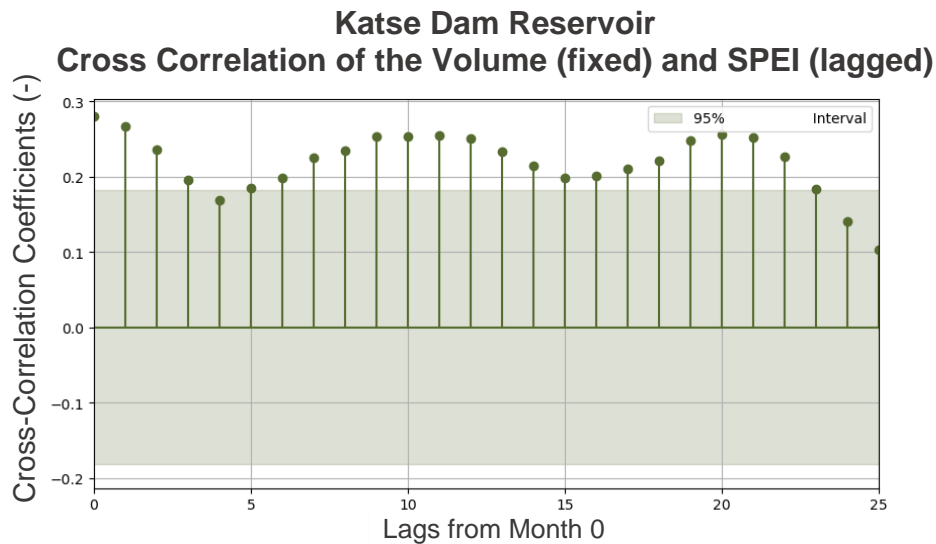
Figure 4.33: The cross-correlation between lagged-SPEI-3 and volume in the month of interest (Month 0) conducted on two years of volume time series data from the Katse reservoir in Lesotho. The cross-correlation coefficient is presented on the y-axis, while the lagged months relative to the dependent month (Month 0) are presented on the x-axis. The 95% confidence interval is displayed in green shading. The figure demonstrates that up to four months prior to the dependent month there is an indication of significant correlation that can be utilised for prediction of the volume in Month 0.

As expected, the SPEI-3 shows smaller extremes in SPEI compared to the SPEI-1 but exhibits less variation and therefore has a more similar pattern to the volume time series. In contrast, the SPEI-1 displays numerous positive and negative peaks during a period when the volume time series only has one peak. This can be observed, for example, around November 2016 and November 2019.

The correlation between the lagged SPEI-3 time series and the volume in the respective month is presented in Figure 4.34.
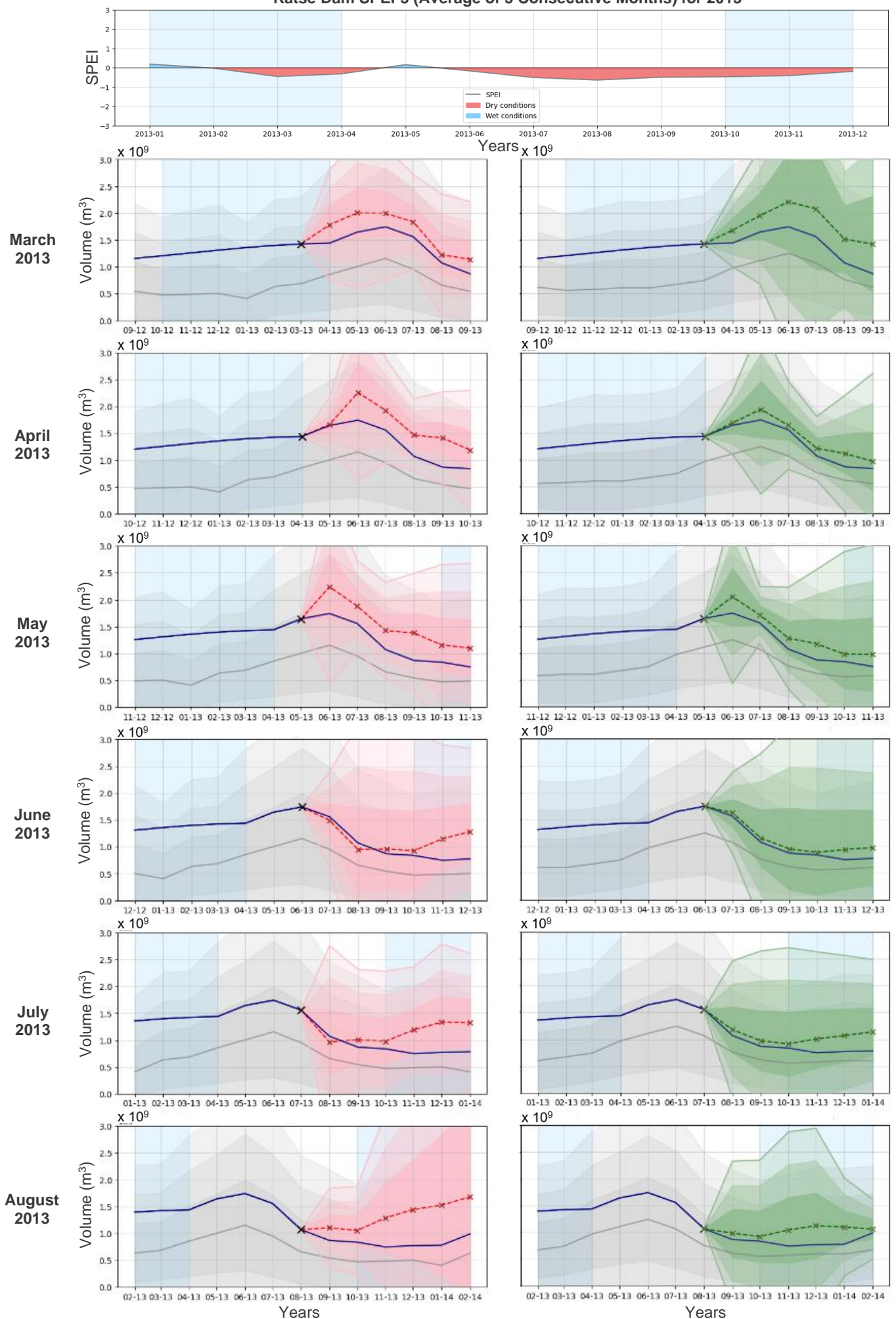
Figure 4.34: The volume predictions for Kaste Dam moving through different starting months (please read from top to bottom), accompanied by the SPEI (-) time series. Each prediction contains 6 months lead time starting from each month between March and August 2013 using volume (autoregression) and SPEI-3 & volume (Multi-linear regression).

The findings reveal that the correlation coefficients between the two variables remain below 0.3, indicating a weak correlation. Nonetheless, up to four preceding months can be utilised by the regression as, demonstrated by the 95% confidence interval. In the V-SPEI-3$_{MLR}$ (the multi-linear regression model with volume and the SPEI-3 as predictors) for Katse Dam three values are used.

The results of the V-SPEI-3$_{MLR}$ (green) and V$_{auto}$ (red) models for Katse Dam for the months of March to October are presented Figure 4.34, accompanied by the SPEI-3 series on the top of the figure. Concurrently, the SPEI-3 time series indicate relatively mild wet and dry conditions during the previous wet season, with SPEI values dipping as low as maximum -0.8 during the subsequent dry season. The Figure shows that the volume in the Katse dam remains comparatively high relative to seasonal expectations, something that is explored in further detail in Section 5.7. Notably, the V-SPEI-3$_{MLR}$ (green) model demonstrates slightly superior predictive accuracy compared to V$_{auto}$ (red), an observation that is elaborated upon in Section 5.6.

The HSS scores for V-SPEI-3$_{MLR}$ (green) are presented in Figure 4.35 and is found to be relatively similar to V$_{auto}$ (red). It should be noted that a lower threshold is selected for Katse dam compared to Hawane dam, as the former does not exceed the -1 standard deviation threshold often enough to compute the HSS. Moreover, the HSS scores indicate that both models perform well in predicting deviations of - 0.5 standard deviation below the seasonality. The predictive performance of V-SPEI-3$_{MLR}$ diminishes beyond a three-month lead time, with predictions for the months of April, May, and June displaying considerably reduced accuracy. These findings are further discussed in Section 5.5.
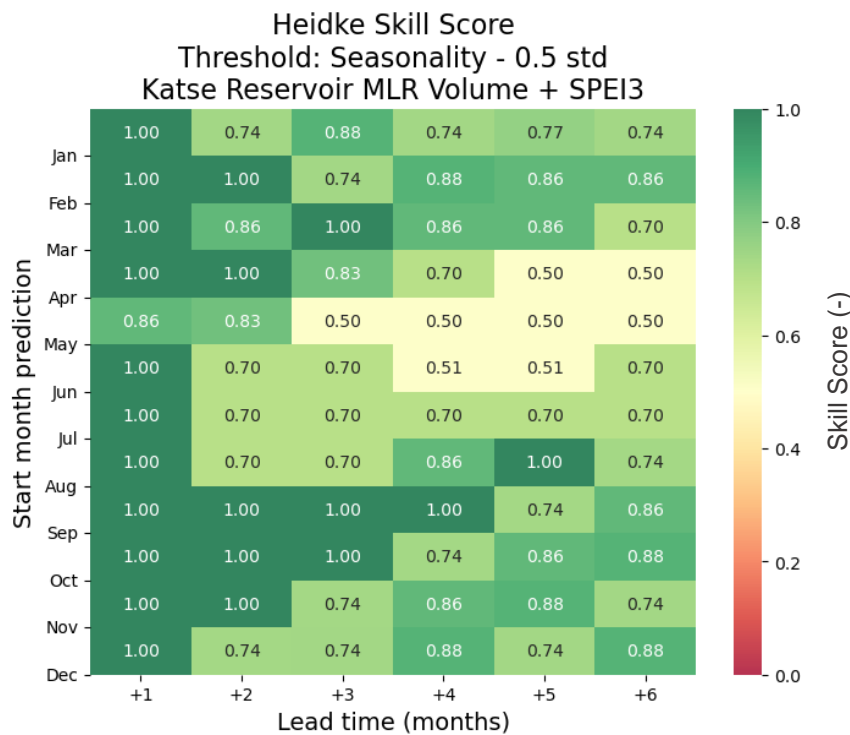
Figure 4.35: The performance of V-SPEI$_{MLR}$ model in the Katse Dam predicting whether the true values deviate from the seasonality by 0.5 standard deviation in the Katse Dam is presented using the Heidke Skill Score (HSS), as computed by Formula 2.8. The HSS scores are color-coded to indicate performance, with green indicating good performance and red indicating poor performance. The associated HSS values are also presented, with a score of 1 indicating good performance and a score of 0 indicating poor performance. The y-axis displays the starting month for each prediction, while the x-axis represents the lead time up to which the prediction is made.

5

Discussion

This chapter focuses on the evaluation of the proposed method for predicting water availability and reconstructing reservoir bathymetries. The novel approach for bathymetry reconstruction is discussed in Section 5.1, followed by a detailed description of the validation results in Section 5.2. Section 5.3 covers a discussion of the comparison of the proposed method to Messager et al. (2016). The predictors used in the regression models are discussed in Section 5.4, while the different regression models are elaborated on in Section 5.5. Section 5.6 highlights the correlation between the SPEI and volume, while Section 5.7 is dedicated to the discussion of the usability of the model, based on interviews conducted by Red Cross 510 in parallel to this research.

5.1 The Novel Method for Bathymetry Reconstruction

This study's findings indicate that the developed methodology has potential for accurately reconstructing hypsometry in both Zambian and Indian reservoirs. The Mita Hills and Mulungushi reservoirs in Zambia demonstrated significant accuracy (with relative errors of 0.88 and 1.01, respectively). While some reservoirs in the Indian validation dataset showed excellent results, others did not perform as well or did not allow for bathymetry reconstruction at all. The expectation was that the Zambian reservoirs would perform better, partially because they were used as examples during the development of the method, which helped to identify and resolve any errors that emerged. However, for the large Indian dataset, new errors emerged and due to time limitations, it was not feasible to address all of them. Additionally, the better performance of the Zambian reservoirs may have been partly since the reference data provided a hypsometric curve, obviating the need to convert the reservoir bathymetry into volume time series for validation. This saved an additional step, which could have introduced more uncertainty in the validation process.

Nevertheless, the challenges in the Indian reservoirs were mainly related to delineating the reservoirs. In total, 46 out of 94 reservoirs had bathymetry plots that had issues to indicate the upstream and downstream cells, like in the examples presented in Figure 4.11. This could be cause by, for example, wrongly sampling the nearest upstream cell in the reservoir. In the pre-processing, the reservoir is delineated by a shape, referred to as a 'polygon', that is extracted from Global Water Watch. However, if the polygon fails to accurately represent the shape of the reservoir or if the georeferenced data of the polygon is inconsistent, it is likely that the upstream cell will be sampled incorrectly. This will cause inaccuracies in the delineation of the reservoir.

Another potential explanation is that the digital elevation model may have wrongly indicated the location or absence of the dam. This could occur if the slope in the digital model is inaccurately calculated and not properly sampled to the main stream, resulting in incorrect sampling of the downstream cell during the delineation process. Incorrectly selected downstream cells often lead to over-prediction of the bathymetry, as they are frequently sampled lower than the actual bottom of the reservoir. Moreover, even if the dam location is accurately identified, the downstream cell may still be incorrectly sampled. This could be due to the buffer size being too large in the method. To address this issue, a possible solution is to manually adjust the buffer distance beyond the default 500 meters, by providing a new distance from the most downstream point.

Overall, to account for the errors in delineation of the upstream and downstream cell it is recommended to manually assign the upstream and downstream locations. The delineation is especially important as it is a fundamental step in retrieving the entire bathymetry of the reservoir. Especially the downstream cell should be sampled correctly, as impacts due to incorrect sampling shown to be larger than in an upstream cell, as can also be deduced from Figure 4.11. Some of the delineation challenges were already addressed at the time of writing, however prospects for even further enhancement of this algorithmic component in future iterations are worth considering.

The Indian dataset contains several reservoirs that have complex shapes, including those with multiple large tributaries or merging reservoirs. In this study, the bathymetry of such reservoirs was determined by identifying tributary streams (Figure 3.2: *Step 5*) within the reservoir that possess a Strahler order deviating by up to five from the Strahler order observed in the first stream (Figure 3.2: *Step 3*). It is noteworthy that not every part of these reservoirs is considered in the interpolation (Figure 3.2: *Step 6*), as evident from Figure 3.2. The remote tributaries of a reservoir are subject to an interpolation that solely employs the surrounding terrain elevation, as no bathymetric data is accessible in their vicinity. Consequently, the resulting volumes of these reservoirs are likely to be underestimated. When computing complex shapes, using a deviation lower than five from the Strahler order in the first stream is not recommended for reservoirs in the applied dataset. Conversely, higher deviations are advisable, although this may result in longer computational time. Determining the optimal deviation from the Strahler order depends on the user's requirements, and various strategies could be explored in future research.

One of the complex reservoir shapes observed consist out of two different river branches that only convolute at the reservoir dam. Apart from the convolution point, the two parts are completely disconnected which makes it challenging for the algorithm. If either the Strahler order setting is set too low, or the flow direction is calculated wrongly, one of the two branches will not be taken along in the volume calculations, leading to an incorrect volume estimation.

Other difficult reservoirs were once that cascades, which were 12 out of 94 reservoirs in the Indian dataset, among which the Ban Sager, Malampuzha, and Srisailam reservoirs, which were presented in Figure 4.12. For these reservoirs, the algorithm had difficulty determining the exact location for the start and end of the reservoir bathymetry because the actual reservoir surface was not clearly identified. Therefore, manual location information was required. One potential reason for the cascading effect was the algorithm's assignment of surrounding cells as reservoirs. Additionally, structures in the water, such as dams or cascades, may cause elevation shifts in the main stream.

It was also assumed that larger reservoirs are more sensitive to errors in the model, which is understandable because a small offset in the surface water area observation in the higher water levels is results in significant larger changes in volume then in the lower water levels. However, on the contrary, the estimation of reservoir bathymetry tends to be more precise in the higher ranges of the reservoirs due to the smaller distance to the known terrain. Figures 4.21 and 4.22 presented that the latter prevails and that better performances are found in the higher ranges of the reservoirs.

Last, it should be noted that the digital elevation model used in this study was measured at a single point in time, and is therefore a static DEM. Specifically, the MERIT-Hydro DEM was constructed around December 2017, which means that the DEM contains the full bathymetry of reservoirs constructed after the establishment of the DEM. However, for reservoirs constructed after the establishment of the DEM, the algorithm will fail as the dam wall was not present at the time of measurement. It is recommended to further develop the algorithm so that this is recognised by the model. Especially because for such reservoirs, a real precise bathymetry can be measured, as simply there is no need for interpolation as the entire bathymetry is available in the DEM.

5.2 Validation of the Hypsometric Curve

The validation dataset of Indian reservoirs entailed several instances where a shift in local datum occurred across the series for different reservoirs. This shift in elevation could be attributed to a variety of reasons, such as a modification of the local datum, which often is the minimum operating capacity, or the relocation of the local measurement installations to different elevations. Additionally, the introduction of a systematic shift during post-processing could also contribute to a shift in local datum. Due to the variations in local datum changes across reservoirs, the analysis focused on the 500 most recent measurements for each reservoir. Nevertheless, for some reservoirs, the validation dataset displayed a significant number of outliers, leading to overprediction if the outlier values were greater than the mean of the dataset, and underestimation if they were smaller than the mean. Figure 4.24 provides an example of a reservoir where the filtering of outliers was unsuccessful.

If the local datum in the validation dataset remains unknown, this leads to a systematic error between the validation and modelled results. The systematic error denotes the difference between the local datum and the modelled outcomes. To address this issue for the aggregated group of reservoirs, a correction was implemented. This study employed a correction that computed the mean water level in the modelled results and the validation data and adjusted for the difference found in the mean. However, the correction was not always effective in eliminating the entire offset in certain reservoirs, as presented in Figure 4.24. This outcome is likely attributed to the outliers detected in the dataset, which significantly influenced the validation mean. Hence, in some cases, an offset is still evident after correction. An alternative correction method could involve calibration using known water surface areas, specifically when the reservoir is empty, although this approach requires availability of relevant information. Apart from the offset observed in some of the reservoirs, mostly overestimating the results, the overall performance of the bathymetry and hypsometry estimates seemed to correctly estimate the validation data.

In the quantitative analysis, a comparison was made among reservoirs based on the percentage of fillings concerning their maximum capacity. However, it is probable that for certain reservoirs, the actual maximum capacity was not reflected in the 500 measurements obtained from the validation dataset. This outcome could be due to the measurements being taken coincidentally during a period when the water level in the reservoir was relatively low, resulting in classification of these reservoirs as smaller than their actual size. Nonetheless, it is inevitable to consider the data available for this study.

The evaluation of the model's performance in estimating reservoir volume in India for various filling states reveals that the modelled volumes still exhibit considerable water volume in the reservoir at a filling state of 25%, whereas the validated volumes indicate no such volume. It should be noted that this disparity is likely to be that the local datum has been established as the minimum operating capacity of the reservoir, which, in many instances, corresponds to 25%.

It is noteworthy that in addition to the two waterbody categories of natural lakes and reservoirs, there may exist other types as well. For instance, a dam can be constructed on a river that flows out of a natural lake, transforming the natural lake into a man-made reservoir. Nevertheless, the bottom parts of the reservoir may retain the natural lake's morphology, while the upper parts reflect a man-made reservoir. In this scenario, the model's estimation of lake volume for such reservoirs would be underestimated since the storage below the dam wall would not be accounted for.

Finally, the validation process relies on the use of existing reference datasets, which, particularly when bathymetric data is available, is the optimal way to test the method. However, in many cases, such reference data is not accessible. To overcome this challenge, one possible solution could be to create artificial reservoirs in a digital elevation model (DEM) by simulating dam walls and water levels. By doing so, the entire bathymetry can be generated for validation purposes for multiple examples. An essential prerequisite for this approach is that the artificial reservoir must be constructed in a location that is feasible and realistic.

5.3 Comparison to Static DEM-based Method by Messager et al. (2016)

As anticipated, the novel method is exhibiting increased performance when compared to the bathymetry reconstructions proposed by Messager et al. (2016), as illustrated in Figure 4.20. This outcome can be attributed to several factors, foremost among them is that a tailor-made novel method was developed for man-made reservoirs, in contrast to the focus of Messager et al. (2016) on both man-made reservoirs and natural lakes. Characteristics of our tailor-made model, as compared to the method of Messager et al. (2016) are the location and elevation of the dam wall. Also, it was assumed that the flattening in the bottom of the reservoir tends towards the dam wall, while Messager et al. (2016) assumes the deepest point to be at the centre of the reservoir, which is typically the case for natural lakes (Morris & Fan, 1998). This enabled more accurate volume estimations for man-made reservoirs.

As previously discussed in Section 2.6, another significant difference between the two methods is that Messager et al. (2016) utilised the same slope parameter k for all reservoirs in their analysis, while the novel approach determines a slope parameter for each individual reservoir. This approach enables the novel method to tailor the methodology to each specific reservoir, thereby successfully enhancing the accuracy of the model as presented in Figure 4.27.

5.4 Predictor Time Series around The 2025-2016 Drought

Time series of the predictors volume, precipitation and SPEI in the Hawane reservoir are presented in Figure 4.29. A prominent feature within the volume time series is the large decrease in water volume in January and October in 2016. This is the period during which the ongoing drought impacted the water level in the Hawane reservoir, which dropped to 9% (ESG News Eswatini, 2016). These extreme circumstances are also characterised by the other predictors: a decrease of 1 standard deviation in precipitation and extreme dry conditions with SPEI values ranging from -1 to -3. Overall, all predictors considered provide a clear description the drought that started in the beginning of 2015, and prolonged till May 2016.

Moreover, it is noteworthy that the reservoir volumes in the Hawane reservoir in the period preceding the 2015-2016 drought event remained relatively stable compared to the subsequent period, whereas precipitation or SPEI patterns align with seasonality. Notably, the Hawane reservoir showed deviations from the constant patterns primarily during the wet seasons, as evident in the years 2004-2005, 2008-2009, 2023-2014, and 2019-2020. The variation in volumes observed in the Hawane dam can potentially be explained by the dam's operating policy. Prior to the 2015-2016 drought event, the dam may have been operated at a constant level, with any excess precipitation and runoff being released or spilled in equal volume. However, this approach may not have been feasible during the drought years of 2004 and 2011, as indicated by the significantly low SPEI values during those periods. This could potentially explain the decreased volumes observed in July 2005 and July 2012. Following the 2015-2016 drought event, the hypothesis is that dam operations were altered to actively use the water in the reservoir, potentially driving the seasonal patterns observed. However, this hypothesis could not be validated within the scope of this thesis. A motivation for change in operating strategy could include factors such as economic development or urban expansion, or as a responsive action to the drought. However, to substantiate these assumptions, further research is needed on the social and water management strategies in place during those drought periods. Additionally, it is possible that the observed changes in volumes could also be attributed to the installation of additional extraction facilities in response to the drought.

5.5 April Predictions Compared: Before and After the 2015-2016 Drought

Predictions to water availability were done with various regression models. In Figure 4.27, there was examined a prediction that started at the end of the wet season in April 2015, which is the wet season before the 2015-2016 drought. During the wet season, there was a moderate amount of precipitation, with observations falling within one standard deviation of the seasonal mean. The SPEI indicates that, after the 2014-2015 wet season, extreme dry conditions occurred relative to the long-term average trend during this period, with values dropping to as low as -3. However, precipitation did not deviate from the seasonal trend, neither did the volume time series. Non-precipitation variables, such as daily temperature or the heat index, used in calculating evapotranspiration might be responsible for the extreme SPEI values during this period. High temperatures in April can result in negative SPEI values, but it has no direct impact on the reservoir's water volume. The impact of high temperatures is indirect, leading to an increase in evapotranspiration, ultimately resulting in a greater water demand in the long run. For instance, crops may require irrigation during periods of heightened evapotranspiration, or water could be utilised for cooling purposes. Although no direct effects on the volume time series are observed, the SPEI exhibits extreme dry conditions, which suggests that non-precipitation variables used in SPEI calculations are contributing to the extreme values during the specific period under consideration.

In analysing the regression models presented in Figure 4.28, an interesting observation is that the V-$SPEI_{MLR}$ and $SPEI_{MLR}$ models do not respond to the extreme values in the SPEI time series for the first four months, despite the dry conditions indicated by the predictor. It can be inferred from this that when input variables are close to the mean in the training dataset, predictions tend to move towards the seasonal expected trend. Therefore, although the SPEI values we observe may be significantly negative, they provide us with the mean in the training dataset and hence do not add much predictive value. This also explains why the V-P_{MLR} and V_{auto} exhibit similar values in the first four months in Figure 4.29, as both inputs for the volume time series and precipitation time series do not deviate from their seasonal expectations. Consequently, small weights are calculated in the regression model, and the model instructs the prediction to follow the seasonal trend. However, this can pose a limitation when volumes do not conform to their seasonal trends, which is a potential issue when using regression models.

Figure 4.28 examines the April prediction for one year later, in April 2016. Similar regression weights are used for the predictions, as is typical for a regression model, but the inputs have changed. The wet season had already ended, and during the 2015-2016 drought, the observed amount of precipitation did not align with seasonal expectations. This is evident in the precipitation time series, which deviated from the seasonal mean by one standard deviation for the entire season. Additionally, the SPEI indicated extreme dry conditions for almost the entire season, observing the drought event. The magnitude of precipitation was not similar to that of the volume time series. This can be attributed to the fact that the precipitation that fell in the upstream catchment may not have reached the reservoir, particularly if the lands upstream were already dry, as the water is most likely absorbed by the unsaturated soil. Another explanation could be that the period of drought induced additional extractions from the reservoir, causing the volume to deviate more significantly than the precipitation time series. Notably, the volume time series showed a deviation of more than three standard deviations from normal, indicating a significant drop in reservoir levels during the drought. However, the regression models did not fully capture this deviation, indicating a limitation in their ability to predict such extreme events.

The regression models, P_{MLR} and $SPEI_{MLR}$, presented in Figure 4.29 are unable to capture a decrease in volume, and instead revert directly to the seasonal mean. This outcome is consistent with the anticipated behaviour of the regression model and once again highlights the limitations of the model. Notably, the volume time series exert a significant influence on the variation observed in the other regression models. This is attributable to the substantial reduction in volume from seasonality, a magnitude which neither precipitation nor SPEI can match. In comparison to the mean observed in the training dataset, precipitation and SPEI exhibit minimal deviation, and consequently, return little deviation from the seasonal mean. This limitation is in line with the discussion on the restrictions of

the regression model presented earlier and is something that is likely to overcome in for example a physically based model.

In the P_{MLR} and $SPEI_{MLR}$ models, which consider precipitation and SPEI as a predictor only, an unexpected finding is the presence of a relatively constant confidence interval, which differs from the other models. This phenomenon may be explained by the independence of the predicted values, whereby the m+2 value is computed in its own distinct way, regardless of what was predicted in m+1. This attribute is characteristic of the linear multiple regression model and implies that it is not predetermined that uncertainty ranges will increase in future predictions, like one would expect with predictions. The uncertainty in the predicted values is determined by the white noise in the regression model, which is reliant on the variance in the training dataset. This leads for example to uncertainty ranges of predictions in the wet season to be large, as the training dataset contains larger variance during those periods. Also, this is the cause for the varying uncertainty ranges which like previously presented in August 2015 in Figure 4.30.

Some anomalous outliers are observed in the predictions, as illustrated in Figure 4.31 for $V\text{-}SPEI_{MLR}$, whereby the model abruptly overpredicts the true value with a lead time of 6 months. This outcome is feasible in the linear regression model, where the set of weights exhibits a high intercept resulting from the optimization fit, and typically, is rectified by negative weights for one of the volume inputs. However, during the year 2016, the volume input is remarkably low, which leads to a minor correction of the intercept. This exemplifies a situation where the set of weights obtained from the optimization fit is inadequate for prediction purposes.

Although the absolute performance of the $SPEI_{MLR}$, which only uses SPEI as a predictor, is weak according to its HSS scores, it does exhibit a slight increase in skill at the end of the rainy season, and the end of the dry season. It shows that the predictor gains skill when all input variables are within either the dry or wet period, suggesting that the SPEI during these periods is consistently indicative across years. However, the HSS score decreases as soon as the seasons are alternating (April and November/December), indicating that the SPEI varies from year to year during these periods. This agrees with the reasonable assumption that the beginning of the wet and dry seasons may differ by a few weeks from year to year.

To conclude, the assumption was that the $V\text{-}P_{MLR}$ model would provide better predictability during relatively dry periods compared to the V_{auto} model. However, when examining both models for the wet season ending in April 2015 (Figure 4.27) and the very dry one in April 2016 (Figure 4.28), there was no significant difference in predictability between the two models. Furthermore, the HSS scores of the two models, which are provided in Appendix F, did not indicate any significant added value for $V\text{-}P_{MLR}$. A possible explanation for this is that the deviations observed in the precipitation time series were too small for the regression model to effectively utilise. Even during the most extreme year of the drought in 2015-2016, the precipitation deviated only one standard deviation from seasonality, leading the regression model to heavily rely on the seasonal trend. This highlights a limitation of using data-driven models, and it would be advisable to develop a physical model of a guided data-driven approach, including in-situ measurements, for a more detailed modelling of the water volume.

It is apparent that all models predict an increase in reservoir volume two months after the official start of the rainy season. This observation could be explained by various factors, including the possibility that there is generally a lag time of around two months in the catchment. This lag time may be due to dry soils upstream in the catchment that need to become saturated before precipitation can turn into runoff. Alternatively, it may be that water extraction from the reservoir during the initial months of the rainy season is like the inflow, and only after two months does the extraction decrease or the inflow increase. To find the exact cause, additional research will be needed to the catchment or the extraction patterns in the reservoir.

The second conclusion drawn from the analysis is that the $V\text{-}SPEI_{MLR}$ model yields the best results for volume predictions, as evidenced by the predictions displayed in Figure 4.29 and the HSS score analysis presented in Figure 4.30. Interestingly, the lack of correlation between the lagged SPEI values and the volume of the Hawane reservoir in the corresponding month is surprising given the

model's relatively good performance. Therefore, it might be possible that this lack of correlation is due to other factors, such as the significant variation in volumes present in the training dataset.

The analysis shows that the performance of the V-SPEI$_{MLR}$, V$_{AUTO}$, and V-P$_{MLR}$ models is significantly better than that of the SPEI$_{MLR}$ and P$_{MLR}$ models, which exhibit little to no predictive skill. This suggests that when using a data-driven approach to predict reservoir volume time series, it is crucial to account for the memory in the reservoir volume dynamics. As such, the novel method presented in this thesis can be a valuable tool for this purpose.

It is important to note that the threshold used to predict the HSS scores in this analysis was a decrease in water volumes of 1 standard deviation. However, for proper decision-making related to water availability, it is necessary to work with thresholds that are relevant to stakeholders. Unfortunately, due to time limitations, this was not feasible for this thesis. It is expected that using more extreme thresholds will result in lower skill scores, as the model's ability to predict such events may be worse due to their infrequency in the training series.

Furthermore, the SPEI is assumed to be a useful indicator of the wet and dry conditions in the region, with the demand for water assumed to be higher during dry conditions. Thus, the SPEI can indirectly reflect water availability. It would be intriguing to investigate whether this assumption holds by including the extraction or discharge time series of the reservoir in the prediction models. However, due to time constraints, this was not feasible within the scope of this master's thesis.

5.6 SPEI: Lacking Correlation, Good Predictor

It was hypothesised that the V-SPEI$_{MLR}$ model would improve predictability compared to the V$_{auto}$ and V-P$_{MLR}$ models, despite the absence of cross-correlation between the lagged-SPEI and volume in the respective month. The SPEI index compares precipitation and potential evapotranspiration, thus contains information that is applicable to both wet and dry seasons. Therefore, the V-SPEI$_{MLR}$ model would provide superior predictability relative to the V-P$_{MLR}$ model, which only incorporates precipitation, and the V$_{auto}$ model, which relies solely on autoregression. While the V-SPEI$_{MLR}$ model demonstrated improved predictability, it was hypothesised that the absence of cross-correlation between the lagged-SPEI and volume in the respective month may be attributed to the absence of variability in the training dataset. Specifically, the training dataset for the Hawane reservoir, which comprises the complete time series apart from the years affected by the 2015-2016 drought event, predominantly represents a constant volume variable. In contrast, the SPEI series exhibits considerable variance.

To test the theory that the lack of correlation between the lagged SPEI time series and the volume in the respective month is due to the relatively constant time series in the training dataset, the Katse dam, which exhibits more fluctuations in its volume time series, was analysed. In the alignment of the time series in Figure 4.32, it was observed that the monthly SPEI contained significantly more positive and negative peaks than the volume time series of the Katse dam. As expected, this led to no improvement in the correlation between the monthly SPEI and volume. Conversely, the 3 monthly SPEI (SPEI-3) exhibited a relatively similar pattern of fluctuations around the reservoir, and demonstrated increased correlation towards the respective month, as presented in Figure 4.33.

The enhanced correlation between SPEI-3 and volume implies that the direct influence of precipitation and evaporation on the reservoir volume is relatively low. Such direct impacts primarily relate to the replenishing and evaporation of water within the reservoir. Conversely, indirect impacts tend to be more diffuse and may not be directly observable. For instance, after a precipitation event in the upstream catchment, it might take a while before any noticeable effects on the water surface are detected. This lag varies across different catchments and depends on a range of factors, including soil saturation, soil type, topography, rainfall intensity and duration, the presence of vegetation, and urbanization, among others. These indirect impacts could potentially be the reason why the correlation between SPEI-3 and volume is stronger than that observed between monthly SPEI and volume.

5.7 Usability of the Novel Method and the Volume Predictions

The usability of the novel method and the volume predictions depend heavily on the specific needs and requirements of decision makers, which can vary widely. To better understand these needs and requirements, Red Cross 510 conducted a study that included human-centred design interviews with water management stakeholders in Lesotho, including the Water and Sewerage Company (WASCO), the Disaster Management Agency (DMA), the Lesotho Highlands Water Project (LHDA), the Ministry of Water and the Lesotho Meteorological Services (LMS) (Red Cross 510, 2023). During these interviews, stakeholders were asked about the potential benefits of volume estimations and how they would use the Global Water Watch platform, as well as any additional requirements they might have. This information can help ensure that the platform meets the specific needs of decision makers and is useful in real-world applications.

First of all, it is important to note that the rural areas in Lesotho mainly rely on water resources other than the reservoirs included in the Global Water Watch database, such as smaller reservoirs, streams, or groundwater wells. Unfortunately, these sources could not be measured by Global Water Watch or computed with the novel method. However, challenges still exist in operating the larger reservoirs, which play a significant role in generating economic income for the country. As such, these reservoirs are closely monitored through in-situ measurements of water availability and reservoir bathymetry. In cases where in-situ measurements are unavailable due to logistical reasons, remotely sensed volume estimations could help fill gaps in the time series.

In addition, accurately estimating the sedimentation rate in reservoirs remains a complex task. The novel method includes a theoretical slope parameter for each reservoir, which flattens the reservoir bottom towards the dam wall to account for sedimentation. However, the current results of the method provide a volume time series proxy only for reservoirs with the typical man-made shape discussed in Section 2.1. To improve the accuracy of volume estimations, a hybrid approach that incorporates sedimentation point measurements in specific reservoirs could be beneficial. The measurement points from bathymetric surveys can enhance the bathymetry estimates in reservoirs. This would enable a more precise calculation of volume by accounting for any sedimentation occurring in the reservoir.

Another potential application of the volume estimations from Global Water Watch is to conduct a historical analysis of water volumes in reservoirs during periods when the same outlook was presented. This analysis could reveal how and to what extend reservoirs were affected in history, and what the impacts on society are. The projection of the historic situation on the current situation will provide decision-makers information on what strategy to take in mitigating the impacts of the event.

The volume estimations derived from Global Water Watch can also be utilised for conducting a historical analysis of water volumes in reservoirs during periods when the same outlook was presented. This analysis can provide insights into how reservoirs were affected and the extent of the impacts on society in the past. By projecting the historic situation onto the current situation, new information could be revealed to decision-makers which could be useful for developing more effective and efficient response plans.

Furthermore, the use of remotely sensed data for water monitoring also provides the benefit of being able to automate the monitoring system and link it to an automated warning system that can be set up to send alerts or notifications to specific stakeholders. By automating the system, alerts could be sent out without the need for manual intervention, which can save time and resources.

Last, the accuracy and frequency of remotely sensed volume estimations are crucial for their usability in reservoir management. Reservoir operators may require near-real-time updates at an hourly frequency to make informed decisions, while other stakeholders, such as policymakers, may benefit from less frequent updates with a much larger frequency. The required levels of accuracy and frequency varies for each stakeholder, which is something to investigate in further research.

6

Conclusions & Recommendations

The final chapter of this thesis presents a summary of the key findings, contributions, limitations, and recommendations for future research. It provides an overview of the study's significance and highlights the fundamental progress made towards predicting water availability in reservoirs worldwide.

6.1 Towards Water Availability Predictions in Reservoirs Worldwide

In conclusion, this thesis presents a novel method for retrieving near real-time volume time series in small to medium-sized man-made reservoirs worldwide using remotely sensed open data. The method combines various data sources and techniques to reconstruct the bathymetry of a reservoir and convert available reservoir area time series into volume time series. The method involves a step-by-step approach including the delineation of the reservoir using the model generation tool HydroMT by Eilander et al. (2023), surface filtering, stream identification based on D8 flow direction methods in PyFlwDir also by Eilander et al. (2023), depth determination of the main and tributary streams, and subsequent bathymetric interpolation. The resulting bathymetry of the main stream was observed to closely align with the upstream terrain and gradually flatten towards the downstream dam wall. The volume time series are then used to predict water availability up to six months in advance using regression models that incorporate precipitation data and the Standardised Precipitation and Evaporation Index (SPEI).

The results of the study demonstrate the potential of this novel approach in accurately estimating reservoir volumes and predicting water availability. The method successfully obtained bathymetries and accurate volume estimations when validating using 2 reservoirs in Zambia and 48 in India. However, some reservoirs with complex shapes faced initial delineation challenges, resulting in inaccurate volume predictions. These issues could be resolved by manually delineating the area for bathymetry reconstruction. Moreover, regression models were applied to case study reservoirs in Eswatini and Lesotho, demonstrating reasonable predictive capabilities with the Heidke Skill Scores ranging from 0.77 to 1 for up to 2 months ahead.

The key contributions of this study are three-fold. First, the novel method introduced in this thesis provides an improved methodology to estimating volume time series based on remotely sensed data. This novel method stems from an improved approach in deriving reservoir bathymetry. Second, this thesis argues that including the volume time series' memory when predicting the volume time series significantly improves the model's predictive capabilities. This was verified through iterations of volume time series predictions with several predictors, which include volume time series memory, SPEI, and precipitation time series data. Lastly, the study explored the added skill when incorporating a combination of predictors. The conclusions derived from these experiments yielded that the combination of SPEI and volume time series' memory demonstrated the best predictive capacities, whereas precipitation data did not significantly improve the accuracy of volume predictions.

Despite the success of the novel approach in predicting water availability, there are some limitations to the study that need to be addressed in future research. First, the method is to a lesser extend suitable for reservoirs with highly irregular shapes, and these reservoirs require further manual delineation. Considering the method relies on accurate bathymetry reconstruction, inaccuracies in bathymetry reconstruction directly impact volume predictive capabilities. Second, the study only

considers small to medium-sized man-made reservoirs and cannot be applied to large-scale reservoirs. Finally, considering sufficient training data is required to train the prediction models, representative data is not always available for reservoirs. For example, historical operating schemes of the reservoir can vary significantly when compared to current ones, which results in unrepresentable training data.

It is recommended that future research is conducted to explore additional factors that impact the accuracy of the methodology of the reservoir bathymetry reconstruction. This can be done by solving for delineating errors and by testing the methodology outside of the regions investigated in this thesis, namely India and Zambia. In this thesis, consideration of in-reservoir processes such as reservoir sedimentation were not included in the scope of the research. For future improvements, it is recommended to research the impact of these processes on the construction of the reservoir bathymetry further.

Second, it is recommended to explore the added benefit of in-situ bathymetric measurements to the model. By using in-situ measurements for specific points within the reservoir, they can be integrated with the reconstructed bathymetry to enhance the accuracy of volume estimations. This approach would provide a more comprehensive understanding of the sedimentation processes taking place within the reservoir and enable more precise calculations of volume. Therefore, the combination of in-situ measurements and reconstructed bathymetry has the potential to significantly improve the accuracy of volume estimations.

Third, future research can be done to ensure the transferability of the method across different regions, which is crucial for applicability to any reservoir worldwide within the Global Water Watch dataset. To ensure transferability, investigation must be conducted into optimising the model's transferable parameters specific to different regions. In the prediction models, it is possible to utilise predictors that are commonly used in specific regions. The only requirement is that sufficient time series data is available, and any relevant predictor can be utilised.

Finally, when considering the usability of the novel method, future research is recommended to determine the volume thresholds for reservoirs to trigger anticipatory action. Decision makers desire a clear action plan when these thresholds are predicted, but more importantly demand a measure of certainty for these predictions. Additionally, further exploration is required to understand the most effective communication strategies for triggers to the relevant stakeholders.

In conclusion, the method presented in this thesis successfully provided remotely sensed volume estimations in small to medium-sized man-made reservoirs and it has the potential for applications worldwide. The study highlighted the novel method for bathymetry reconstruction and explored the skill of regression models in predicting water availability. Future research can build on the foundations laid in this study towards the development of more accurate and reliable volume estimations and predictions in various reservoirs worldwide.

Bibliography

Alsdorf, D., Birkett, C., Dunne, T., Melack, J., & Hess, L. (2001). Water Level Changes n a Lareg Amazon Lake Measured with Spaceborne Radar Interferometry and Altimetry. *Geophysical Research Letters, 28*(14), 2671-2674.

Annor, F., Van de Giesen, N., Liebe, J., Van de Zaag, P., Tiltmant, A., & Odai, S. (2009). Delineation of small reservoirs using radar imagery in a semi-arid environment: A case study in the upper east region of Ghana. *Physics and Chemistry of the Earth, Parts A/B/C, 34*(4-5), 309-315.

Arsen, A., Crétaux, J., Berge-Nguyen, M., & Abarca Del Rio, R. (2014). Remote Sensing-Derived Bathymetry of Lake Poopó. *Remote Sensing, 6*(1), 407-420. doi:10.3390/rs6010407

AZ Nations. (2017). *Population of Mbabane 2017*. Retrieved from World countries population: https://www.aznations.com/population/sz/cities/mbabane

Becker, J., Sandwell, D., Smith, W., Braud, J., Binder, B., Depner, J., . . . Weatherall, P. (2009). Global Bathymetry and Elevation Data at 30 Arc Seconds Resolution: SRTM30_PLUS. *Marine Geodesy*, 355-371.

Beguería, S., Latorre, B., Reig, F., & Vicente-Serrano, S. (2021). *Global SPEI database.* Open Database License.

Biancamaria, S., Lettenmaier, D., & Pavelsky, T. (2016). The SWOT mission and its capabilities for land hydrology. *Remote Sensing and Water Resources*, 117-147.

Bierkens, M., Bell, V., Burek, P., Chaney, N., Condon, L., David, C., . . . Wood, E. (2015). Hyper-resolution global hydrological modelling: what is next? "Everywhere and local relevant". *Hydrological processes, 29*, 310-320. doi:10.1002/hyp.10391

Blog, J. Z. (2013, December 28). *One time we went to Mulungushi*. Retrieved from juliezambia.blogspot.com: http://juliezambia.blogspot.com/2013/12/one-time-we-went-to-mulungushi.html

Brownlee, J. (2017, January 2). *Autoregression Models for Time Series Forecasting With Python*. Retrieved from Machine Learning Mastery: https://machinelearningmastery.com/autoregression-models-time-series-forecasting-python/

Buarque, D., Fan, E., A.R., P., & Collischonn, W. (2015). Comparacao de métodos para definir direcões de escoamento a partir de modelos digitais de elevacão. *RBRH: revista brasileira de recursos hídricos*, 91-103.

Burgan, H. (2016). *Autoregressive Models For Prediction of Rainfall Data in Afyon Region.* Istanbul: International Science.

Chandimala, J., & Zubair, L. (2007). Predictability of stream flow and rainfall based on ENSO for water resources management in Sri Lanka. *Journal of Hydrology*, 303-312.

Chen, J., & Boccelli, D. (2014). Demand Forecasting for Water Distribution Systems. *Procedia Engineering*, 339-342.

Cohen, B. (2015). *Photographs of Katse Dam*. Retrieved from The Gate: https://thegatewithbriancohen.com/katse-dam-in-lesotho/

Cooley, S., Ryan, J., & Smith, L. (2021). Human alteration of global surface water storage variability. *Nature, 591*, 78-81.

CWC. (n.d.). *Validation dataset.* New Delhi: Central Water Authority.

Dargahi, B. (2012). Reservoir Sedimentation. In R. H. L. Bengtsson, *Encyclopedia of Lakes and Reservoirs* (pp. 628-649). Springer Science+Business.

Deputy Prime Minister's Office. (2016). *Swaziland Drought Assessment Report: Rapid Assessment 2015/2015 Season.* Deputy Prime Minister's Office.

Dibike, Y., Prowse, T., Bonsal, B., & O'Neil, H. (2016). Implications of future climate on water availability in the western Canadian river basins. *International Journal of Climatology*, 3247-3263.

Donchyts, G., Winsemius, H., Baart, F., Dahm, R., Schellekens, J., Gorelick, N., . . . Schmeier, S. (2022). High-resolution surface water dynamics in Earth's small and medium-sized reservoirs. *Nature*.

Downing, J., Prairie, Y., Cole, J., & Duarte, C. (2006). The Global Abundance and Size Distribution of Lakes, Ponds, and Impoundments. *Limnology and Oceanography*, 2388-2397.

Eilander, D., Boigontier, H., Bouaziz, L., Buitink, J., Couasnon, A., Dalmijn, B., . . . Verseveld, v. W. (2023). HydroMT: Automated and reproducible model building and analysis. *The Journal of Open Source Software*, 1-7.

ESG News Eswatini. (2016, August 15). *Drought-hit Swaziland imposes water cuts*. Retrieved from bizcommunity.com: https://www.bizcommunity.com/Article/203/422/149198.html

EUMeTrain. (2023). *Forecast variable types*. Retrieved from Resources.EUMeTrain: https://resources.eumetrain.org/data/4/451/english/msg/introduction/uos3/uos3_ko1.htm

FAO. (2013). *Drought. Factsheet.* Rome: Food and Agriculture Organization.

FAO. (2022). *Striking before disasters do.* Rome: Food and Agriculture Organization of the United Nations.

Farr, T. G., & Kobrick, M. (2000). Shuttle Radar Topography Mission produces a wealth of data. *Eos Trans. AGU, 81*, 583-583.

Feng, L. C. (2011). MODIS observations of the bottom topography and its inter-annual variability of Poyang Lake. *Remote Sensing of Environment*, 2729-2741.

Gao, H., Birkett, C., & Lettenmaier, D. (2012). Global monitoring of large reservoir storage from satellite remote sensing. *Water Resources Research, 48*(9). doi:10.1029/2012WR012063

Ghasemi, P., Karbasi, M., Nouri, A. T., & Azamathulla, H. (2021). Application of Gaussian process regression to forecast multi-step ahead SPEI drought index. *Alexandria Engineering Journal*, 5375-5392.

Global Forest Watch. (2023, 03 23). *Forest Monitoring Designed for Action*. Retrieved from Global Forest Watch: https://www.globalforestwatch.org/

Greenwood, T. (2018, August 17). *WaterAid: Wet yet thirsty - in these five countries with high rainfall millions lack access to clean water*. Retrieved from Relief Web: https://reliefweb.int/report/world/wateraid-wet-yet-thirsty-these-five-countries-high-rainfall-millions-lack-access-clean

Grill, G., Lehner, B., Thieme, M., Geenen, B., Tickner, D., Antonelli, F., . . . Zarlf, C. (2019). Mapping the world's free-flowing rivers. *Natuer*, 215-221.

Gurrapu, S., Hodder, K., Sauchyn, D., & St. Jacques, J. (2021). Assessment of the ability of the standardized precipitation evapotranspiration index (SPEI) to model historical streamflow in watersheds of Western Canada. *Canadian Water Resources Journal*, 52-72.

Habets, F., Molenat, J., Carluer, N., Douez, O., & Leenhardt, D. (2018). The cumulative impacts of small reservoirs on hydrology: A review. *Science of The Total Environment*, 850-867.

Håkanson, L., & Peters, R. H. (1995). *Predictive Limnology: Methods for Predictive Modelling.* Mitchigan: University of Mitchigan.

Hallema, M. (2022, May 2009). *Meer maatregelen waterschappen tegen droogte*. Retrieved from Nieuwe Oogst: https://www.nieuweoogst.nl/nieuws/2022/05/09/meer-maatregelen-waterschappen-tegen-droogte

Heathcote, A. J., Giorgio, P. d., & Prairie, Y. T. (2015). Predicting bathymetric features of lakes from the topography of their surrounding landscape. *Canadian Journal of Fisheries and Aquatic Sciences*. doi:10.1139/cjfas-2014-0392

Heidke, P. (1926). Berechnung des Erfolges und der Güte der Windstärkevorhersagen im Sturmwarnungsdienst. *Gerog. Ann., 8*(4), 301-349.

Hersbach, H., Bell, B., Berrisford, P., Hirahara, S., Horányi, A., Muñoz-Sabater, J., . . . al, e. (2020). The ERA5 global reanalysis. *Quarterly Journal of the Royal Meteorological Society*, 1999-2049.

Hollister, J. W., Milstead, W. B., & Urrutia, M. A. (2011). Predicting Maximum Lake Depth from Surrounding Topography. *PLoS ONE, 6*(9), e25764. doi:doi.org/10.1371/journal.pone.0025764

Hollister, J., & Milstead, B. (2010). Using GIS to estimate lake volume from limited data. *Lake and Reservoir Management, 26*, 194-199. doi:doi.org/10.1080/07438141.2010.504321

Hrachowitz, M. (2021). *Lecture series of Hydrological Modelling - Lecture 1 - Models in Hydrology.* Delft: Delft University of Technology.

Hrachowitz, M. C. (2017). HESS Opinions: The complementary merits of top-down and bottom-up modelling philosophies in hydrology. *Hydrology and Earth System Sciences Discussions*.

Hutchinson, G. (1957). *A Treatise on Limnology.* New York: John Wiley and Sons.

IBM. (2021, 03 22). *Nonlinear Regression.* Retrieved from IBM: https://www.ibm.com/docs/bg/spss-statistics/25.0.0?topic=regression-nonlinear

Jarvis, A., Reurter, H., Nelson, A., & Guevara, E. (2008). *Hole-Filled SRTM for the Globe Version 4.* Retrieved from http://srtm.csi.cgiar.org

Jenson, S., & Domingue, J. (1988). Extracting Topographic Structure from Digital Elevation Data for Geographic Information System Analysis. *American Society for Photogrammetry and Remote Sensing*, 1593-1600.

Jerlov, N. (1976). *Marine Optics.* Amsterdam: Elsevier Oceanography Series.

Jiao, W., Wang, L., Smith, W., Chang, Q., Wang, H., & D'Odorico, P. (2021). Observed increasing water constraint on vegetation growth over the last three decades. *Nature Communications*, 12.

Khandelwal, A., Karpatne, A., Marlier, M., Kim, J., Lettenmaier, D., & Kumar, V. (2017). An approach for global monitoring of surface water extent variations in reservoirs using MODIS data. *Remote Sensing of Environment, 202*, 113-128. doi:10.1016/j.rse.2017.05.039

Kim, J., Jung, C., Lee, J., & Kim, S. (2018). Development of Naïve-Bayes classification and multiple linear regression model to predict agricultural reservoir storage rate based on weather forecast data. *J. Korea Water Resour. Assoc.*, 839-852.

Knyazev, V. Y., Kossyi, I. A., Malykh, N. I., & Yampolskii, E. S. (2003). Penetration of Microwave Radiation into Water: Effect of Induced Transparency. *Technical Physics, 48*, 1489-1492.

Kozacek, C. (2014, November 4). *Sao Paulo's Water Waiting Game Avoided Rationing But Produced Huge Risk of Severe Shortage*. Retrieved from Circle of Blue: https://www.circleofblue.org/2014/world/sao-paulos-water-waiting-game-avoided-rationing-produced-huge-risk-severe-shortage/

Lehner, B. (2011). High-resolution mapping of world's reservoirs and dams for sustainable river-flow management. *Front. Ecol. Environ.*, 494-502.

Lehner, B., & Döll, P. (2004). Development and validation of a global database of lakes, reservoirs and wetlands. *J. Hydrol.*, 1-22.

Lehner, B., Liermann, C., Revenga, C., Vörösmarty, C., Fekete, B., Crouzet, P., . . . WIsser, D. .. (2011). High-resolution mapping of the world's reservoirs and dams for sustainable river-flow management. *Frontiers in ecology and the environment, 9*(9). doi:10.1890/100125

Li, M., Wang, Q., Bennet, J., & Robertson, D. (2015). *A strategy to overcome adverse effects of autoregressive updating of streamflow forecasts.* EGU.

Li, Y., Gao, H., Jasinski, M., Zhang, S., & Stoll, J. (2019). Deriving High-Resolution Reservoir Bathymetry From ICESat-2 Prototype Photon-Counting Lidar and Landsat Imagery. *Transactions on Geoscience and Remote Sensing, 57*.

Li, Y., Gao, H., Zhao, G., & Tseng, K. (2020). A high-resolution bathymetry dataset for global reservoirs using multi-source satellite imagery and altimetry. *Remote Sensing of Environment*. doi:10.1016/j.rse.2020.111831

Li, Y., Wei, K., Chen, K., He, J., Zhao, Y., Yang, G., . . . Yang, Z. (2023). Forecasting Monthly Water Deficit Based on Multi-Variable Linear Regression and Random Forest Models. *Environmental and Human Impacts on Hydrological Drought*, 1057.

Magagula, L. (2016). *Hawane DAM.* Mbabane: Eswatini TV.

Magruder, L., Neuenschwander, A., & Klotz, B. (2021). Digital terrain model elevation corrections using space-based imagery and ICESat-2 laser altimetry. *Remote Sensing of Environment.* doi:10.1016/j.rse.2021.112621

Mahr, K. (2018, May 4). *How Cape Town was saved from running out of water.* Retrieved from The Guardian: https://www.theguardian.com/world/2018/may/04/back-from-the-brink-how-cape-town-cracked-its-water-crisis

Markus, T., Neumann, T., Martino, A., Abdalati, W., Brunt, K., Csatho, B., . . . Popescu, S. (2017). The Ice, Cloud, and land Elevation Satellite-2 (ICESat-2): Science requirements, concept, and implementation. *Remote Sensing of Environment, 190*, 260-273.

Massonnet, D., & Feigl, K. (1998). Radar interferometry and its application to changes in the Earth's surface. *Review of Geophysics*, 441-689.

McGuire, M., Wood, A., Hamlet, A., & Lettenmaier, D. (2006). Use of satellite data for streamflow and reservoir storage forecasts in the Snake River Basin. *ASCE.*

Messager, M. L., Lehner, B. L., Grill, G., Nedeva, I., & Schmitt, O. (2016). Estimating the volume and age of water stored in global lakes using a geo-statistical approach. *Nature Communications.* doi:10.1038/ncomms13603

Messager, M., Lehner, B., Grill, G., Nedeva, I., & Schmitt, O. (2016). Estimating the volume and age of water stored in global lakes using a geo-statistical approach. *Nat. Commun.*, 1-11.

Minderhoud, P., Coumou, L., Erkens, G., Middelkoop, H., & Stouthamer, E. (2019). Mekong delta much lower than previously assumed in sea-level rise impact assessments. *Nature Communications*, Online. doi:10.1038/s41467-019-11602-1

Morris, G., & Fan, J. (1998). *Reservoir Sedimentation Handbook.* New York: McGraw-Hill Book Co.

Mulligan, M., Van Soesbergen, A., & Sáenz, L. (2020). GOODD, a global dataset of more than 38,000 georeferenced dams. *Scientific Data, 7*.

Murray-Darling Basin Authority. (2022, 09 02). *The Basin Plan*. Retrieved from mdba.gov.au: https://www.mdba.gov.au/basin-plan/sustainable-diversion-limits/sustainable-diversion-limit-accounting-reporting-framework

Muwowo, C. (2012, October 12). *e-Mita Sunset*. Retrieved from masukuonmymind.com: https://masukuonmymind.com/2012/10/12/beautiful-zambia/e-mita-sunset/

NASA. (2019, 02 08). *The SAR Handbook.* Huntsville: NASA. doi:10.25966/nr2c-s697

NASA. (2023, 02 24). *Counting on NASA's ICESAT-2.* Retrieved from ICESAT-2: https://icesat-2.gsfc.nasa.gov/articles/counting-nasas-icesat-2#:~:text=While%20the%20first%20ICESat%20satellite,the%20surface%20they%27re%20measuring.

Neumann, T., Martino, A., Markus, T., Bae, S., Bock, M., Brenner, A., . . . Ramos-Izquierdo, L. (2019). The Ice, Cloud, and Land Elevation Satellite – 2 mission: A global geolocated photon product derived from the Advanced Topographic Laser Altimeter System. *Remote Sensing of Environment, 233*. doi:10.1016/j.rse.2019.111325

O'Callighan, J., & Mark, D. (1984). The extraction of drainage networks from digital elevation data. *Computer Vision, Graphics and Image Processing, 28*(3), 323-344.

Parrish, C., Magruder, L., Neuenschwander, A., Forfinski-Sarkozi, N., Alonzo, M., & Jansinski, M. (2019). Validation of ICESat-2 ATLAS Bathymetry and Analysis of ATLAS's Bathymetric Mapping Performance. *Remote Sensing, 11*(14). doi:10.3390/rs11141634

Pistocchi, A., & Pennington, D. (2006). European hydraulic geometries for continental SCALE environmental modelling. *Journal of Hydrology, 329*, 553-567. Retrieved 01 05, 2023

Qin, C., Zhu, A.-X. P., Li, B., Zhou, C., & Yang, L. (2007). An adaptive approach to selecting a flow-partition exponent for a multiple-flow direction algorithm. *International Journal of Geopgraphical Information Science, 21*(4), 443-458.

Ramsar Sites Information Service. (2016, 09 26). *Hawane Dam and Nature Reserve*. Retrieved from rsis.ramsar.org: https://rsis.ramsar.org/ris/2121

Red Cross 510. (2023). *Human Centred Design Interviews in Lesotho.* The Hague: Red Cross.

Savenije, H., & Hrachowitz, M. (2017). HESS Opinions "Catchments as meta-organisms - a new blueprint for hydrological modelling". *Hydrology and Earth System Sciences*, 1107-1116.

Schellekens, J. (. (2019). *wflow*. Retrieved from wflow.readthedocs.io: https://wflow.readthedocs.io/

Sene, K. (2010). Hydrological Forecasting. *Hydrometeorology*, 101-140.

Shen, Y., Liu, D., Jiang, L., Nielsen, K., Yin, J., Liu, J., & Bauer-Gottwein, P. (2022). High-resolution water level and storage variation datasets for 338 reservoirs in China during 2010-2021. *Earth Syst. Sci. Data, 14*, 5671-5694. doi:10.5194/essd-14-5671-2022

SMHI. (2006). *The HBV Model*. Retrieved from http://www.smhi.se/forskning/forskningsomraden/hydrologi/hbv-1.1566: https://www.scirp.org/(S(czeh2tfqyw2orz553k1w0r45))/reference/ReferencesPapers.aspx?ReferenceID=1702441

Sobek, S., Nisell, J., & Fölster, J. (2011). Predicting the depth and volume of lakes from map-derived parameters. *Inland Waters, 1*(3), 177-134. doi:10.5268/IV-1.3426

Studio Pietrangeli. (2012a). *Bathymetrical Report.* Mulungushi: Lunsemfwa Hydro Power Company.

Studio Pietrangeli. (2012b). *Mita Hills, Bathymetrical Report.* Studio Pietrangeli: Lunsemfwa Hydro Power Company.

Stysley, P., Coyle, D., Clarke, G., Frese, E., Blalock, G., Morey, P., . . . Hersh, M. (2015). Laser Production for NASA's Global Ecosystem Dynamics Investigation (GEDI) Lidar. *International Society for Optics and Photonics*. doi:10.1117/12.2191569

Tarboton, D. G. (1997). A New Method for the Determination of Flow Directions and Contributing Areas in Grid Digital Elevation Models. *Water Resoures Research, 33*(2), 309-319.

Tracks4Africa. (2013, January). *Hawane Nature Reserve*. Retrieved from tracks4africa.co.za: https://tracks4africa.co.za/listings/item/w180397/hawane-nature-reserve/

Trimble, S. W. (2012). Reservoir and Lake Trap Efficiency. In R. H. L. Bengtsson, *Encyclopedia of Lakes and Reservoirs* (p. 619). 226: Springer Science+Business Media. doi:10.1007/978-1-4020-4410-6

Tseng, K., Shum, C., Kim, J., Wang, X., Zhu, K., & Cheng, X. (2016). Integrating Landsat Imageries and Digital Elevation Models to Infer Water Level Change in Hoover Dam. *Journal of selected topics in applied earth observations and remote sensing, 9*(4), 1696-1709.

UNDRR. (2015). *Sendai Framework for Disaster Risk Reduction 2015-2030.* Geneva: United Nations.

UNESCO. (2005). Data-Based Models. In UNESCO, *Water Resources Systems Planning and Management* (p. 147). UNESCO.

UNESCO. (2019). *The UN World Water Development Report: Leaving no one behind.* Geneva: UNESCO.

UNICEF. (2023, 01 02). *Water Scarcity*. Retrieved from UNICEF.ORG: https://www.unicef.org/wash/water-scarcity#:~:text=Water%20scarcity%20limits%20access%20to,water%20also%20becomes%20more%20expensive.

Van Loon, A., & Van Lanen, H. (2013). Making the distinction between water scarcity and drought using an observation-modelling framework. *Water Resources Research, 49*, 1483-1502. doi:10.1002/wrcr.20147

Vernimmen, R., Hooijer, A., & Pronk, M. (2020). New ICESat-2 satellite LiDAR data allow first global lowland DTM suitable for accurate coastal flood risk assessment. *Remote Sensing, 12*(2827).

Wheatcroft, E. (2019). Interpreting the skill score form of forecast performance metrics. *International Journal of Forecasting*, 573-579.

White, W. (2000). Contributing paper flushing of sediments from reservoirs. Prepared or thematic review IV.5: operation, monitoring and decommisioning of dams. *World Commission on Dams.* Cape Town.

World Bank Group. (2021, March 04). *Climate Change Knowledge Portal - Eswatini.* Retrieved from climatechangeknowledgeportal.worldbank.org: https://climateknowledgeportal.worldbank.org/country/eswatini/climate-data-historical

Xiao, X., White, E., Hooten, M., & Durham, S. (2011). On the use of log-transformation vs. nonlinear regression for analyzing biological power laws. *Ecology*, 1887-1894.

Yamaguchi, Y., Kahle, A., Tsu, H., Kawakami, T., & Pniel, M. (1998). verview of Advanced Spaceborne Thermal Emission and Reflection Radiometer (ASTER). *EEE Trans. Geosci. Remote Sens.Remote Sensing, 36*, 1062-1071.

Yamazaki, D., Ikeshima, D., Sosa, J., Bates, P., Allen, G., & Pavelsky, T. (2019). MERIT Hydro: A High-Resolution Global Hydrography Map Based on Latest Topography Dataset. *Water Resources Research*, 5053-5073. doi:10.1029/2019WR024873

Appendix A: Global Water Watch

Figure A: Screenshot of the Global Water Watch website, showing step by step how the reservoir surface area for, in this case, the Mita Hills reservoir in Zambia is obtained. Retrieved from globalwaterwatch.org (2023).
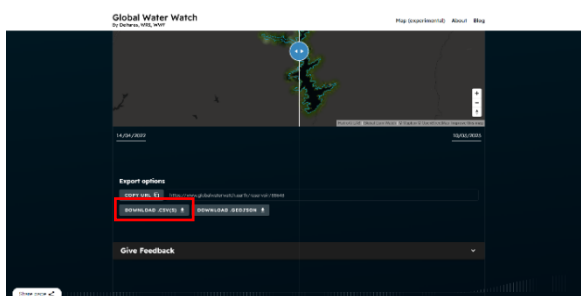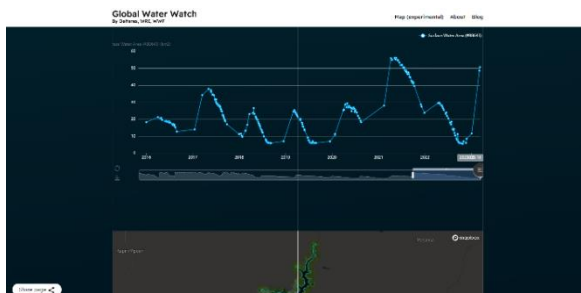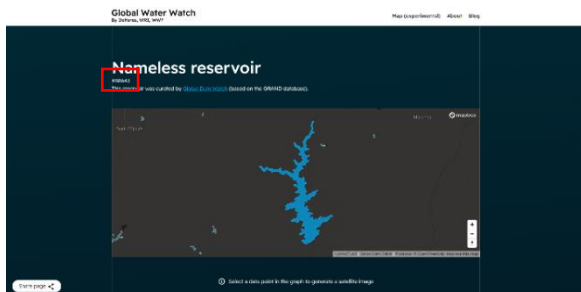
Appendix B: Hypsometric Curves

Figure B: The hypsometric relations established with the novel method for the Mita Hills reservoir (top) and the Mulungushi reservoir (bottom) in Zambia. The figures on the left provide the relation between area and water level height, the middle figures provide the relation between volume and water level height, the right figures provide the relation between volume and area.
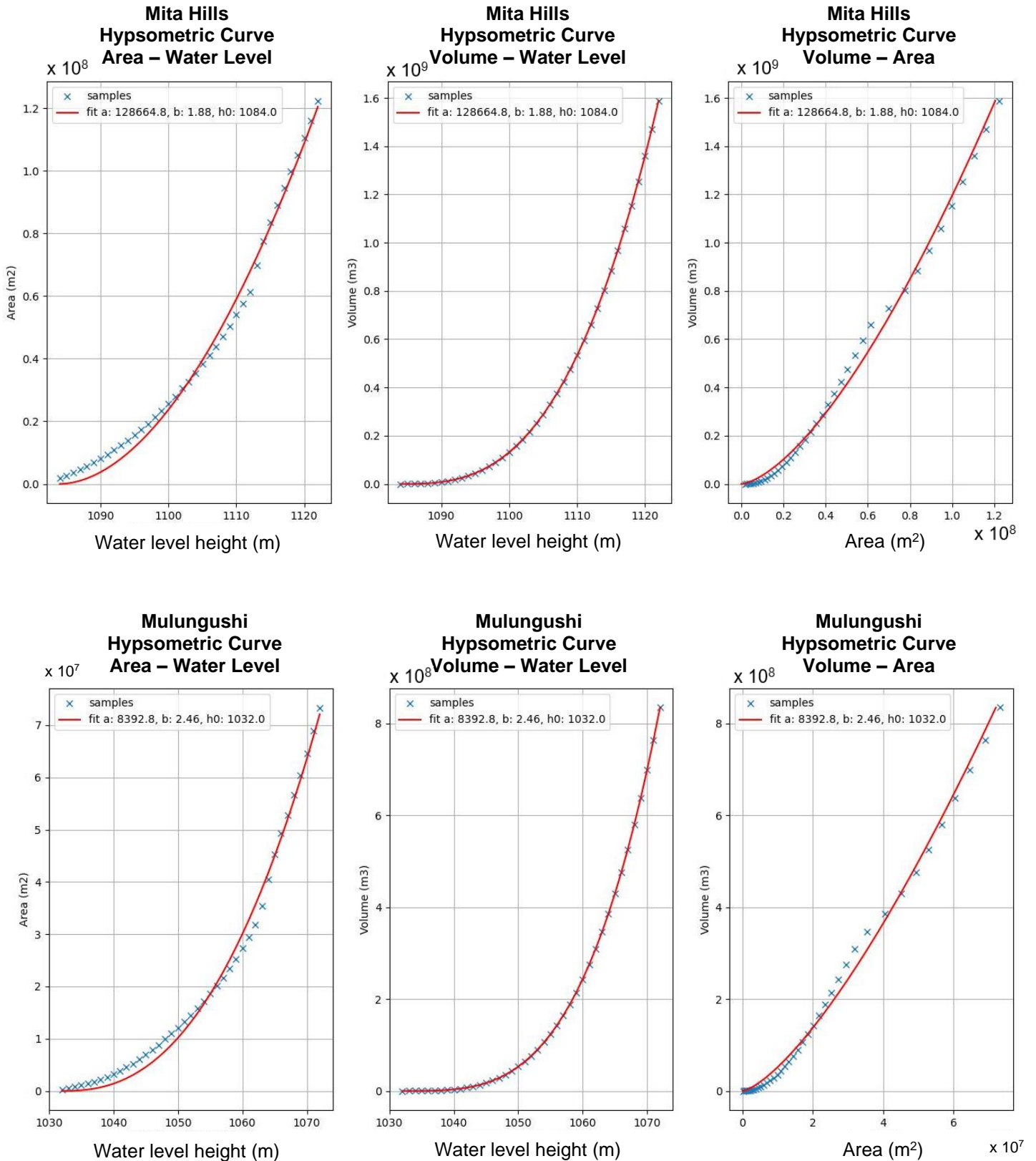
Appendix C: Performance Indian Reservoirs

The Map of India incl. 46 Bad Performing Reservoirs

Figure C1: The map of India including the bad reservoir locations. The bad performing reservoirs are presented in pink, the really bad performing reservoirs are presented in red.

The Map of India incl. 48 Good Performing Reservoirs

Figure C2: The map of India including the good performing reservoir locations. The neutral performing reservoirs are presented in orange, the good performing reservoirs are presented in green.

Appendix D: Bathymetry Hawane Reservoir

Hawane Reservoir DEM
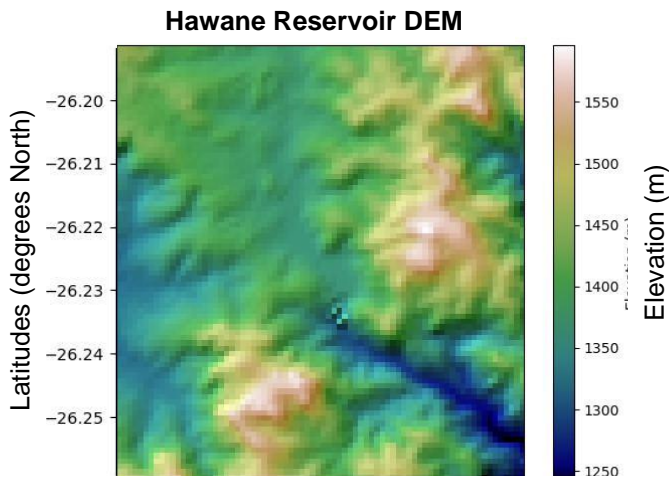
Figure D1: The MERIT-Hydro DEM presenting the Hawane region. The axis provides the longitudes (°) and latitudes (°). The elevation is provided in the z-direction indicated by the colors on the color bar.
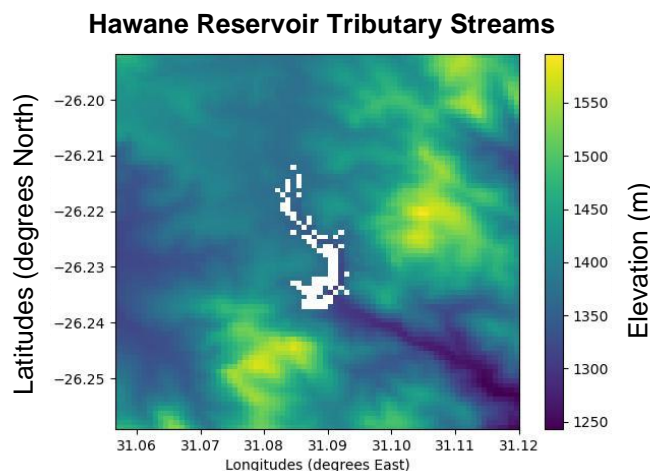

Hawane Reservoir Filtered
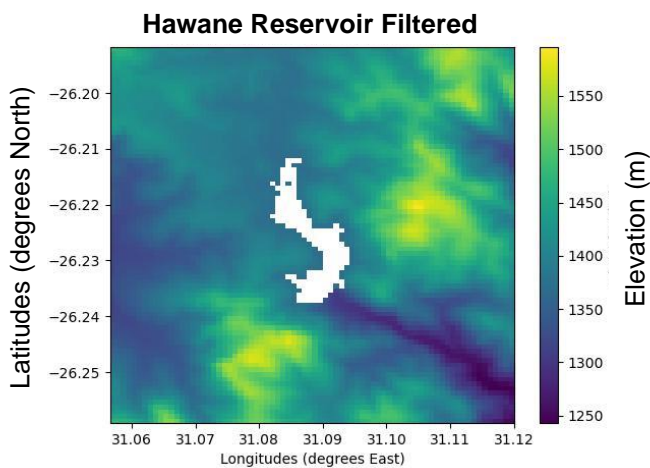
Figure D2: Cells representing the water surface are filtered from the MERIT-Hydro DEM presenting the Hawane region. The axis provides the longitudes (°) and latitudes (°). The elevation is provided in the z-direction indicated by the colors on the color bar.

Hawane Reservoir Tributary Streams

Figure D3: Tributary streams with new elevations plotted in the Hawane reservoir. The axis provides the longitudes (°) and latitudes (°). The elevation is provided in the z-direction indicated by the colors on the color bar.

Hawane Reservoir Bathymetry
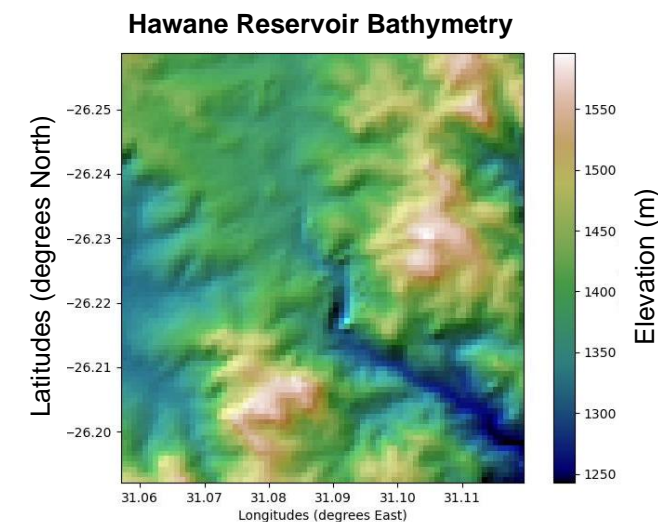
Figure D4: Cubic interpolation to obtain bathymetry in Hawane Dam. The axis provides the longitudes (°) and latitudes (°). The elevation is provided in the z-direction indicated by the colors on the color bar.
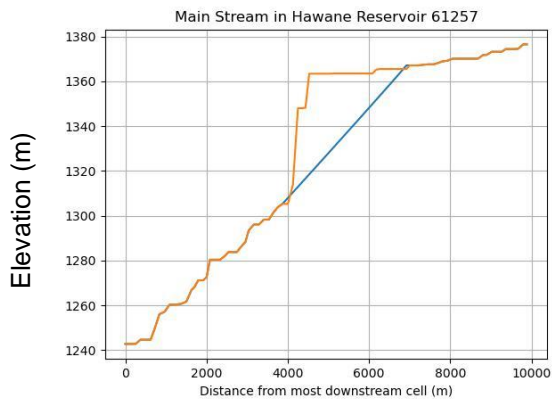
Figure D5: Bathymetry (blue) on main stream in the Hawane Dam. On the x-axis the distance from the most downstream cell is plotted (m), and the elevation is plotted on the y-axis.
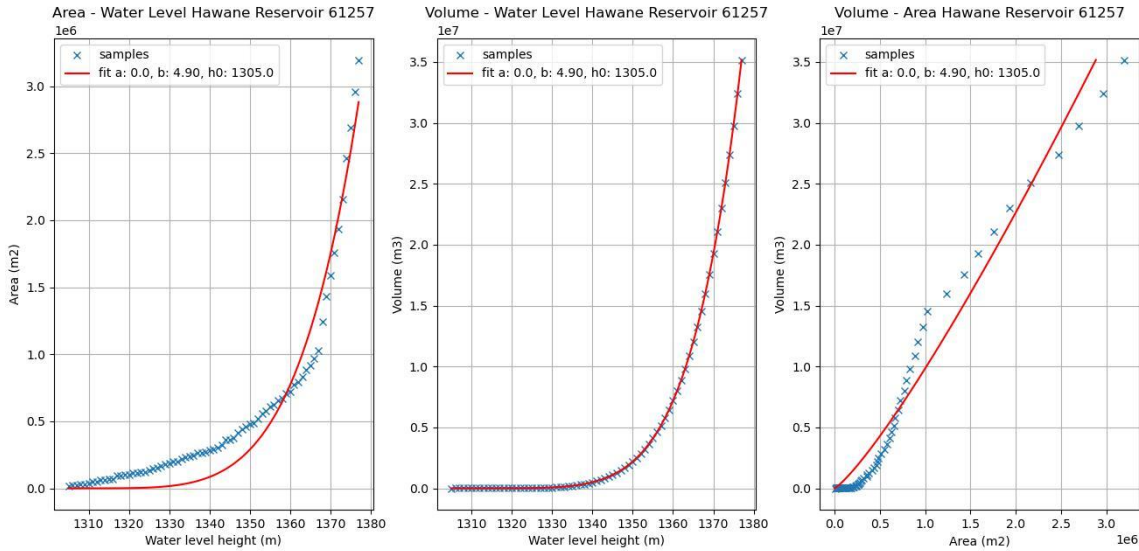

Figure D6: The hypsometric curves provided for Area-Water Level (left), Volume Water-Level (middle) and Volume-Area (right) in the Hawane Dam.
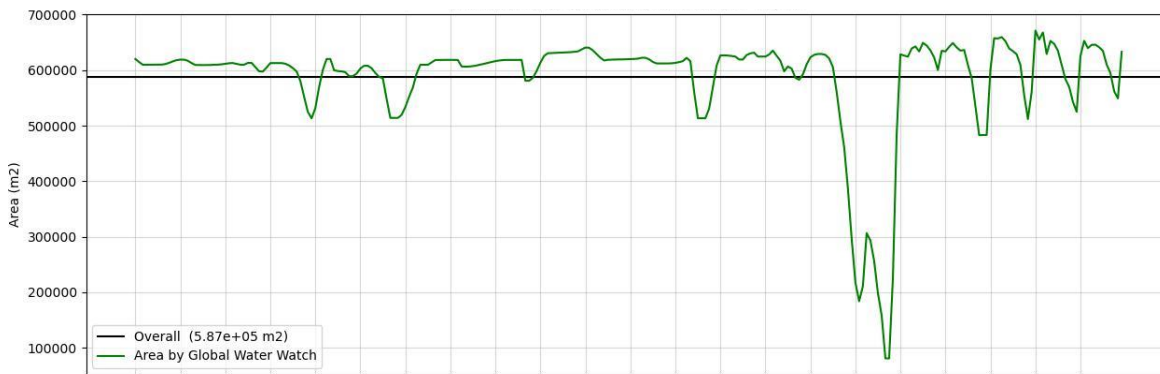

Figure D7: Area time series of Hawane reservoir obtained with Global Water Watch by Donchyts et al. (2016).
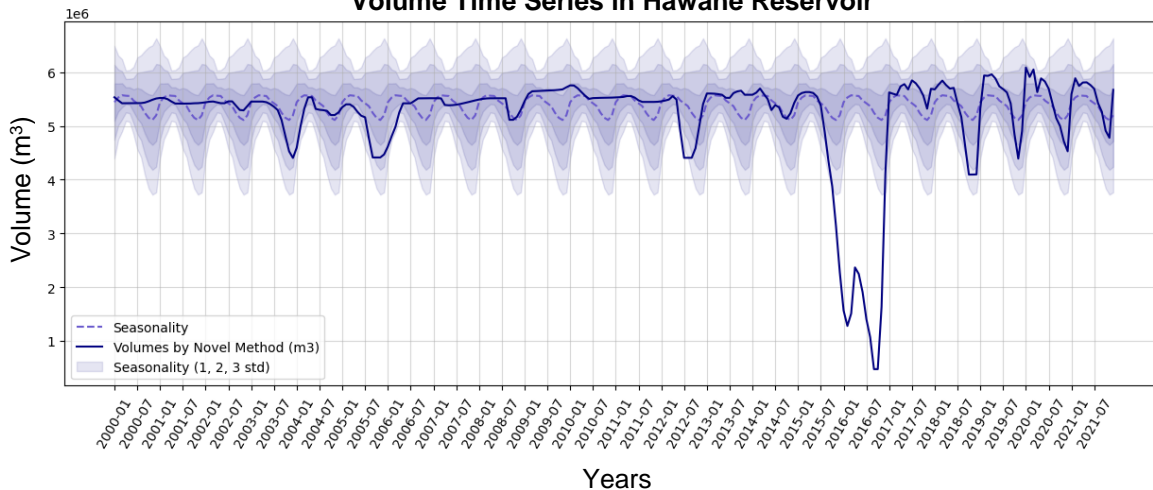

Figure D9: Volume time series of the Hawane reservoir in Eswatini, showing the seasonal mean (dotted line) and seasonality computed over regular years (2000-2014 & 2017-2021) presented in blue shades, with 1, 2, and 3 standard deviations from the mean. The severe drought event that occurred in 2015-2016 resulted in a significant drop of over 3 standard deviations in reservoir volume.
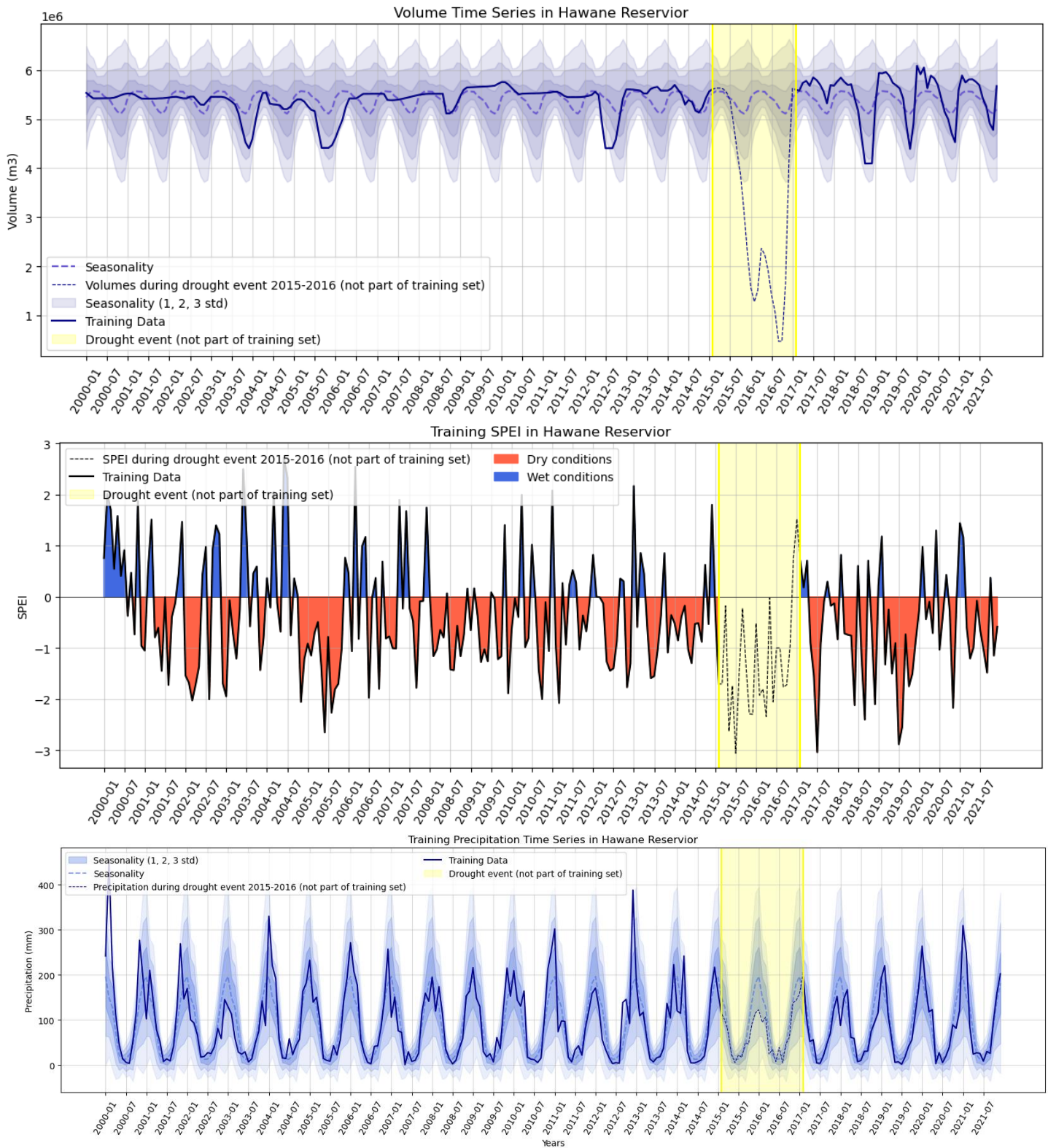
Figure E1: The training data used for the regression models for volume (top), SPEI (middle) and precipitation (bottom), which are the remaining values of the precipitation time series of the catchment upstream of the Hawane reservoir after filtering out the drought period (highlighted in yellow). The figure also displays the seasonal mean (dotted line) and seasonality computed over regular years (2000-2014 & 2017-2021) in blue shades, with 1, 2, and 3 standard deviations from the mean.
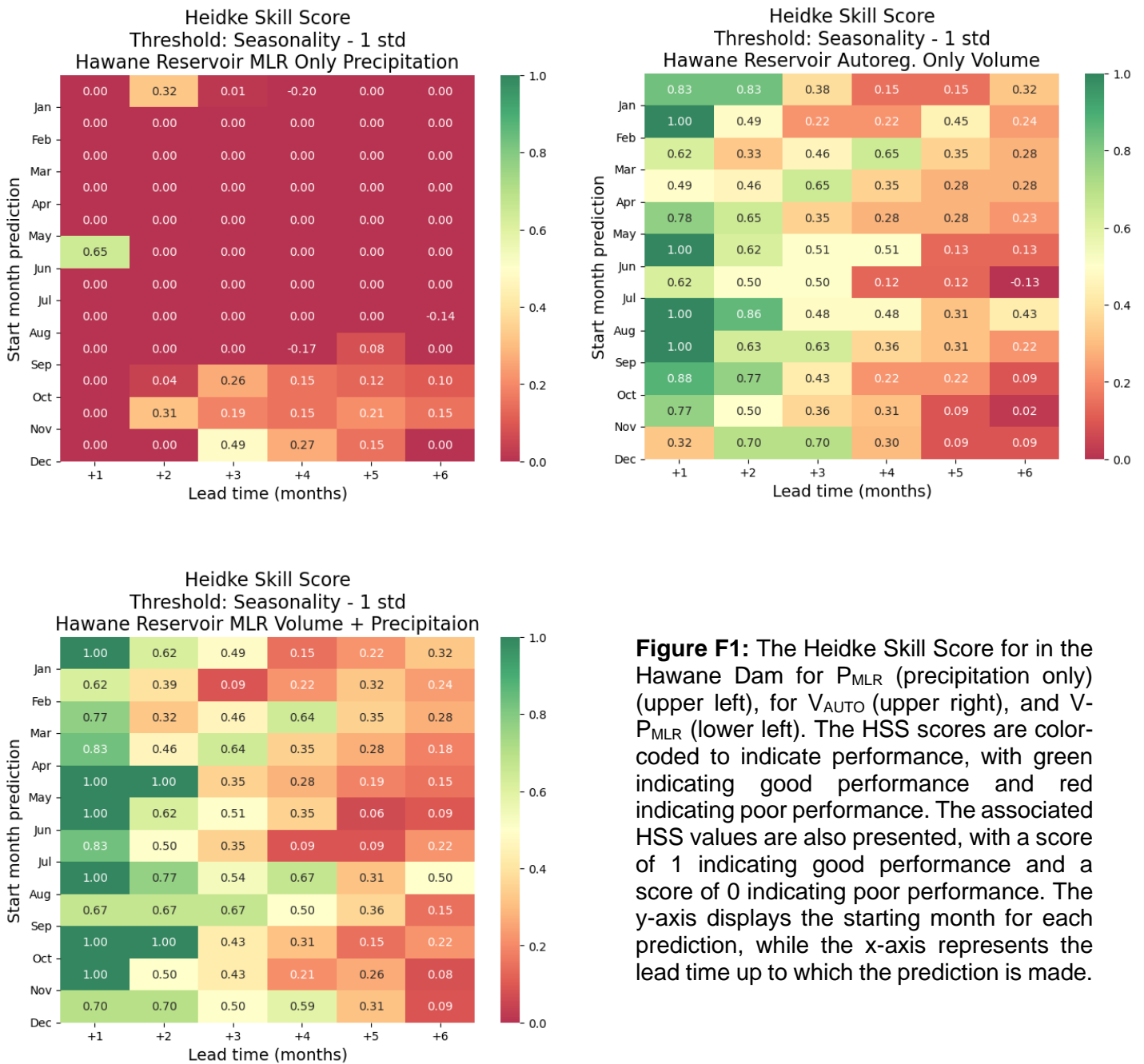
Appendix F Heidke Skill Scores

Heidke Skill Score
Threshold: Seasonality - 1 std
Hawane Reservoir MLR Only Precipitation

Heidke Skill Score
Threshold: Seasonality - 1 std
Hawane Reservoir Autoreg. Only Volume

Heidke Skill Score
Threshold: Seasonality - 1 std
Hawane Reservoir MLR Volume + Precipitaion

Figure F1: The Heidke Skill Score for in the Hawane Dam for P_{MLR} (precipitation only) (upper left), for V_{AUTO} (upper right), and V-P_{MLR} (lower left). The HSS scores are color-coded to indicate performance, with green indicating good performance and red indicating poor performance. The associated HSS values are also presented, with a score of 1 indicating good performance and a score of 0 indicating poor performance. The y-axis displays the starting month for each prediction, while the x-axis represents the lead time up to which the prediction is made.
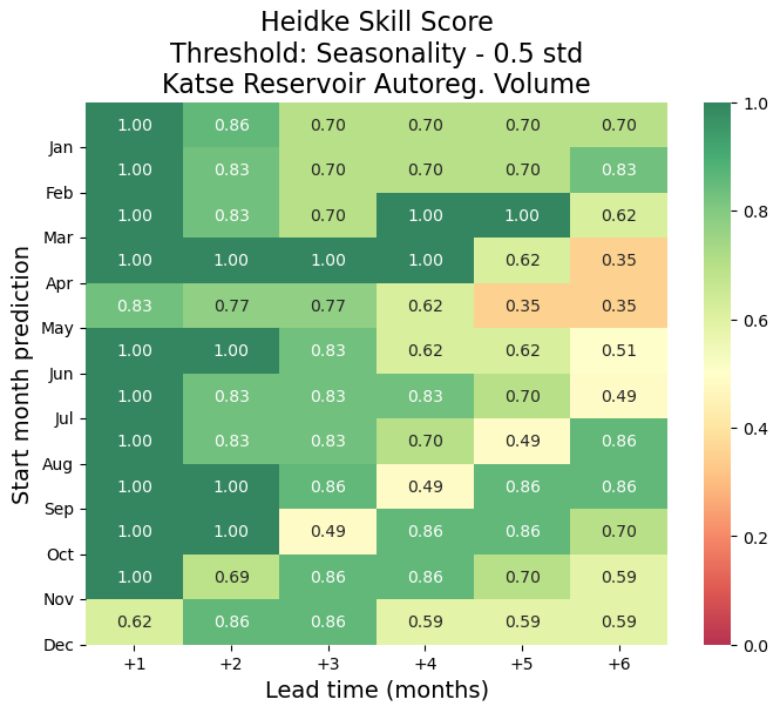
Heidke Skill Score
Threshold: Seasonality - 0.5 std
Katse Reservoir Autoreg. Volume

Figure F2: The Heidke Skill Score for in the Katse Dam for V_{AUTO} (upper), and V-SPEI$_{MLR}$ (lower). The HSS scores are color-coded to indicate performance, with green indicating good performance and red indicating poor performance. The associated HSS values are also presented, with a score of 1 indicating good performance and a score of 0 indicating poor performance. The y-axis displays the starting month for each prediction, while the x-axis represents the lead time up to which the prediction is made.

Heidke Skill Score
Threshold: Seasonality - 0.5 std
Katse Reservoir MLR Volume + SPEI3